BRUNEL UNIVERSITY

LEWIS KIELY

MODELLING OF SHOCK WAVES IN FCC AND BCC METALS USING A DISLOCATION BASED CONTINUUM APPROACH

Mechanical and Aerospace Engineering

PhD
Academic Years: 2016 - 2019

Supervisor: Prof Rade Vignjevic
Dr Nenad Djordjevic

August 2019

BRUNEL UNIVERSITY

Mechanical and Aerospace Engineering

PhD

Academic Years 2016 - 2019

LEWIS KIELY

MODELLING OF SHOCK WAVES IN FCC AND BCC METALS USING A DISLOCATION BASED CONTINUUM APPROACH

Supervisor: Prof Rade Vignjevic
Dr Nenad Djordjevic
August 2019

ABSTRACT

Recent experimental data has revealed that, over short time scales (on the nanosecond time scale), during formation of a shock in metals the amplitude of the ‘elastic’ precursor greatly exceed the Hugoniot elastic limit (HEL), before decaying to the level of the HEL. Existing continuum scale material models are unable to reproduce this behaviour. To capture this aspect of material behaviour physical effects related to high rate dislocation mechanics have to be taken into consideration and included into the continuum scale material model.

This is achieved with the use of a dislocation dynamics based model, where the state variable are calculated on the microscale, before being fed up to the continuum scale by use of the Orowan equation. Three state variable are used for the evolution of plasticity on the microscale; the density of mobile dislocation, the density of immobile dislocations and the velocity of dislocations. The model used in this work was previously available in literature in a 1D form only. Full 3D implementation of the model is made in a finite element hydrocode, including coupling with an appropriate equation of state

Model validation was done by comparison of numerical results with experimental data for plate impact tests (1D strain state) for aluminium and copper, both fcc structured metals. The difference between the experimental and numerical values of the compared parameters (longitudinal stress, pulse length, elastic precursor relaxation time) was within 10%. Notably the plate impact tests show that over the first 50ns after impact the pre-cursor wave has an amplitude similar to the stress levels behind the shock wave, relaxing to HEL with time (wave propagation).

Further developments are made to the model to allow for simulation of the more complexly yielding bcc single crystals, with a focus on the simulation of single crystal tantalum plate impact tests. It is observed that the model accurately predicts the shape of the rear surface velocity obtained experimentally for single crystal tantalum, with analysis of the generate simulation data allowing for explanation of the features observed.

Further to the use of the model for simulations, method have been developed to allow for the determination of material parameter using the fitting of data.

Keywords:

Single crystals, precursor decay, tantalum, plasticity

ACKNOWLEDGEMENTS

I would like to thank my supervisors, Prof Rade Vignjevic and Dr Nenad Djordjevic for their support and guidance throughout this work. Their invaluable input has enabled the successful completion of this work. Additionally, their guidance and critiques have enabled me to develop personally, which will stay with me for life.

Secondly, I am extremely grateful to the sponsors of this work, AWE for their financial support, and to Dr Simon Case and Dr James Turner for valuable input into the technical side of this work.

Additional thanks goes to Dr James Campbell, Dr Tom DeVuyst and Dr Kevin Hughes for providing additional support and motivation when required.

Finally, I am would like to thank my family, my mother, father, brother and gran for always believing in me and supporting me throughout this work, particularly at the more challenging times. Without this support completion of this work would not have been possible.

TABLE OF CONTENTS

LIST OF FIGURES

LIST OF TABLES

Nomenclature

English alphabet

A - cross sectional area

a_0 - lattice constant

B - coefficient of dynamic drag

$\mathbf{b}$ - Burgers vector

b - Magnitude of Burgers vector

b_s, b_e - screw and edge components of Burgers vector

$\mathbf{C}$ - right Cauchy Green tensor

c - wave speed

c_b - bulk speed of sound

c_t - transverse speed of sound

E - specific internal energy

$\mathbf{F}$ - deformation gradient

$\mathbf{F}_e, \mathbf{F}_p$ - elastic and plastic parts of the deformation gradient

F - force

F_{cl} - climb component of force

F_{gl} - glide component of force

G - shear modulus

H - Hugoniot function

h - Planck's constant

J - volume ratio

k_a - coefficient of annihilation of dislocations

k_g - coefficient of generation of dislocations

L - length

$\mathbf{l}$ - spatial velocity gradient

m - mass

m_0 - rest mass of dislocations

$\mathbf{n}$ - unit vector normal to slip plane

$\mathbf{P}$ - first Piola-Kirchhoff stress tensor

P - pressure

P_1, P_0 - pressure ahead of and behind shock front

$\mathbf{p}$ - momentum

Q_D^β - rate of generation of dislocations

Q_I^β - rate of immobilisation of dislocations

$\mathbf{R}$ - rotation tensor

$\mathbf{R}_p$ - plastically induced rotation tensor

$\mathbf{S}$ - second Piola-Kirchhoff stress tensor

$\mathbf{s}$ - direction of slip

S_{ik} - stress deviators

T - temperature

U_{ik} - total deformation

$\mathbf{u}^{pl}$ - plastic deformation

$\mathbf{u}$ - displacement

$\mathbf{U}$ - stretch tensor

U_P - particle velocity

U_s - shock velocity

$\mathbf{v}$ - velocity

V - volume

V_D^{β} - velocity of mobile dislocations

V_I - characteristic velocity of dislocations during immobilisation processes

$\mathbf{w}$ - rate of rotation tensor

W - energy

W_e - elastic energy

W_p - potential energy

W_t - total energy

Y - yield strength

Y_0 - resistance due to Peierls barrier

Greek alphabet

γ - shear strain

$\dot{\gamma}$ - rate of shear strain

δ_{ik} - Kronecker delta

$\mathbf{E}$ - Green Lagrange strain

$\boldsymbol{\varepsilon}$ - Euler Almansi strain

$\dot{\boldsymbol{\varepsilon}}_{pl}$ - rate of plastic strain

$\boldsymbol{\varepsilon}_{pl}$ - plastic strain

θ - Debye temperature

ν - Poissons ratio

ρ - mass density

ρ_0 - minimum density of dislocations required for immobilisation processes

ρ_D^β - density of mobile dislocations

ρ_I^β - density of immobile dislocations

ρ_I - total density of immobile dislocations

$\tilde{\Sigma}, \overline{\Sigma}$ - Mandel stress in the intermediate and isoclinic configuration

$\boldsymbol{\sigma}$ - Cauchy stress

σ_d - dislocation self stress

$\boldsymbol{\tau}$ - Kirchhoff stress

χ - motion

ψ_e - stress function

1 Introduction

Computation modelling of material deformation has many benefits to a wide range of industries. Accurate and reliable simulations can significantly reduce costs and the need for destructive testing during the design stages of many products including aircraft, spacecraft, satellites, automobiles and weapons. This work focuses on the modelling of deformation of metals.

It is well established that the deformation of metals can be characterised into three main categories: elastic, plastic and damage, where elastic deformation is reversible upon unloading, plastic deformation is permanent but does not affect the elastic stiffness of the metal, and damage is associated with the formation of microcracks and microvoids, and is therefore permanent upon unloading and affects the elastic properties of the metal.

The main focus of this work is the modelling of plastic deformation of metals. Plasticity is an important phenomena in metals, as, depending on the application, it could be a desirable effect or could be catastrophic. In manufacturing processes, the forming of sheet metals require plastic deformation to occur in order to create the desired shaping of the product, whereas in the design of a submarine hull it is essential to avoid plastic flow under loading as this could lead to catastrophic underwater results.

The specific metals of interest in this work are single crystal metals, with either a face centred cubic structure, or a body centred cubic structure.

The dynamic strength of metals; the stress required for plastic flow to occur, is observed to have a non-linear dependence on the strain rate. The typical relationship between the dynamic strength of a metal and the strain rate is shown in Figure 1-1.

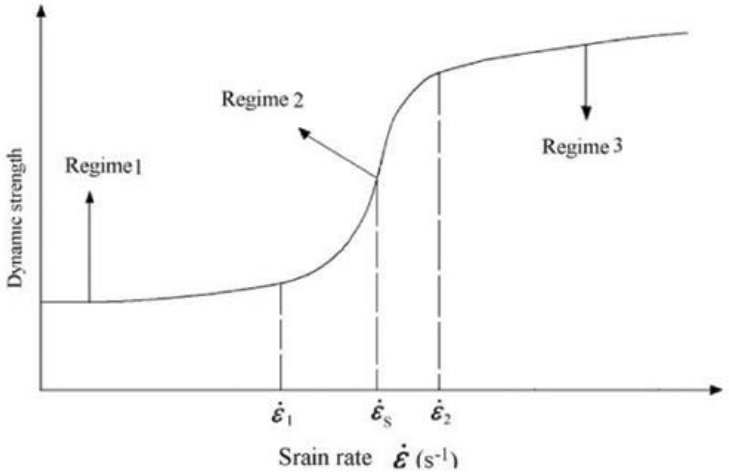

Figure 1-1: Graph showing the three regimes of strain rate dependence on the dynamic strength of materials. (Qi, et al., 2009)

It is seen in Figure 1-1 that there are three regime of strain rate dependence on the dynamic strength of materials. Firstly, in regime 1, it is seen that increasing strain rate produces very little increase in dynamic strength. However in regime 2, a strong dependence of the strain rate is observed on the dynamic strength. Finally, when the strain rate is sufficiently high, the dependence of the strain rate on the dynamic strength decreases significantly.

From Figure 1-1 it is apparent that, when developing a model, the strain rate dependence must be taken into account depending on the intended applications of the model. It is also observed that the strain rate dependence is likely to be a limiting factor with regards to the range of applicability of a model. The focus of this work is on modelling at high strain rates, such as those observed during high velocity impacts or explosive loading.

It has been shown in recent ultrashort laser pulse experiments that the amplitude of ‘elastic’ precursor wave behave differently to that observed using traditional approaches. This can be seen in Figure 1-2. Figure 1-2 shows the results of a plate impact test, where the amplitude of the stress is plotted vs the distance the wave has propagated into the plate a different instances in time. The time scales used are over the nanosecond range. The plot on the right hand side of Figure 1-2 shows the results obtained using an existing continuum mechanics model,

with plasticity driven via an MTS approach. It is seen that a small precursor wave of a fixed amplitude precedes the main plastic shock front. The left had side plot shows the results obtained using a multiscale approach (Mayer, et al., 2013), with the behaviour of the precursor wave significantly different. It is observed that the amplitude of this wave initially exceeds the amplitude of the trailing plastic shock front, before decaying over a short time scale to the traditional elastic limit. A primary objective of this work is to capture the precursor decay in the framework of the traditional continuum mechanics model.

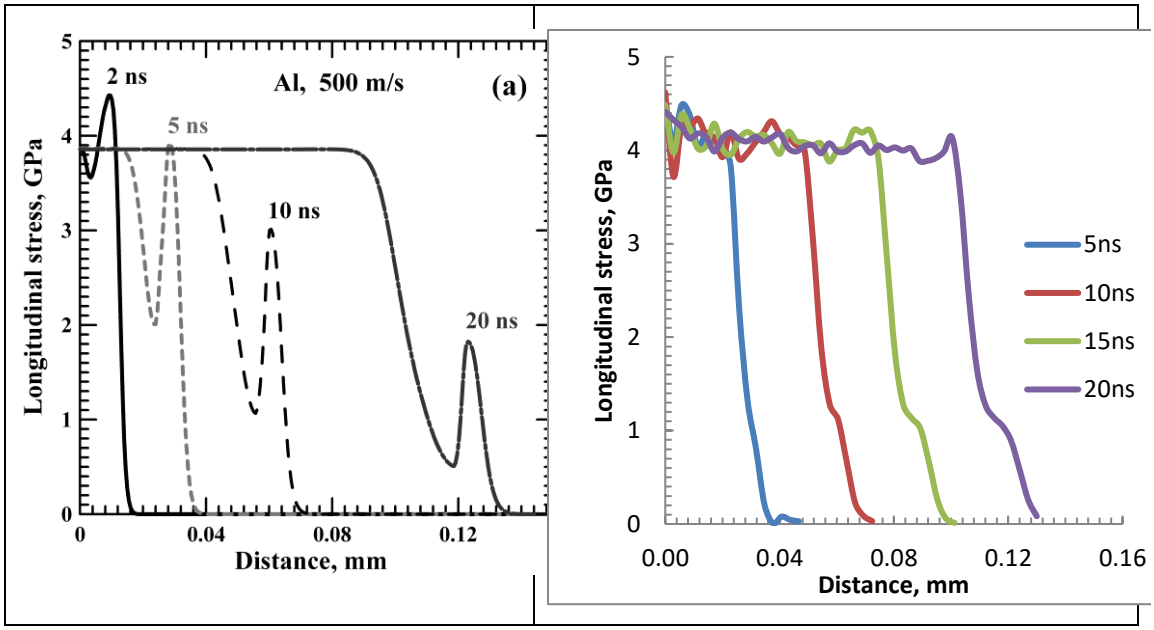

Figure 1-2: Plots showing the longitudinal stress plotted against distance into the target plate at instances of 2, 5, 10 and 20 nanoseconds after impact of two symmetrical aluminium plates at a relative impact velocity of 500 m/s obtained using two different models.

1.1 Aim and Objectives

The overall aim of this piece of work is summarised into the following aim:

“To develop a constitutive model capable of (accurately) predicting high strain rate deformation processes of metals at the continuum level, incorporating physics from sub-continuum scales”

In order to achieve this aim, the following objectives have been identified, which can be used to ensure specific targets are achieved in the duration of the work, and also be used to measure progress towards completion.

- Development and implementation of a dislocation based continuum model for plasticity in finite element hydrocode available at Brunel University for modelling fcc metals.
- Extension of model to incorporate the deformation of bcc metals
- Validation of both fcc and bcc models for single crystal examples, including comparison against experimental data.
- Identify and develop method of determining material model parameters.

1.2 Methodology

To achieve the aim and objectives outlined above, the following methodology was followed.

Firstly, a model was identified in literature which shown potential capable of reproducing precursor decay behaviour during shock formation. The model identified in literature is a 1D model with published results showing capture of precursor decay behaviour. However, some limitations of the model are identified:

- 1D
- Only tested for single crystal fcc metals

The formulation of the model is analysed and implementation in a full 3D form is made in finite element hydrocode, including coupling with an equation of state:

- Incorporation of full stress tensor
- Inclusion of all material slip systems
- Couple with appropriate equation of state

Next, validation is the performed for FCC single crystal metals:

- Repeat validation available in literature, including comparison of plate impact tests against experimental data
- Confirm precursor decay behaviour is successfully captured in 3D implementation

Finally the applicability of the model is extended to allow for simulation of BCC single crystals. This stage required several aspects of work to be completed:

- Inclusion of complex slip systems, up to 48
- Determination of material parameters for single crystal Tantalum

- Simulation of single crystal plate impact tests
- Full analysis of simulated data to explain features observed in both experimental and simulated plots

1.3 Structure of report

The structure of this thesis is as follows: chapter two focusses on the motivation and need for this work as has been determined by surveying current literature. Following this chapter 3 outlines the continuum mechanical foundations of modelling at the continuum scale. This is followed by a discussion of the physical concepts of shock waves, including the continuum mechanical considerations required for modelling shocks. Chapter 5 outlines the microscale physics, in the form of dislocation dynamics, which is used as the underlying principles for the development of plasticity in the new material model, which is described in chapter 6. The implementation of the new material model in the hydrocode available is described in chapter 7, which is followed by the validation process for fcc metals presented in chapter 8. Chapter 9 outlines the new application of the model to modelling bcc single crystal tantalum. The report is concluded with the conclusions and proposed future work in chapter 10.

2 Survey of relevant shock loading plasticity models

A review of relevant strain rate dependent plasticity models has been carried out and is presented in this chapter. The chapter begins with discussion of the older, widely used and publicised shock plasticity models, for which many of the more recent works build upon, followed by a discussion of the more recently developed shock plasticity models. The chapter is concluded with a discussion of the proposed method for developments in this work.

As is seen in Figure 1-1 and discussed in chapter 1 the flow stress of a material is dependent on the strain rate by a variable degree, depending on the magnitude of the strain rate. Therefore, modelling at high strain rates requires the flow rules to incorporate rate effects.

2.1.1 Steinberg-Guinan model

The first significant high strain rate model was developed in 1980 by Steinberg and Guinan (Steinberg, et al., 1980). The Steinberg-Guinan model is a fully empirical, high strain rate model which makes use of the fact that at very high strain rates, the effect of the strain rate on the yield strength becomes insignificant in comparison strain and temperature effects. This can be seen in Figure 1-1 to be in the third regime, with the lower limiting strain rate of $10^5 s^{-1}$.

Evolution of the yield surface is given by equation (2.1).

$$Y = Y_0 \left\{ 1 + \left(\frac{Y_p^{'}}{Y_0} \right) \frac{p}{\eta^{1/3}} + \left(\frac{G_T^{'}}{G_0} \right) (T - 300) \right\} (1 + \beta\varepsilon)^n \qquad (2.1)$$

Where: Y is yield strength, Y_0 is the yield stress constant, $Y_p^{'}$ is the pressure dependent yield component, G_0 is the shear modulus, $G_T^{'}$ is the temperature dependent shear modulus, and β is a material constant.

It is seen in equation (2.1) that the yield surface is a function of pressure, temperature and strain. The yield surface is independent of the strain rate, resulting in the model only being applicable at strain rates above 10^5 s^{-1}.

2.1.2 Johnson-Cook model

Further to the Steinberg-Guinan model, in 1983 a model was published by Johnson and Cook (Johnson & Cook, 1983) to model rate dependent plasticity. Similar to the Steinberg-Guinan model, the Johnson-Cook model is a simple, fully empirical model. Evolution of the yield surface controlled by a sum of three terms; the three terms account for the dependence of the yield strength on the strain, the strain rate and the temperature, as can be seen in equation :

$$\sigma_y\left(\varepsilon_p,\dot{\varepsilon}_p,T\right)=\left[A+B\left(\varepsilon_p\right)^n\right]\left[1+C\ln\left(\dot{\varepsilon}_p^*\right)\right]\left[1-\left(T^*\right)^m\right] \tag{2.2}$$

Where σ_y is the flow stress, ε_p is the effective plastic strain, $\dot{\varepsilon}_p^*$ and T^* are normalised plastic strain rate and normalised temperature, respectively, and A,B,C,m,n are material constants.

Due to the strain rate dependence of the yield surface, the Johnson-Cook model is applicable over a larger range of strain rates, and even remains valid for quasi-static analysis.

The Johnson-Cook model is still a widely used model, in part due to the requirement of only 5 material constants, which are available for a wide range of materials in literature.

2.1.3 Zerilli – Armstrong

In 1987 a model based on simplified dislocation mechanics was proposed by Zerilli and Armstrong (Zerilli & Armstrong, 1987). The Zerilli-Armstrong model is based on the thermally activated motion of dislocations, and as such is a physically based model. Similar to the Johnson-Cook and Steinberg-Guinan models, evolution of plasticity is dependent on the strain, the strain rate and

temperature. However, a distinguishing feature of this model is the fact that two microstructurally based constitutive equations are used, depending on the material structure. This is due to the observation that a BCC metal exhibits a much greater dependence on the strain rate and temperature than it does on the strain. The evolution of the yield strength is for FCC metals by equation (2.3) and for BCC metals by equation (2.4).

$$\sigma = \sigma_G + C_2 \varepsilon^{1/2} \exp\left(-C_3 T + C_4 T \ln \dot{\varepsilon}\right) \tag{2.3}$$

$$\sigma = \sigma_G + C_1 \exp\left(-C_3 T + C_4 T \ln \dot{\varepsilon}\right) + C_5 \varepsilon^n \tag{2.4}$$

Where σ is flow stress, σ_G is the athermal component of flow stress, ε is strain, $\dot{\varepsilon}$ is strain rate, T is temperature and $C_1, C_2, C_3, C_4, C_5, n$ are material parameter that depend on the structure of the material.

2.1.4 MTS model

The next significant model was developed in 1988 by Follansbee and Kocks (Follansbee & Kocks, 1988) and is widely referred to as the Mechanical Threshold Stress (MTS) model. The MTS model provides a scalar valued flow stress which is a function of the strain rate and temperature.

The model is physically based, with dislocation mechanics the basis of the model; and two key assumptions:

i) Viscous drag effects are small in comparison to the thermally activated dislocation motion.
ii) High temperature diffusion effects are absent

As a result of the first assumption, thermally activated dislocation motion is used to describe the flow stress evolution. This assumption also limits the MTS model to strain rates below 10^4 s^{-1}, as at strain rates above 10^4 s^{-1} viscous drag effects become dominant.

The mechanical threshold stress, σ_{MTS}, is provided by equation (2.5) as a sum of parts: an athermal term, σ_a, which is used to describe the rate independent

interactions of dislocations with long range barriers and the thermally part, which accounts for interactions with short range barriers..

$$\sigma_{MTS} = \sigma_a + \frac{\mu}{\mu_0}\left(\hat{\sigma} - \sigma_a\right) s\left(T, \dot{\varepsilon}_p\right) \tag{2.5}$$

Where $\hat{\sigma}$ is the plastic evolution parameter, $s(T, \dot{\varepsilon}_p)$ is the thermal activation factor, which is a function of both temperature, T, and plastic strain rate, $\dot{\varepsilon}_p$.

The athermal componenis calculated via the following relation:

$$\sigma_a = M\left(\sigma_0 + k_y d^{-n}\right) \tag{2.6}$$

Where M is the Taylor orientation factor, σ_0 is the friction stress, d is grain diameter and k_y and n are fitting constants.

The thermal activation factor is given as:

$$s\left(\dot{\varepsilon}, T\right) = \left[1 - \left(\frac{k_B T \ln\left(\frac{\dot{\varepsilon}_0}{\dot{\varepsilon}_p}\right)}{G b^3 g_0}\right)^{\frac{1}{q}}\right]^{\frac{1}{p}} \tag{2.7}$$

Where k_B is the Boltzmann constant, $\dot{\varepsilon}_0$ is a reference strain rate, G is the shear modulus, b is Burgers vector, g_0 is the normalised activation energy and p and q are micromechanical constants.

Unlike the relatively simpler Steinberg-Guinan, Johnson-Cook and Zerilli-Armstrong models discussed about, a large number of material parameters, 29, are required for modelling with the MTS model. The parameters required for the MTS model are outlined in Table 2-1 However, studies (Panov, 2006) have shown that the MTS model holds some advantages over the Johnson-Cook and Zerlli-Armstrong models, most notably it is accurate over a wider range of strains.

Table 2-1: Outline of the 29 parameters required for modelling with the MTS model

Symbol	Description
$\hat{\sigma}_a$	Dislocation interaction – long range barriers
$\hat{\sigma}_i$	Dislocation interaction – interstitial atoms
$\hat{\sigma}_s$	Dislocation interaction – solute atoms
$\hat{\sigma}$	Initial flow stress
a_0, a_1, a_2	First, second and third dislocation generation constants
$\hat{\sigma}_{s0}$	Saturation threshold stress
b	Magnitude of Burgers vector
A	Material constant
k_B	Boltzmann constant
b_0	Shear modulus at 0K
b_1, b_2	First and second shear modulus constants
G_0	Normalised activation energy for dislocation – dislocation interactions
$\dot{\varepsilon}_{so}, \dot{\varepsilon}_0, \dot{\varepsilon}_{0,i}, \dot{\varepsilon}_{0,s}$	Reference strain rates
$\frac{1}{p}, \frac{1}{p_i}, \frac{1}{p_s}$	Material constants
$\frac{1}{q}, \frac{1}{q_i}, \frac{1}{q_s}$	Material constants
$G_{0,s}$	Normalised activation energy for a dislocation/solute interaction
$G_{0,i}$	Normalised activation energy for a dislocation interstitial interaction
ρC_p	Density heat capacity
T	Temperature

The MTS model is widely used, for example in (Banerjee & Bhawlkar, 2008) and (Djordjevic, 2011). Significantly, in (Djordjevic, 2011) the MTS model is modified for use in modelling orthotropic metals under high strain rate loading, which is a work that this work largely builds upon. However, MTS based models are unable to capture the superelastic precursor behaviour that this work is focussing on therefore it is required to investigate different modelling methods for the success of this work.

More recently works by Khan (Khan & Liu, 2016) (Khan, et al., 2015) , and Hansen (Hansen, et al., 2013) have utilised thermal activation of dislocations in modelling. However, when considering dislocation motion, it is widely observed that at strain rates higher than about 10^5 s^{-1} thermal activation is superseded by viscous drag effects as the dominant process controlling dislocation motion. Therefore, it is necessary for dislocation dynamics based models to be developed to accurately model over higher strain rates and subsequently thermal activation models are discounted from this work. .

2.2 Orowan equation based modelling

It is seen in Figure 2-1 that the time scales of interest in this work is the nanosecond timescale over which the precursor wave amplitude decays. Figure 2-1 shows that when modelling, the time and length scales required scale accordingly. Therefore, to accurately capture behaviour over the nanosecond time scale, it is imperative to give proper consideration to the microscale processes governing plasticity.

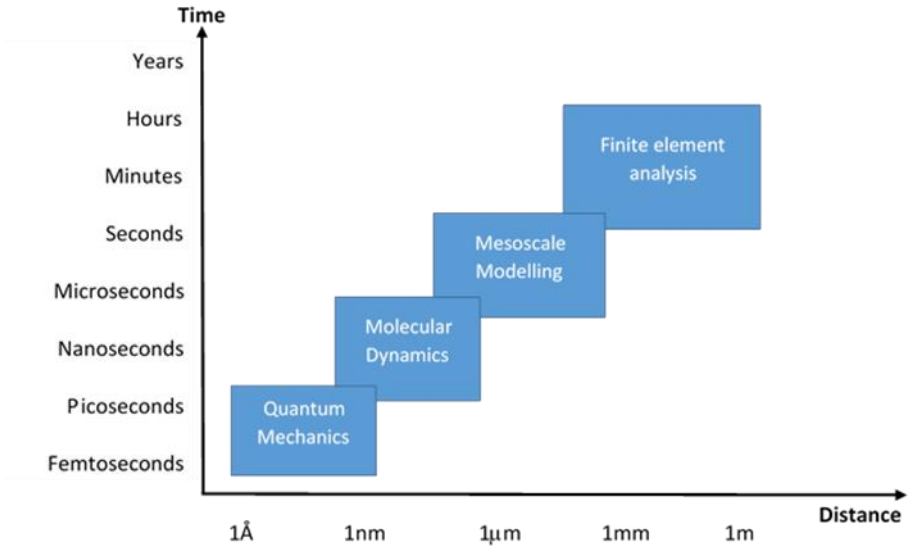

Figure 2-1: Graph showing the time and length scales applicable to different modelling methods

The Orowan equation provides a convenient method of achieving this. The Orowan equation, equation (2.8), provides a method of calculating the continuum scale plastic strain rate from the dislocation scale variables.

$$\dot{\varepsilon}_p = bv\rho_m \tag{2.8}$$

It is seen in equation (2.8) that the plastic strain rate is determined by the product of the magnitude of Burgers vector, b, the velocity of mobile dislocations, v, and the density of mobile dislocations ρ_m. Numerous model have been developed utilising the Orowan equation, for example (Groh, et al., 2009) (Colvin, et al., n.d.) (Hansen, et al., 2013) (Luscher, et al., 2016) (Malygin, 1999) (Mayeur, et al., 2016) (Mayer, et al., 2013), with the unique features in each being the equations governing the evolution of the dislocation based variables.

Two models were identified in (Kiely, 2013) as being of particular interest to this work; both models combined processes occurring on the microscale with the development of deformation on the continuum scale. The first method investigated was that developed by Malygin (Malygin, 1999). In this method a series of dislocation kinetic equations are developed, with evolution equation

developed dislocation densities of various origins. This results in a large number of internal variables, resulting in an extremely computationally expensive model.

2.2.1 Mayer's model

The second model investigated was developed by Mayer (Mayer, et al., 2013) (Krasnikov, et al., 2010) (Krasnokov, et al., 2011). The model uses three internal state variables to evolve plasticity; the density of mobile dislocations, the density of immobile dislocations and the velocity of mobile dislocations. The three internal state variables evolve by the use of dislocation dynamics based equations.

Firstly, the density of mobile dislocations is evolved by the following constitutive relation:

$$\frac{d\rho_D^\beta}{dt} = Q_D^\beta - Q_I^\beta - k_a b \left| V_D^\beta \right| \rho_D^\beta \left(2\rho_D^\beta + \rho_I^\beta \right) \tag{2.9}$$

Where: ρ_D^β is the density of mobile dislocations, Q_D^β is the rate of generation of new mobile dislocations, Q_I^β is the rate of immobilisation of mobile dislocations, k_a is a coefficient of annihilation, b is the magnitude of Burgers vector and V_D^β is the velocity of mobile dislocations. The superscript β 's indicate that values are for each slip system.

This can be interpreted physically as, the rate of change of mobile dislocation is equal to the rate of generation of new mobile dislocations, formed using plastically dissipated energy, minus the number of dislocations immobilised into structures via dislocation interactions, minus the number of dislocations lost to annihilation with other dislocations.

Next, evolution of the immobile dislocation density is achieved by the relation:

$$\frac{d\rho_I^\beta}{dt} = Q_I^\beta - k_a b \left| V_D^\beta \right| \rho_D^\beta \rho_I^\beta \tag{2.10}$$

It can be seen that similar to equation (2.9), the evolution of the immobile dislocation density can physically be interpreted as the increasing by the same

number of mobile dislocations lost to immobilisation, minus the annihilation of previously immobilised dislocations with other mobile dislocations.

Finally, the velocity of mobile dislocations is determined via the dislocation equation of motion:

$$m_0 \zeta_\beta^3 \frac{dV_D^\beta}{dt} = \left[\sum_{i=1}^{N} \sum_{k=1}^{N} S_{ik} b_i^\beta n_k^\beta \pm \frac{1}{2} bY \right] - B\zeta_\beta^3 V_D^\beta \tag{2.11}$$

Where: m_0 is the effective mass of dislocations, S_{ik} are the mechanical stress components driving dislocation motion, n_k is the vector normal to the slip plane, Y is the yield strength and B is a coefficient of dynamic drag.

Here, the equation of motion is comparable to Newton's second law of motion, whereby the acceleration of dislocations is written in terms of a sum of the forces acting on the dislocations. The forces accounted for in the equation of motion are the driving force from the mechanical stress tensor, minus the resistive forces in the form of the inherent lattice resistance and the dynamic drag forces.

Work hardening in the model is controlled by the immobile dislocation density via the relation:

$$Y = Y_0 + A_I G b \sqrt{\rho_I} \tag{2.12}$$

Where: Y_0 is the resistance due to Peierls barrier, A_I is a coefficient of hardening and G is the shear modulus.

The mobile dislocation density and the dislocation velocity are used to determine the rate of plastic strain via Orowans equation.

The model proposed by Mayer was identified as being of significant interest in this work as it is a dislocation dynamics based model, which uses the Orowan equation to feed microscale variables up to the continuum scale, while providing information regarding the state of the microstructure of the material. This is advantageous to aiding the understanding of the underlying processes driving plasticity during shock deformation. Unlike the Malygin model (Malygin, 1999),

only the overall densities of dislocations are considered on each slip system, the origin and separate dislocation processes are not considered. This is advantageous as it maintains computational efficiency.

The other key feature of the model is its published ability to capture super elastic precursor behaviour, which is a key motivation for this work. Initial published results, as seen in Figure 1-2 clearly demonstrate the models ability to capture this behaviour. Limitations of the Mayer model

Despite the above mentioned advantages of the Mayer model, the model in its published form has some limitations which require improvement for use in a hydrocode. Firstly, the published model is a 1D model, where a single stress component is calculated, not the full stress tensor. This 1D version of the model has been used to model plate impact, successfully predicting superelastic behaviour, however further work was required to fully implement this in the hydrocode.

Secondly, the model has only been tested for the use of modelling single crystal FCC metals. The modelling of single crystal BCC metals is of significant interest to this work in addition to FCC metals. It is widely acknowledged that the yielding of BCC metals is somewhat more complicated than that of FCC metals, therefore further investigation and development is required for full use.

Finally, little detail is provided in literature regarding the determination of the material parameters required for the model, of which there are 9. Therefore full parametric investigation of the model is required before the range of materials it is applicable for can be extended.

Despite the limitations highlighted above, the Mayer model is the only model observed in literature to successfully capture superelastic behaviour and therefore the model is chosen as a basis for the development of this work. Full mathematical details of the Mayer model are described in chapter 6.

3 Continuum Mechanics framework for modelling

The foundations of continuum mechanics are outlined in this chapter. The chapter introduces and defines the key concepts of continuum mechanical modelling, before defining the framework required for modelling slip deformation, which is used in the development of the new material model.

A continuum approach considers the material being modelled to be continuously distributed in space. A continuum is considered to be a continuous medium in which the material has properties averaged over representative volume at each point (Mase, 1970). In order for this to hold true the size of the representative volume must be large enough for the discrete nature of the material structure (e.g. individual atoms) not be apparent. Eliminating the need to model material discrete structure significantly reduces the complexity of modelling. This section will introduce the required relationships and concepts of continuum mechanics used in material modelling.

First, the basics of deformation kinematics are introduced. In this it is important to define a reference configuration. A deforming material is regarded to be in a current configuration. However in order to measure deformations a reference configuration relative to which deformation is measured has to be defined. It can be the initial configuration of the material, prior to any motion or deformation, or it can be an imaginary configuration which the material does not achieve during the motion.

Motion is described by the mapping of a point in the reference configuration to a corresponding point in the current configuration. This can be done by consideration of a point X in the reference configuration with position vector **X**. After deformation the point will be at position vector **x** in the current configuration, and for convenience shall be called point x. The mapping from **X** to **x** is achieved through the motion

$$\mathbf{x} = \chi\left(\mathbf{X}, t\right) \tag{3.1}$$

where χ is the motion. It is a time dependent vector valued vector function (Holzapfel, 2000). The inverse motion can be calculated, mapping point x in the current configuration back to point X in reference configuration.

$$\mathbf{X} = \chi^{-1}(\mathbf{x}, t) \tag{3.2}$$

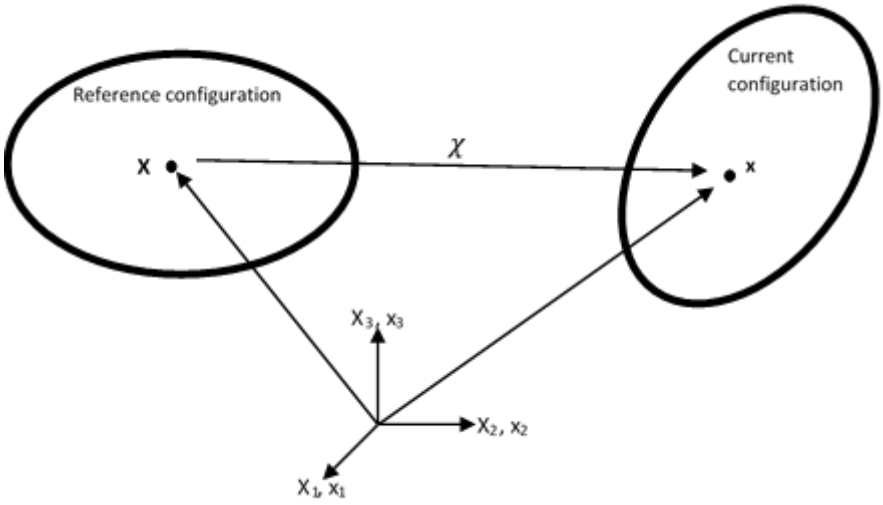

Figure 3-1: Diagram showing the mapping of a point in the reference configuration to a point in the current configuration via the motion.

3.1 Deformation measures

The principal deformation measures used in this work are introduced here.

The deformation gradient is a measure of deformation between the reference and current configurations and is arrived at by partial differentiation of equation (3.1) with respect to X.

$$d\mathbf{x} = \frac{\partial \mathbf{x}}{\partial \mathbf{X}} d\mathbf{X} \tag{3.3}$$

Where

$$\mathbf{F} = \frac{\partial \mathbf{x}}{\partial \mathbf{X}} = \frac{\partial \chi(\mathbf{X})}{\partial \mathbf{X}} = Grad\mathbf{x}(\mathbf{X}) \tag{3.4}$$

is the deformation gradient. The uppercase $Grad$ in equation (3.4) indicates that the deformation gradient is taken with respect to the reference coordinates **X**. If the deformation is being mapped back from the current to the reference configuration, then the deformation gradient is taken with respect to the current coordinates and is shown in equation (3.5).

$$\mathbf{F}^{-1} = \frac{\partial \chi^{-1}(\mathbf{X})}{\partial \mathbf{x}} = grad\mathbf{X}(\mathbf{x}) \tag{3.5}$$

The lowercase $grad$ in the grad term in equation (3.5) indicates that the gradient is taken with respect to the current configuration.

The change of volume between the reference and current configurations is given by the determinant of the deformation gradient tensor and is commonly referred to as the Jacobian

$$dv = \det \mathbf{F} dV = J(\mathbf{X}, t) dV \tag{3.6}$$

As mass is conserved during deformations, the Jacobian can be shown to relate the densities in the reference and current configurations.

$$\frac{\rho}{\rho_0} = J^{-1} \tag{3.7}$$

3.2 Polar Decomposition

One of the fundamental relations in continuum mechanics is polar (multiplicative) decomposition of the deformation gradient. This means that the deformation gradient can be split into an elongation term and a rotational term as shown in equation (3.8).

$$\mathbf{F} = \mathbf{RU} = \mathbf{vR} \tag{3.8}$$

Where $\mathbf{U}$ and $\mathbf{v}$ are unique positive definite, symmetric tensors. $\mathbf{U}$ is referred to as the right (symmetric, material) stretch tensor and $\mathbf{v}$ the left (symmetric, spatial) stretch tensor. $\mathbf{R}$ is an orthonormal tensor of rotation. This decomposition shows that when deformation occurs, both elongation and rotation occur.

3.3 Nansons Formula

To map a unit vector normal to an infinitesimal surface element in the reference configuration to a unit vector normal to an infinitesimal surface element in the current configuration the deformation gradient cannot be used (Holzapfel, 2000). Instead a useful relationship called the Nanson's formula is used. The formula is defined as:

$$d\mathbf{s} = J\mathbf{F}^{-T} d\mathbf{S} \tag{3.9}$$

Where

$$d\mathbf{s} = ds\mathbf{n} \tag{3.10}$$

$$d\mathbf{S} = dS\mathbf{N} \tag{3.11}$$

and ds and dS are the surface elements in the reference and current configurations, and $\mathbf{n}$ and $\mathbf{N}$ are the unit vectors normal to the surfaces.

Nansons formula has use during the derivation of different types of stress tensors.

3.4 Cauchy-Green deformation tensors

As well as the deformation gradient, other deformation measures and strain tensors are used. A good starting point is the product of the deformation gradient with the transpose of itself $\mathbf{F}^T\mathbf{F}$.

From here two deformation tensors can be derived, the right Cauchy-Green tensor

$$\mathbf{C} = \mathbf{F}^T\mathbf{F} = \mathbf{C}^T \tag{3.12}$$

and the left Cauchy-Green tensor

$$\mathbf{b} = \mathbf{F}\mathbf{F}^T \tag{3.13}$$

The right Cauchy-Green tensor, $\mathbf{C}$, represents the change in squared length of the element dX and is defined with respect to the reference configuration. The left Cauchy-Green tensor, $\mathbf{b}$, represents the change in squared length of the element dx and is defined with respect to the current configuration.

The deformation tensors 3.12 and 3.13 can be linked to the stretch tensors $\mathbf{U}$ and $\mathbf{v}$ arising during the polar decomposition of the deformation gradient. The stretch tensors are related to the Cauchy-Green deformation tensors via equations (3.14) and (3.15).

$$\mathbf{C} = \mathbf{F}^T\mathbf{F} = \mathbf{U}^2 \tag{3.14}$$

$$\mathbf{b} = \mathbf{F}\mathbf{F}^T = \mathbf{v}^2 \tag{3.15}$$

The Cauchy-Green deformation tensors are useful measures, however in the un-deformed configuration, equations (3.12) and (3.13) reduce to identity. More usefully, they can be used to derive strain tensors which reduce to zero in the un-deformed configuration, making the constitutive equations less complicated.

3.5 Green-Lagrange strain tensor

The strain measured in terms of material variables can be expressed by the Green-Lagrange strain tensor

$$\mathbf{E} = \frac{1}{2}\left(\mathbf{F}^T\mathbf{F} - \mathbf{1}\right) \tag{3.16}$$

The Green-Lagrange strain can be related to the Cauchy-Green deformation tensors and the elongation tensor by substituting equation (3.14) into equation (3.16) giving

$$\mathbf{E} = \frac{1}{2}\left(\mathbf{C} - \mathbf{1}\right) = \frac{1}{2}\left(\mathbf{U}^2 - \mathbf{1}\right) \tag{3.17}$$

3.6 Euler-Almansi strain tensor

When the squared lengths are measured in terms of spatial variables, the resulting strain tensor is the Euler-Almansi tensor.

$$\boldsymbol{\varepsilon} = \frac{1}{2}\left(\mathbf{1} - \mathbf{F}^{-T}\mathbf{F}^{-1}\right) \tag{3.18}$$

The Euler-Almansi tensor can be related to the left Cauchy-Green tensor and the stretch tensor by substituting equations (3.12) and (3.13) into equation (3.18).

$$\boldsymbol{\varepsilon} = \frac{1}{2}\left(\mathbf{1} - \mathbf{b}^{-1}\right) = \frac{1}{2}\left(\mathbf{1} - \left(\mathbf{v}^{-1}\right)^2\right) \tag{3.19}$$

The Green-Lagrange and Euler-Almansi strain tensors are linked by relation (3.20).

$$\mathbf{E} = \frac{1}{2}\left(\mathbf{F}^T\mathbf{F} - \mathbf{1}\right) = \mathbf{F}^T\,\frac{1}{2}\left(\mathbf{1} - \mathbf{F}^{-T}\mathbf{F}^{-1}\right)\mathbf{F} = \mathbf{F}^T\boldsymbol{\varepsilon}\mathbf{F} \tag{3.20}$$

3.7 Deformation rate measures

Taking the first derivative of the position vector $\mathbf{x}$ in the spatial description results in the spatial velocity. By taking the derivative of this with respect to the spatial coordinates yields the spatial velocity gradient:

$$\mathbf{l}(\mathbf{x},t) = \frac{\partial \mathbf{v}\left(\mathbf{x},t\right)}{\partial \mathbf{x}} = grad\mathbf{v}\left(\mathbf{x},t\right) \tag{3.21}$$

By putting the spatial velocity in terms of the motion, and then applying the chain rule, the spatial velocity gradient can be shown in terms of the deformation gradient

$$\mathbf{l} = \dot{\mathbf{F}}\mathbf{F}^{-1} \tag{3.22}$$

Importantly, the spatial velocity gradient can be additively decomposed as in equation (3.23).

$$\mathbf{l}\left(\mathbf{x},t\right) = \mathbf{d}\left(\mathbf{x},t\right) + \mathbf{w}\left(\mathbf{x},t\right) \tag{3.23}$$

Where

$$\mathbf{d}\left(\mathbf{x},t\right) = \frac{1}{2}\left(\mathbf{l} + \mathbf{l}^T\right) \tag{3.24}$$

$$\mathbf{w}\left(\mathbf{x},t\right) = \frac{1}{2}\left(\mathbf{l} - \mathbf{l}^T\right) \tag{3.25}$$

The tensors $\mathbf{d}$ and $\mathbf{w}$ are the symmetric and skew-symmetric parts of the spatial velocity gradient respectively. The symmetric part, $\mathbf{d}$, is referred to as the rate of deformation tensor and the skew-symmetric part, $\mathbf{w}$, is the rate of rotation tensor.

Similarly the material velocity gradient can be obtained by taking the material time derivative of the deformation gradient

$$\dot{\mathbf{F}} = \frac{\partial}{\partial t}\left(\frac{\partial \boldsymbol{\chi}(\mathbf{X},t)}{\partial \mathbf{X}}\right) = \frac{\partial}{\partial \mathbf{X}}\left(\frac{\partial \boldsymbol{\chi}(\mathbf{X},t)}{\partial t}\right) = \frac{\partial \mathbf{V}(\mathbf{X},t)}{\partial \mathbf{X}} = Grad\mathbf{V}(\mathbf{X},t) \qquad (3.26)$$

3.8 Intermediate and isoclinic configurations

As a load is applied to the materials of interest is this work, deformation occurs. Three main types of deformation occur in metals; elastic deformation, plastic deformation and damage. Elastic deformation forms the Hooke's law region of a stress-strain plot, which for a metal is a straight line region with the strain being directly proportional to the stress. Plastic deformation occurs when the applied stress reached the yield point of the material. For a metal this is observed to be the point on a stress-strain plot where the straight line region ends and a curve begins to develop. Upon unloading, the plastic deformation will remain in the material. An important property of plastic deformation is that it does not affect the elastic properties of the material.

In a real, physical experiment, both of these modes of deformation will be observed simultaneously. When modelling the deformations however, it is convenient to consider each type separately. In reality this is not achievable, i.e. a material cannot undergo plastic deformation without some degree of elastic deformation. For the purpose of modelling this the concept of multiplicatively decomposing the deformation gradient as well as intermediate configurations need to be introduced.

Equation (3.27) shows how the deformation gradient is decomposed as presented in (Djordjevic, 2011).

$$\mathbf{F} = \frac{\partial \mathbf{x}}{\partial \mathbf{X}} = \frac{\partial \mathbf{x}}{\partial \mathbf{x}_p}\frac{\partial \mathbf{x}_p}{\partial \mathbf{X}} = \mathbf{F}_e\mathbf{F}_p \qquad (3.27)$$

Where $\mathbf{F}_e$ is the elastic part of the deformation gradient, and $\mathbf{F}_p$ is the inelastic, or plastic, part of the deformation gradient.

Making use of the multiplicatively decomposed deformation gradient, an intermediate configuration becomes apparent when considering a deformation.

It is usual to map between the initial and current configurations, however to reach the current configuration all types of deformation need to be included. Considering the decomposition in equation (3.27), a two stage deformation process can be written as shown in Figure 3-2.

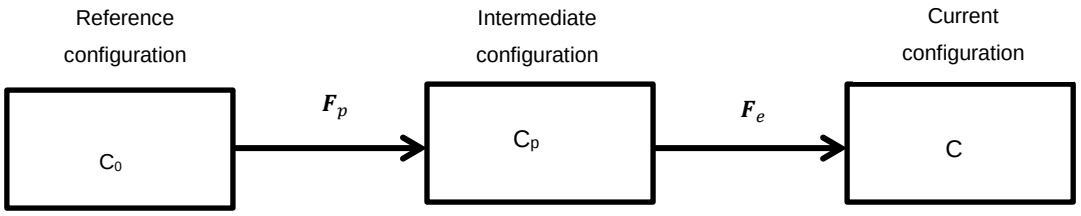

Figure 3-2: Link between the decomposed deformation gradient and the reference, intermediate and current configurations.

Figure 3-2 shows three configurations: the initial configuration, C_0, the current configuration, C, and an intermediate configuration, C_p. The initial and current configurations are as described previously in section 3-1, and the intermediate configuration is caused due to the consideration of the deformation processes separately. The intermediate configuration shown in Figure 3-2 can be considered as an elastically released configuration; only plastic deformation is present.

Additionally, the deformation gradient can be decomposed into stretch and rotational parts, as shown previously in section 3.2. The same decomposition can be applied to the multiplicatively decomposed deformation gradient resulting in a rigid body rotation associated with each stage of the deformation. Due to this, the elastically released intermediate configuration is not uniquely defined. This is overcome by the introduction of the isoclinic configuration. The isoclinic configuration is similar to the intermediate configuration, in that it is elastically relaxed, however, it is uniquely defined by the removal of the rigid body rotation caused during plastic deformation, $\mathbf{R}_p$.As $\mathbf{R}_p^{-1} = \mathbf{R}_P^T$, removal of the plastically induced rotation to map from the intermediate to isoclinic configuration is done

via the transpose ($\mathbf{R}_P^T$) of $\mathbf{R}_p$. Physically, the isoclinic configuration is not achievable, but it is a very useful concept for modelling as it is uniquely defined.

Figure 3-3 shows the relationship between the initial configuration, the elastically released intermediate configuration, the current configuration and the isoclinic configuration, $\tilde{C}_p$.

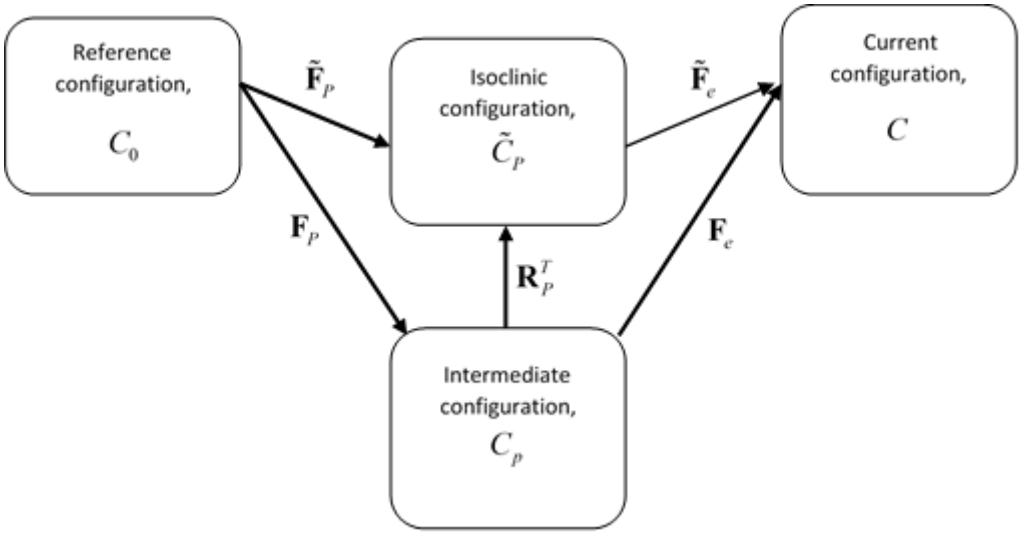

Figure 3-3: Diagram showing the links between the reference, intermediate, isoclinic and current configurations.

3.9 Stress

Stress in a continuum can be described by considering the forces on an infinitesimal surface element on an imaginary plane cutting through the continuum. The force on the infinitesimal surface area, ds, is described by a traction vector, $\boldsymbol{t}$. The traction vector represents the force per unit area with the same direction as the force is acting. Stress tensor arise from this due to Cauchy's stress theorem which states: "there exist unique second-order tensor fields $\boldsymbol{\sigma}$ and $\boldsymbol{P}$ so that

$$\mathbf{t}(\mathbf{x},t,\mathbf{n}) = \boldsymbol{\sigma}(\mathbf{x},t)\mathbf{n} \tag{3.28}$$

$$\mathbf{T}(\mathbf{X},t,\mathbf{N}) = \mathbf{P}(\mathbf{X},t)\mathbf{N} \tag{3.29}$$

Where $\boldsymbol{\sigma}$ denotes a symmetric spatial tensor field called the Cauchy stress tensor, while $\boldsymbol{P}$ characterizes a tensor field called the first Piola-Kirchhoff stress tensor" (Holzapfel, 2000). It should be noted that the traction vector $\boldsymbol{t}$ is representative of the surface tractions in the current configuration, whereas $\boldsymbol{T}$ is a function of the referential configuration.

The Cauchy stress and the first Piola-Kirchhoff stress are related by equation (3.30).

$$\boldsymbol{\sigma} = J^{-1}\mathbf{P}\mathbf{F}^{T} \tag{3.30}$$

There are many other stress tensors that have been defined in literature, however two are of particular interest in this work; these are the so called second Piola-Kirchhoff stress and the Mandel stress.

The second Piola-Kirchhoff stress is defined by the pull-back operation on the contravarient spatial tensor field, known as the Kirchhoff stress. The Kirchhoff stress is given as

$$\boldsymbol{\tau} = J\boldsymbol{\sigma} \tag{3.31}$$

Where J is the volume ratio and σ is the Cauchy stress tensor.

The second Piola-Kirchhoff stress tensor is now defined as

$$\mathbf{S} = \boldsymbol{\chi}_{*}^{-1}\left(\boldsymbol{\tau}^{\#}\right) = \mathbf{F}^{-1}\boldsymbol{\tau}\mathbf{F}^{-T} \tag{3.32}$$

The subscript $*$ and superscript # in equation (3.32) represent that the second Piola-Kirchhoff stress is achieved by a pull-back operation of the contravariant spatial tensor field.

From the definition of the Kirchhoff stress, equation (3.31), and the relation between the first Piola-Kirchhoff stress and the Cauchy stress, equation (3.30), the second Piola-Kirchhoff stress can be expressed in terms of the Cauchy stress and the first Piola-Kirchhoff stress tensors:

$$\mathbf{S} = J\mathbf{F}^{-1}\boldsymbol{\sigma}\mathbf{F}^{-T} = \mathbf{F}^{-1}\mathbf{P} \tag{3.33}$$

The Mandel stress is a stress tensor which is defined with respect to an intermediate configuration. The Mandel stress tensor can be defined separately in both the intermediate and isoclinic configurations. It is shown in (Djordjevic, 2011) that the Mandel stress is given in the intermediate configuration in terms of Kirchhoff stress and the second Piola-Kirchhoff stress tensor as:

$$\tilde{\boldsymbol{\Sigma}} = \mathbf{F}_e^{-1}\boldsymbol{\tau}\mathbf{F}_e^{-T} = \tilde{\mathbf{C}}_e\tilde{\mathbf{S}} \tag{3.34}$$

And in the isoclinic configuration as:

$$\bar{\boldsymbol{\Sigma}} = \bar{\mathbf{F}}_e^{-1}\boldsymbol{\tau}\bar{\mathbf{F}}_e^{-T} = \bar{\mathbf{C}}_e\bar{\mathbf{S}} \tag{3.35}$$

A relationship exists between the Mandel stress in the intermediate configuration and the Mandel stress in the isoclinic configuration, which is determined by the inelastically induced rotation $\boldsymbol{R}_p$ as:

$$\bar{\boldsymbol{\Sigma}} = \mathbf{R}_p^T\tilde{\boldsymbol{\Sigma}}\mathbf{R}_p \tag{3.36}$$

In general, the Mandel stress is asymmetric. However, for a model modelling small elastic but large plastic deformation, a behaviour which is observable with most metals, the Mandel stress becomes symmetric.

3.10 Kinematics of slip deformation

Following the continuum mechanical foundations presented above, the kinematics of slip deformation are now discussed. This forms the framework for the new material model.

In the framework of thermodynamics and configurational mechanics, kinematics of deformation at the continuum level is defined in terms of multiplicative decomposition of deformation gradient given as:

$$\mathbf{F} = \mathbf{F}_e\mathbf{F}_p \tag{3.37}$$

where: $\mathbf{F}_e$ represents thermo-elastic part of the deformation, and $\mathbf{F}_p$ represents the part of the deformation due to plastic deformation (dislocation mechanics). The decomposition (3.37) introduces an intermediate, elastically unloaded

configuration, which is stress free at a reference temperature and can be physically obtained by elastic unloading of material. For the sake of compatibility with the orthotropic material properties, the model developed in this work is integrated in isoclinic intermediate configuration, which can be obtained from the elastically unloaded configuration by rotating back for the plastically induced rigid body rotation, as described in (Vignjevic, et al., 2012). The material directions in the isoclinic configuration remain unchanged and corresponding multiplicative decomposition is defined as:

$$\mathbf{F} = \mathbf{F}_e \mathbf{F}_p = \mathbf{F}_e \mathbf{R}_p \mathbf{R}_p^T \mathbf{F}_p = \bar{\mathbf{F}}_e \bar{\mathbf{F}}_p \tag{3.38}$$

Where polar decomposition of plastic part of deformation gradient introduced the orthogonal tensor of rotation $\mathbf{R}_p$, which is used to obtain the elastic and plastic part of deformation gradient in isoclinic configuration: $\bar{\mathbf{F}}_e = \mathbf{F}_e \mathbf{R}_p$, $\bar{\mathbf{F}}_p = \mathbf{R}_p^T \mathbf{F}_p = \mathbf{R}_p^T \mathbf{R}_p \mathbf{U}_p = \mathbf{U}_p$. Green Lagrange strain pushed forward to the isoclinic configuration is additively decomposed as:

$$\bar{\mathbf{E}} = \bar{\mathbf{F}}_p^{-T} \mathbf{E} \bar{\mathbf{F}}_p^{-1} = \frac{1}{2}\left(\bar{\mathbf{F}}_e^T \bar{\mathbf{F}}_e - \mathbf{I}\right) + \bar{\mathbf{F}}_p^{-T} \left(\frac{1}{2}\left(\bar{\mathbf{F}}_p^T \bar{\mathbf{F}}_p - \mathbf{I}\right)\right) \bar{\mathbf{F}}_p^{-1} = \bar{\mathbf{E}}_e + \bar{\mathbf{E}}_p \tag{3.39}$$

Equally, velocity gradient pulled back to the isoclinic configuration leads to additive decomposition defined as:

$$\bar{\mathbf{l}} = \bar{\mathbf{F}}_e^{-1} \mathbf{l} \bar{\mathbf{F}}_e = \bar{\mathbf{F}}_e^{-1} \dot{\mathbf{F}}_e + \dot{\bar{\mathbf{F}}}_p \bar{\mathbf{F}}_p^{-1} = \bar{\mathbf{l}}_e + \bar{\mathbf{l}}_p \tag{3.40}$$

Where $\bar{\mathbf{l}}_e$ and $\bar{\mathbf{l}}_p$ are respectively elastic and plastic part of the velocity gradient in isoclinic configuration, which can be further divided into symmetric and antisymmetric/spin tensor. Evolution of elastic deformation is determined by elastic part of velocity gradient, whilst plastic part of velocity gradient determines the evolution of plastic deformation. The latter is calculated using the generalised Orowan's equation, which is described in the following subsection.

In the framework of thermodynamics, the velocity gradient in isoclinic configuration is work conjugate variable to Mandel stress $\bar{\boldsymbol{\Sigma}}$ (Mandel, 1972)

(Mandel, 1974) (Vignjevic, et al., 2012), which is defined as a pull back of Kirchhoff stress $\boldsymbol{\tau}$, as:

$$\bar{\boldsymbol{\Sigma}} = \bar{\mathbf{F}}_e^T \boldsymbol{\tau} \bar{\mathbf{F}}_e^{-T} \tag{3.41}$$

Mandel stress tensor can be decomposed into the spherical and deviatoric part, which is in the index and tensor notation respectively given as:

$$\bar{\Sigma}_{ij} = -P\bar{\psi}_{ij} + \bar{S}_{ij} \qquad \bar{\boldsymbol{\Sigma}} = -P\bar{\boldsymbol{\psi}} + \bar{\mathbf{S}} \tag{3.42}$$

Where P is pressure that is work conjugate to volumetric part of strain, $\bar{\psi}_{ij}$ is tensor determined by material elastic orthotropy (Vignjevic, et al., 2008) with the following properties $\bar{\psi}_{ij} \neq 0$ for $\forall\ i = j$ and $\bar{\psi}_{ij} = 0$ for $\forall\ i \neq j$; and $\bar{S}_{ij}$ components of deviatoric stress. Note that the tenor $\bar{\psi}_{ij}$ becomes δ_{ij} for the case of isotropic material formulation.

When modelling the shock response of materials, spherical part of the stress tensor is updated by the equation of state, whilst the deviatoric part is determined by the strength part of the constitutive model, where the assumption was made that only the elastic component of deviatoric part of the strain contributes to the deviatoric stress. Consequently, the generalised constitutive law can be written in the rate form as:

$$\dot{\bar{S}}_{ij} = C_{ijkl} \bar{d}'^{e}_{kl} \qquad \dot{\bar{\mathbf{S}}} = \mathbb{C} \bar{\mathbf{d}}'_e \tag{3.43}$$

where Mandel stress is assumed to be symmetric (Vladimirov, et al., 2009) (Reese & Vladimirov, 2008) , so that deviatoric part of elastic component of the rate of deformation, $\mathbf{d}'_e$ can be obtained from a symmetric part of the additively decomposed velocity gradient:

$$\bar{\mathbf{d}}'_e = \left(\bar{\mathbf{l}} - \bar{\mathbf{l}}_p \right)_{sym} - \frac{1}{3} \bar{\mathbf{d}} : \boldsymbol{\delta} \tag{3.44}$$

3.11 Summary

The basic measures of deformation in a continuum, including the deformation gradient, strain and stress have been defined, along with the important rate measures. The important decompositions of the deformation gradient and the deformation tensors have been defined, before finally the kinematic framework for modelling slip deformation has been developed.

4 Physics of shock waves and relevant continuum and thermodynamic considerations required for modelling

The main focus of this work is the modelling of deformation of metals under shock loading. This chapter outlines the key definitions and physics of shock waves in solids. The chapter starts by defining shock waves and outlining the conditions under which they are generated. This is followed by the mathematical considerations, specifically those relevant in a continuum mechanical framework.

4.1 Shock waves

Shock waves are defined as discontinuities in stress, velocity, density and internal energy (or temperature) with a very sharp leading edge travelling through a medium. Shocks form when high amplitude stress waves overtake stress waves of lower amplitude so the result is a pile up of stress waves travelling as a single, high amplitude discontinuity.

In one-dimension the stress waves are described by the wave equation

$$c^2 \frac{\partial^2 u}{\partial x^2} = \frac{\partial^2 u}{\partial t^2} \tag{4.1}$$

Where the wave speed, c is given by $c = \sqrt{S/\rho}$ and $s = d\sigma/d\varepsilon$, i.e. the slope of the stress strain curve.

It can be seen from the wave equation that the speed of the shock is dependent on the slope of the stress strain curve for the material. A typical stress strain curve shape is shown in Figure 4-1 for a typical non-ferrous metal in the state of uniaxial stress. It is apparent that the slope of the stress strain curve decreases with an increasing stress amplitude. Consequently, that higher amplitude stress waves travel at a slower speed in this regime, therefore higher amplitude stress waves will not overtake lower amplitude waves, resulting in no pile up of waves and consequently no shock wave. It can therefore be concluded that shock waves cannot form in metals in the state of uniaxial stress. It is noteworthy that the elastic region in Figure 4-1 has a steeper slope than tangents after the yield point. This property ensures that, if material is dynamically loaded beyond yield limit, two

stress wave pattern will form with a dispersive plastic wave trailing behind a faster elastic wave.

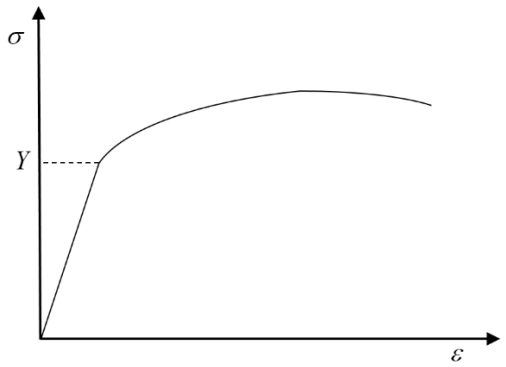

Figure 4-1: Typical stress strain curve of a metal in a state of uniaxial stress

In the case of uniaxial strain i.e. deformation is confined to one-direction only, the material response is somewhat different. A typical stress strain curve for a material in the uniaxial strain regime is shown in Figure 4-2. It is apparent that as plastic deformation progresses, the slope of the curve increases. As a result of this property, applying equation (4.1) it is seen that the speed of stress waves increases with increasing amplitude. This results in higher amplitude waves catching up lower amplitude waves and propagating as a single, steep wave front, i.e. a shock wave. Therefore, the state of uniaxial strain is a condition for shock wave formation.

It is observed in Figure 4-2 that under the conditions of uniaxial strain, there are four different regimes that can be observed. Firstly, when the stress is below the yield point, a single elastic wave is formed, and propagates through the material. The speed of this elastic wave is governed by the slope of the elastic region of the graph following equation (4.1).

The second regime can is observed at point A in Figure 4-2. At point A, the slope of the curve above the yield point decreases. In this case, two waves are formed and propagate through the material; an elastic wave and a plastic shock. The speed of the elastic wave will be determined from the slope of the elastic region of the graph, and the speed of the plastic shock will be determined from the slope of the plastic region of the graph. Therefore, as the gradient of the elastic region

of the graph is greater than at point A, the elastic wave will have a greater speed than the plastic wave, and so will move away from the plastic shock wave. The magnitude of the elastic wave will be determined by the magnitude of the yield stress. When this two wave structure is observed, the shock is common referred to as a weak shock.

The third regime is observed at point B on Figure 4-2. Here, both an elastic and a plastic shock wave will form and propagate, however unlike the case at point A, the speeds of both waves will be the same, so no separation of the waves will be observed. As with the case at point A, the magnitude of the elastic wave will be determined by the elastic limit.

The final regime is typical of that observed at point C on Figure 4-2. Here, the slope of the plastic region of the graph exceeds that of the elastic part, therefore the speed of the plastic wave will exceed the elastic wave. In this case a single plastic shock front will form and propagate, with no elastic wave being observed. The lack of the elastic precursor wave typifies the regime and is commonly referred to as strong shock.

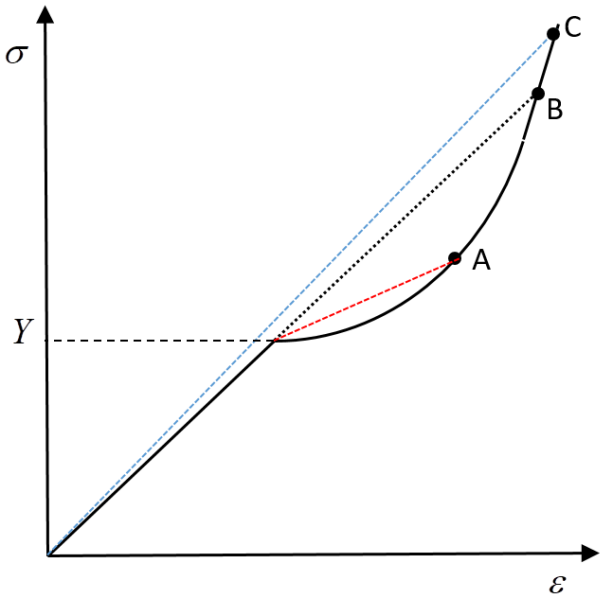

Figure 4-2: Typical stress strain curve for a metal in a state of uniaxial strain.

4.2 Rankine Hugoniot conditions

As a shock propagated through a material, mass, momentum and energy are conserved across the shock discontinuity. This conservation is described by a set of conditions, known as the Rankine – Hugoniot conditions, which relate the state variables either side of the shock discontinuity.

Starting from the conservation of mass, consider a continuous slab of material, with a constant cross section, impacted by a piston at some velocity, as is shown in Figure 4-3 Assuming the piston moves at a constant velocity, as this impacts the material the material at the impacted face begins moving with the same velocity. This onset of material motion results in an increase in material density ahead of the impacted surface, which in turn results in a shock travelling forward at a velocity, U_s.

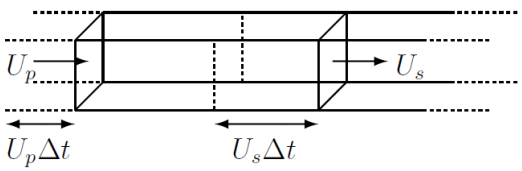

Figure 4-3: Schematic diagram of shock propagation in a slab of material (Park, 2010)

After a short time period, Δt, the shock will have travelled a distance $U_s\Delta t$, and the material behind the shock will have been compressed by an amount $U_p\Delta t$. Therefore, the material behind the shock will now occupy a length of $\left(U_s - U_p\right)\Delta t$. As mass is conserved, the mass contained in the length of the material swept by the shock prior to compression, will be the same as the mass of the compressed length behind the shock. Therefore;

$$\rho_0 A U_s \Delta t = \rho A\left(U_s - U_p\right)\Delta t \tag{4.2}$$

Where ρ_0 is the initial density of the material, A is the cross-sectional area, U_s is the shock velocity, U_p is the particle velocity and ρ is the material density behind the shock.

Making use of the fact that the specific volume is given by $v = \frac{1}{\rho}$, equation (4.2) can be expressed as:

$$\frac{v}{v_0} = \frac{U_s - U_p}{U_s} \tag{4.3}$$

Equation (4.3) shows that the compression, i.e. the change in volume, is given by the shock velocity and particle velocity.

Now, consideration of the conservation of momentum can be used to develop an expression for the pressure change across the shock. The force driving the shock, i.e. the pressure, is by definition equal to the rate of change of momentum. By application of the well known relation, force = mass x acceleration, it can be written:

$$\mathbf{p} = m\frac{d\mathbf{v}}{dt} = \frac{d\left(m\mathbf{v}\right)}{dt} \tag{4.4}$$

In the time period Δt the mass accelerated is equal to that of the material through which the shock has propagated;

$$m = \rho_0 A U_s \Delta t \tag{4.5}$$

With the acceleration being $U_p \big/ \Delta t$

Now the pressure, the force acting per unit area, can be obtained by division of the momentum gain by the cross sectional area, A, resulting in the following relation:

$$P_1 - P_0 = \frac{\rho_0 A U_s \Delta t U_p}{A \Delta t} = \rho_0 U_s U_p \tag{4.6}$$

Similar to the volume change given by equation (4.3), the pressure is given by equation (4.6) in terms of the shock and particle velocities.

A similar approach is taken to develop the expression for the change in energy by equating the work done by the shock wave with the sum of the increase of internal energy and kinetic energy. The work done by the shock is equal to the force driving the shock (i.e. the pressure multiplied by the cross sectional area, PA) multiplied by the distance the mass of material is moved, $U_p \Delta t$. The increase in internal energy is given by the change in specific internal energy, $\Delta E = E_1 - E_0$, multiplied by the mass of material swept by the shock, $m = \rho_0 U_s A \Delta t$, and finally the gain in kinetic energy is given as $\frac{1}{2} m U_p^2$, which result in:

$$\left(P_1 - P_0\right) A U_p \Delta t = \rho_0 U_s A \Delta t \Delta E + \frac{1}{2} \rho_0 U_s A \Delta t U_p^2 \tag{4.7}$$

Which reduces to:

$$\left(P_1 - P_0\right) U_p = \frac{1}{2} \rho_0 U_s U_P^2 + \rho_0 U_S \left(E_1 - E_0\right) \tag{4.8}$$

The three equation, (4.5), (4.6) and (4.8), are known as the Hugoniot conditions. These three relations contain five unknowns: ρ_1, P_1, U_s, U_p and E_1. Using equations (4.6) and (4.8), U_s and U_p can be eliminated from the energy conservation expression, resulting in the following expression.

$$E_1 - E_0 = \frac{1}{2}\left(V_0 - V_1\right)\left(P_1 + P_0\right) \tag{4.9}$$

Equation (4.9) is the Hugoniot equation, which combined with equations (4.5), (4.6) and (4.8) allows for all variables to be calculated provided one is known or measured. The Hugoniot is a material property which represents the locus of all attainable shock states; that is the material state does not pass along the Hugoniot curve during the shock process, rather the curve can be used to determine the endpoint value of the shock.

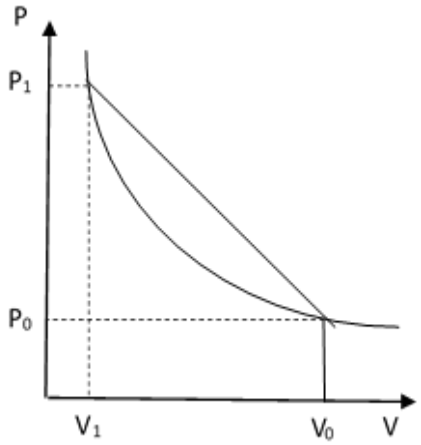

Figure 4-4: Typical Hugoniot curve in the P-V plane with the Rayleigh line showing the loading path

Figure 4-4 shows a typical Hugoniot curve in the P-V plane. As the Hugoniot curve provides only the endpoint value of the shock, the curve does not represent the loading path. This is instead provided by the Rayleigh line, shown in Figure 4-4 as a straight line, over which energy is not constant. An important feature of the Rayleigh line is the fact that its slope is a function of shock speed; faster shocks are described by steeper lines. A key feature of the Hugoniot graph is that the area enclosed by the Hugoniot and the Rayleigh line is equal to the energy dissipated by the shock.

The Hugoniot curve shown in Figure 4-4 is used to determine the jump in a state variable across the shock given knowledge if the other i.e. if the pressure jump is know, the change in volume can be read off of the graph. This is seen by the dashed lines on Figure 4-4, where the jump in pressure from the value P_0 to P_1 correspond to the change in volume from V_0 to V_1.

4.3 Hugoniot Elastic Limit

Additional to an increase in pressure during the shock process, the compression of the material also induces shear stresses. When the amplitude of the compression waves is sufficiently low, the shear stresses are supported by the

material, and no structural change in the material is observed. In this case the material is compressed elastically and will return to its original state upon release. However, as the amplitude of the compression increases, the magnitude of the shear stresses also increase, until the point where the material can no longer support the shear stress and plastic deformation occurs. This point is known as the Hugoniot Elastic Limit (HEL).

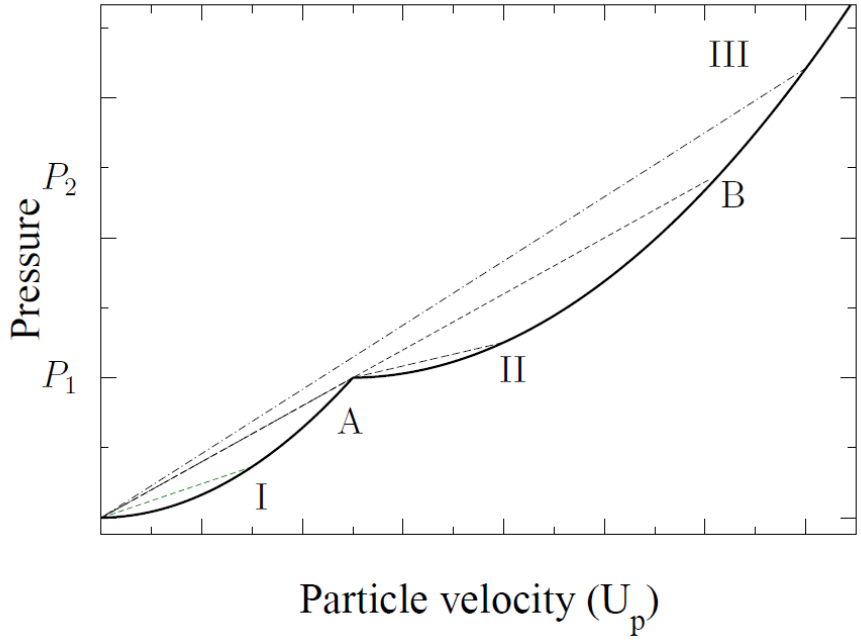

Figure 4-5: Hugoniot curve in the P-U_p plane showing the differing nature of the Rayleigh lines depending on the loading (Park, 2010).

Due to the change in material strength associated with the onset of plastic deformation, different behaviours are observed above a certain pressure, see Figure 4-5. It is seen in Figure 4-5 that the nature of the Rayleigh lines differ for pressures above and below the point P_1. For pressures below P_1 a single Rayleigh line is present, indicating a single wave. When the shock pressure exceeds the value of P_1, typified by the point II on Figure 4-5, it is seen that two distinct Rayleigh lines are now observed. First a steeper line defines the shock until the point of P_1, then a second, less steep line to the point II. Since the slope

of the Rayleigh line is a function of shock speed, this indicates that a two wave structure will propagate through the material; a faster, lower pressure precursor wave propagates, followed by a slower higher pressure wave. This two wave structure is observed until the shock pressure reaches that of point B, at which point the shock speed is equal to that of the precursor, resulting in the two shocks becoming indistinguishable. For shocks of pressures above point B, only a single shock is observed. This is typically referred to as an overdriven shock.

4.4 Shockwaves in Continuum Mechanics

The current mathematical capabilities of shock wave modelling are explored in this section. The mathematical capabilities explored are those from a continuum mechanics point of view. In a continuum a shock wave is treated as a discontinuity of field variables. Despite this discontinuity, balance laws must still be observed.

4.4.1 Basic jump conditions

The balance laws in a normal, smooth continuum are given as:

$$\frac{d}{dt}\int_{R_t}\rho dv = 0 \tag{4.10}$$

$$\frac{d}{dt}\int_{R_t}\rho \mathbf{v} dv = \int_{R_t}\rho \mathbf{b} dv + \int_{\partial R_t}\mathbf{t}_{(n)} da \tag{4.11}$$

$$\frac{d}{dt}\int_{R_t}\rho \mathbf{x}\times\mathbf{v} dv = \int_{R_t}\rho \mathbf{x}\times\mathbf{b} dv + \int_{\partial R_t}\mathbf{x}\times\mathbf{t}_{(n)} da \tag{4.12}$$

$$\frac{d}{dt}\int_{R_t}\rho\left(\frac{1}{2}\mathbf{v}\cdot\mathbf{v}+\varepsilon\right)dv = \int_{R_t}\rho\left(\mathbf{b}\cdot\mathbf{v}+r\right)dv + \int_{\partial R_t}\left(\mathbf{t}_{(n)}\cdot\mathbf{v}+h_{(n)}\right)da \tag{4.13}$$

Where equations (4.10), (4.11), (4.12) and (4.13) represent, respectively, the balance of mass, the balance of linear momentum, the balance of angular momentum and the balance of energy.

The above laws can conveniently be written in the general form

$$\frac{d}{dt}\int_{R_t}\rho\pi dv = \int_{R_t}\rho s dv + \int_{\partial R_t} f_{(n)} da \tag{4.14}$$

With the quantities π, s and $f_{(n)}$ are given in the table for the corresponding balance laws

Table 4-1: Variables for inclusion in the general form of the balance law to give the corresponding balance law

Balance Law	π	s	$f_{(n)}$
Mass	1	0	0
Linear Momentum	$\boldsymbol{v}$	$\boldsymbol{b}$	$\boldsymbol{t}_{(n)}$
Angular Momentum	$\boldsymbol{x}\times\boldsymbol{v}$	$\boldsymbol{x}\times\boldsymbol{b}$	$\boldsymbol{x}\times\boldsymbol{t}_{(\boldsymbol{n})}$
Energy	$\varepsilon+\frac{1}{2}\boldsymbol{v}\cdot\boldsymbol{v}$	$\boldsymbol{b}\cdot\boldsymbol{v}+r$	$\boldsymbol{t}_{(n)}\cdot\boldsymbol{v}+h_{(n)}$

If the singular surface, shown in Figure 4-6 as Λ in the body R_t, is now considered it is observed that the continuum becomes discontinuous with the body being split into two separate regions R_t^+ and R_t^-, where R_t^+ is the part of the body ahead of the advancing singular surface and R_t^- is the region of the body trailing it.

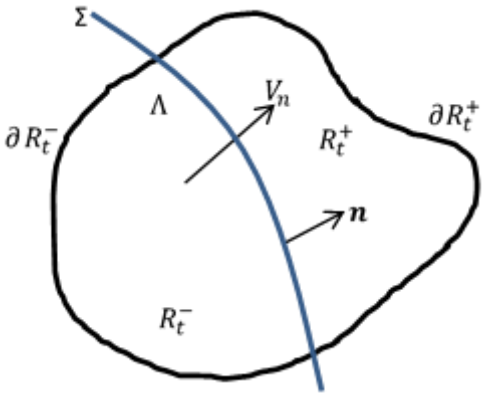

Figure 4-6: Diagram of body $\mathcal{B}$ in which the volume R_t is enclosed by surface dR_t, intersected by the singular surface Σ, where Λ is the element of Σ contained in the boundary. The superscript + and - indicate values in the region ahead of and trailing the singular surface respectively.

The balance laws are extended to discontinuity relations. The derivation of the discontinuity relations starts from Reynolds transport theorem in the following form (Chadwick, 1999):

$$\frac{d}{dt}\int_{R_t}\phi dv = \int_{R_t}\frac{\partial\phi}{\partial t}dv + \int_{\partial R_t}\phi\mathbf{v}\cdot\mathbf{n}da \tag{4.15}$$

Or in vector form as:

$$\frac{d}{dt}\int_{R_t}\mathbf{u}dv = \int_{R_t}\frac{\partial\mathbf{u}}{\partial t}dt + \int_{\partial R_t}\mathbf{u}\left(\mathbf{v}\cdot\mathbf{n}\right)da \tag{4.16}$$

Application of the scalar theorem over N^+ and N^- , where $N^{\pm} = R_t^{\pm} \cup \Lambda$ individually gives:

$$\frac{d}{dt}\int_{N^+}\phi dv = \int_{N^+}\frac{\partial\phi}{\partial t}dv + \int_{\partial R_t^+}\phi\mathbf{v}\cdot\mathbf{n}da - \int_{\Lambda}\phi^+V_n da \tag{4.17}$$

$$\frac{d}{dt}\int_{N^-}\phi dv = \int_{N^-}\frac{\partial\phi}{\partial t}dv + \int_{\partial R_t^-}\phi\mathbf{v}\cdot\mathbf{n}da - \int_{\Lambda}\phi^-V_n da \tag{4.18}$$

Adding equations (4.17) and (4.18) results in the generalisation of equation (4.15) , as:

$$\frac{d}{dt}\int_{R_t}\phi dv=\int_{R_t}\frac{\partial\phi}{\partial t}dv+\int_{\partial R_t}\phi\mathbf{v}\cdot\mathbf{n}da-\int_{\Lambda}[\phi]V_n da \tag{4.19}$$

The brackets around the field ϕ , i.e. $[\phi]$, represent the jump in the variable across the discontinuity, with the jump given as:

$$[\phi]\equiv\phi^{+}-\phi^{-} \tag{4.20}$$

The vector transport theorem, equation (4.16), is similarly modified to produce:

$$\frac{d}{dt}\int_{R_t}\mathbf{u}dv=\int_{R_t}\frac{\partial\mathbf{u}}{\partial t}dv+\int_{\partial R_t}\mathbf{u}\left(\mathbf{v}\cdot\mathbf{u}\right)da-\int_{\Lambda}[\mathbf{u}]V_n da \tag{4.21}$$

Application of the modified scalar and vector transport theorems to the general form of the balance equations results:

$$\int_{R_t}\left(\frac{\partial}{\partial t}(\rho\pi)-\rho s\right)dv+\int_{\partial R_t}\left(\rho\pi\mathbf{v}\cdot\mathbf{n}-f_{(n)}\right)da-\int_{\Lambda}[\rho\pi]V_n da=0 \tag{4.22}$$

Where the values of π, s and $f_{(n)}$ are taken as the quantities in Table 4-1 for the corresponding balance law. The volume of R_t is made to approach zero in such a way that, in the limit, ∂R_t collapses onto the two sides of Λ.

When ρ,π and s are assumed to retain away from Σ the smoothness properties attributed to them previously the result of this procedure is:

$$\int_{\Lambda}\left(\left[\rho\pi\mathbf{v}\cdot\mathbf{n}-f_{(n)}\right]-[\rho\pi]V_n\right)da=0 \tag{4.23}$$

This holds for all segments of the singular surface that are formed by intersection of the surface with regular regions of the body. Therefore, providing the integrand is continuous on Σ, the general jump condition is given:

$$\left[\rho V\pi+f_{(n)}\right]=0 \tag{4.24}$$

Where V is the local speed of propagation of the surface relative to the material, and is given mathematically as:

$$V = V_n - \mathbf{v} \cdot \mathbf{n} \tag{4.25}$$

The general jump condition, equation (4.24), results in the basic jump conditions when the entries in Table 4-1 are substituted in, in place of π and $f_{(n)}$.

$$\left[\rho V\right] = 0 \tag{4.26}$$

$$\left[\rho V \mathbf{v} + \mathbf{t}_{(n)}\right] = \mathbf{0} \tag{4.27}$$

$$\left[\rho V \left(\varepsilon + \tfrac{1}{2}\mathbf{v} \cdot \mathbf{v}\right) + \mathbf{t}_{(n)} \cdot \mathbf{v} + h_{(n)}\right] = 0 \tag{4.28}$$

4.5 Thermodynamic consideration of shocks

The thermodynamic aspect of modelling shocks in a continuum mechanical framework dates back to the early 20th century. The foundations for the modern analysis of discontinuous surfaces were laid in by Hadamard (Hadamard, 1903) in his work 'Lecons sur la propagation des ondes et les equations de l'hydrodynamique' in 1903. His studies focussed on the basic jump relations for field quantities and their derivatives.

Further work was done in 1948 by Courant and Friedrich (Courant & Friedrichs, 1948). This work is of great value to considering shocks and is the beginning of the more modern approach to discontinuity analysis. The work considers shocks in the context of gas dynamics, not the solid mechanics of interest to this work, but it provides a useful analysis of moving strong discontinuity surfaces. The conclusion of the work by Courant and Friedrich showed that the entropy change across shocks can be disregarded in all but the strongest shocks in gases. Further work by Wallace (Wallace, 1980) shown that entropy effects are of third order in strain in gases, but second order in strain for weak shock in solids.

Following on from the work of Courants and Friedrich (Courant & Friedrichs, 1948) the assumption that a shock wave can be approximated using a smooth wave has found much use, first for quasistatic deformation (Drugan, 1986) and then of dynamic deformation of elastic plastic solids (Drugan & Shen, 1987) (Drugan & Shen, 1990). This assumption has been proven to be valid by Brannon et al. (Brannon & Drugan, 1995) in 1995. Using this assumption, the works of Drugan and Shen in the 1980's have provided specific conditions which are required for jump to occur. The key stage of these works was the realisation that integration of the maximum plastic work inequality at a material point during the passage of a discontinuous surface provides an explicit restriction on jumps in the components of stress and strain (Drugan & Shen, 1987).

The conclusion of Courants and Friedrich's 1948 (Courant & Friedrichs, 1948) work stating that the entropy changes across shocks can be disregarded in all but the strongest of shocks, which has led to the assumption that entropy changes across shocks must be small in order for the approximation by a smooth wave to hold is challenged by Brannon et al. (Brannon & Drugan, 1995). The work by Brannon et al. aimed to extend the work of Courant and Friedrich from entropy effects in weak one-dimensional shocks in mechanically conservative systems to general three-dimensional large deformations in a material of arbitrary construction (Brannon & Drugan, 1995). This extension concludes that the approximation of a shock by a smooth wave is legitimate, and also that entropy change across the wave does not need to be small in order for the approximation to hold. The entropy change can be significant at the first order, and the change in entropy predicted using the smooth wave approximation will agree until the third order (Brannon & Drugan, 1995).

4.6 Hugoniot

When modelling shocks, one of the important functions is the so called Hugoniot. The Hugoniot function is a function which essentially relates the state of the continuum on one side of the shock to the state of the material on the other side of the shock.

Specifically, the Hugoniot provides the set of all states on one side of the shock front associated with a given state, referred to here as state 1, on the other side, that is compatible with the jump in internal energy (Brannon & Drugan, 1995). It is convenient here to define the Hugoniot mathematically as:

$$H\left(u,\mathbf{t},\mathbf{F},\mathbf{Q}\right)\equiv\left(u-u_1\right)-\frac{1}{2\rho_0}\left(\mathbf{t}^T+\mathbf{t}_1^T\right):\left(\mathbf{F}-\mathbf{F}_1\right)-\frac{\mathbf{N}\cdot\left(\mathbf{Q}-\mathbf{Q}_1\right)}{\rho_0 c_0} \tag{4.29}$$

The function H is convenient in this form as it is defined entirely in terms of thermodynamical variables (Brannon & Drugan, 1995). This form of the Hugoniot can be written by considering the first law of thermodynamics in jump form. This can be given as (Brannon & Drugan, 1995):

$$\left[u\right]=\left[w_s\right]+\left[w_T\right] \tag{4.30}$$

Where

$$\left[w_s\right]=\frac{1}{\rho_0}\mathbf{t}_A^T:\left[\mathbf{F}\right] \tag{4.31}$$

$$\left[w_T\right]=\frac{\mathbf{N}\cdot\left[\mathbf{Q}\right]}{\rho_0 c_0} \tag{4.32}$$

Which by substitution of equations (4.32) and (4.31) into (4.30), results in

$$\left[u\right]=\frac{1}{\rho_0}\mathbf{t}_A^T:\left[\mathbf{F}\right]+\frac{\mathbf{N}\cdot\left[\mathbf{Q}\right]}{\rho_0 c_0} \tag{4.33}$$

It can be seen that by rearrangement of equation (4.33) to set it to equal zero, and expansion of the jump terms following the definition in equation (4.20), then the Hugoniot function in terms of thermodynamical variables is fully derived.

A state is considered to be on the Hugoniot if the function results in $H=0$. Solutions that satisfy this, and are therefore on the Hugoniot, provide all of the equilibrium states achievable by the material after shock wave passage.

4.7 Summary

The basic definition of shock waves has been describes, along with the conditions which are required for shocks to form in solid (i.e. uniaxial strain). The continuum jump conditions have been outlined, these conditions ensure the balance principles of continuum mechanics are maintained when considering a shock to be a travelling discontinuity. Finally the important Hugoniot function has been discussed.

5 Dislocation dynamics

This section outlines the theoretical aspects of this work, starting from the cubic structures of interest, the key features of these structures, defects contained within crystals, focussing specifically on the role of dislocations. The key properties of dislocations are then discussed, along with forces acting upon them. The microscale dislocation processed presented in this chapter form the underlying physical processes of the material model presented in detail in chapter 6.

5.1 Crystal structures of metals

When observed on an atomistic scale, the arrangement of atoms in a metallic structure is found to be very ordered. This structure is referred to as the crystal structure of the metal and has been shown to have a limited number of possible arrangements. In total there are 14 possible structures, however only three of these are commonly observed; the so-called body centred cubic structure (bcc), the face centred cubic structure (fcc) and the hexagonal close packed structure (hcp). This work focusses on modelling of metals with fcc or bcc structures, therefore only details of these structures are given here.

5.1.1 The face centred cubic structure

The face-centred cubic structure, from herein referred to simply as fcc, consists of cubic lattice, with a lattice point on each of the corners, and one additional atom located at the centre of each of the six faces of the resulting cube.

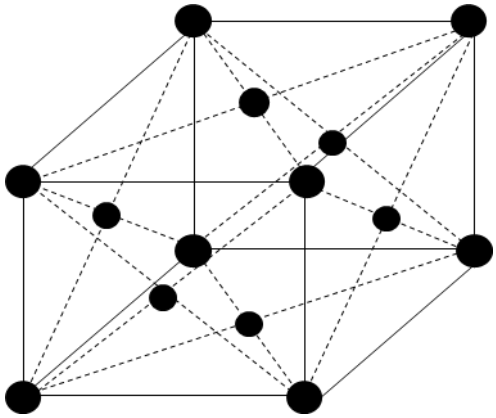

Figure 5-1: Schematic diagram of the face centred cubic structure

The fcc structure is shown in Figure 5-1. Common metals with a fcc structure include aluminium, copper, nickel, lead, gold and silver.

5.1.2 The body centred cubic structure

The body centred cubic structure, herein referred to simply as bcc, is similar to fcc in that the cubic lattice contains lattice points on the corners of the cube, however instead of having an additional six sites at the centre of each cubic face, bcc crystals contain only one additional lattice site located in the centre of the body of the cube. Figure 5-2 shows the bcc structure.

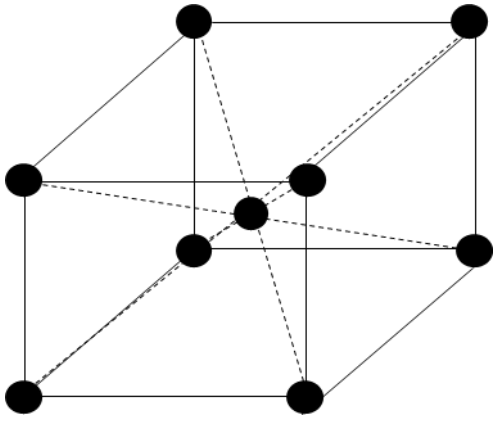

Figure 5-2: Schematic diagram of the body centred cubic structure

Metals with a bcc structure include iron, tantalum, tungsten and chromium.

5.1.3 Miller Indices

When discussing metals on the microscale, it is convenient to use the conventional notation of Miller indices. Miller indices are used to describe planes contained in the crystal, as well as directions through the crystal. For cubic structures the indices are determined simply by attaching axes aligned with the edges of the cube and then applying the following three stage approach:

i) Determine the intercepts the crystal plane makes with the attached crystal axes expressing these as the number of axial lengths.
ii) Take the reciprocal of the intercepts
iii) Scale to the smallest integers for which the same ratios are maintained.

When defining a direction through the crystal, the Miller indices are determined by constructing an arrow pointing in the required direction, ensuring it passes through the origin and then determining the axial intercepts. Steps two and three from above can then be applied, leading to the required values.

When expressing Miller indices there are a few common conventions whih are adopted in this report. Firstly, when expressing negative Miller indices, the value is written with an over bar instead of a minus sign, e.g. (-101) would be written as $(\bar{1}01)$. Next, the shape of the brackets enclosing the indices indicate whether the indices are defining a plane or a direction. Planar indices are expressed in round brackets, e.g. (111), and directional indices are expressed in square brackets, e.g. $[110]$. Sets of equivalent planes are denoted by curly brackets, e.g. $\{111\}$ and sets of equivalent directions by pointed brackets, e.g. $\langle 110 \rangle$.

5.2 Defects in metals

So far, the crystal structures outlined show “perfect” crystal; that is, crystals that are free from any defects. Theoretical analysis of the shear strength of perfect crystal provides a result that is orders of magnitude greater than the equivalent experimentally obtained values, indicating that the mechanisms carrying deformation are not accounted for in the treatment of perfect crystals. It is well

established that defects are nearly always present in a crystal, the presence of which can explain the discrepancy in shear strengths.

There are several types of defects that can be present in crystals; point defects, line defects, planar defects and volume defects. The main focus of this work is looking at line defects, in the form of dislocations, however, as is seen later, other forms of defects can affect dislocations, therefore it is necessary to briefly introduce them here.

5.2.1 Point defects

Point defects are defects in the crystal that are local to a single point in the crystal. These can be in the form of a vacancy, which is a lattice point with a missing atom, as is shown by Figure 5-3(a); an interstitial atom, where an atom is located in a site outside of regular lattice sites, as is shown by Figure 5-3(b), or an impurity atom, where an atom of a different species is found in the lattice. Impurity atoms can occupy either a regular lattice point, or an interstitial location.

(a) (b)

Figure 5-3: Schematic diagrams showing (a) a lattice vacancy and (b) an interstitial

5.2.2 Dislocations

The most important defect considered in this work is the line defect in the form of a dislocation. Dislocations have two fundamental forms described as either edge or screw dislocations. Edge dislocations are observed as an extra half plane of atoms present in part of the crystal, as is shown in Figure 5-4.

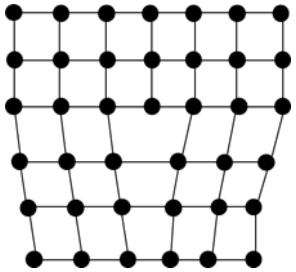

Figure 5-4: Schematic diagram showing an edge dislocation, The edge dislocation is formed by an extra half layer of atoms being inserted into part of an otherwise perfect crystal.

Screw dislocations can be thought of as a perfect crystal which has a cut made into its body and then the crystal being twisted resulting in one side of the lattice being skewed by one lattice site. Figure 5-5 shows this diagrammatically.

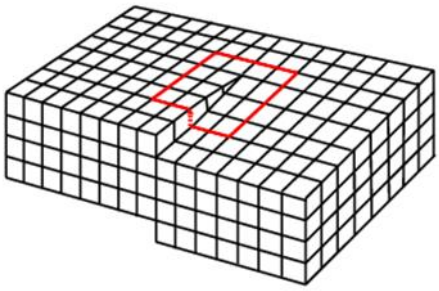

Figure 5-5: Schematic diagram of a screw dislocation

Dislocations are of significant interest to this work as they are able to propagate through the crystal resulting in the relative displacement of two parts of the crystal. The result of this is observed to be equivalent to an entire plane of atoms sliding over another.

5.3 Burgers vector

One of the most important quantities in the description if dislocations is the Burgers vector. The Burgers vector is determined by the crystal displacement caused by the presence of a dislocation in an otherwise perfect piece of crystal. A simple way of determining the Burgers vector is done by forming a loop around a dislocation in the material and determining the distortion caused by the dislocation. This is illustrated for the case of an edge dislocation in Figure 5-6.

Using the edge dislocation shown in Figure 5-6 the Burgers vector is obtained by forming a loop clockwise around the dislocation, starting at point S, and ensuring the same number of lattice sites are visited in each direction. This leads to an un-closed loop. In order to close the loop, the vector $\boldsymbol{b}$ is added, shown by the red arrow in Figure 5-6. This vector is the Burgers vector. It is noted that the convention used here determines the Burgers vector using a clockwise loop, if however, an anticlockwise loop is used, the Burgers vector obtained will be of identical magnitude, with opposite direction.

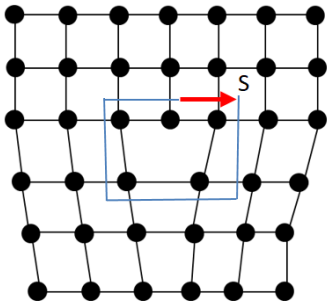

Figure 5-6: Schematic diagram showing the construction of a clockwise loop around an edge dislocation, with the resulting Burgers vector, represented by the red arrow, required to close the loop.

In the case of a screw dislocation, the same approach is applied as was used to determine the Burgers vector of an edge dislocation. The screw dislocation shown in Figure 5-5 shows a clockwise loop constructed around the screw dislocation.

It is seen that, like the edge dislocation, the loop is unclosed if the same number of lattice sites are visited in each direction, with the vector $\boldsymbol{b}$ required to close the loop. As with the edge dislocation, the vector $\boldsymbol{b}$ is the Burgers vector. Consistent with the edge analysis, an anticlockwise loop constructed around a screw dislocation will result in the Burgers vector having equal magnitude but opposite direction to that obtained with the clockwise loop.

One key difference between the Burgers vectors of screw and edge dislocations is apparent when considering their direction with respect to the dislocation line vector. The dislocation line vector of an edge dislocation, is perpendicular to the

Burgers vector, and in contrast to this, the dislocation line vector and Burgers vector for screw dislocations are parallel to each other. This property is important when defining the dislocation glide planes.

It is seen in Figure 5-5 and Figure 5-6 that the size of the Burgers vector is half an atomic spacing, i.e. it is closing the loop of an extra half layer of atoms. Using the conventional notation, the magnitude of a Burgers vector can therefore be found as:

$$|b| = \frac{a_0}{2}\left|\langle hkl \rangle\right| \tag{2.1}$$

Where a_0 is the lattice constant; i.e. the spacing between two lattice points in a perfect piece of crystal, and $\langle hkl \rangle$ are the directional Miller indices of the vector. Therefore, the magnitude of Burgers vector is dependent on the structure of the crystal. For an fcc crystal, the magnitude is found to be:

$$|b| = \frac{a_0}{2}\left|\langle 110 \rangle\right| = \frac{\sqrt{2}a_0}{2} \tag{2.2}$$

Similarly, in bcc metals the magnitude of Burgers vector is found as:

$$|b| = \frac{a_0}{2}\left|\langle 111 \rangle\right| = \frac{\sqrt{3}a_0}{2} \tag{2.3}$$

5.4 Slip and slip planes

It is observed that, when a metal is loaded and deforms plastically, small step like ridges are formed on the surface, as is shown in Figure 5-7.

Figure 5-7: Diagram showing 1) an un-loaded, un-deformed specimen and 2) the same specimen after loading has been applied and plastic deformation has occurred. The direction of loading is indicated by the arrow (Anon., 2013).

The formation of these steps indicate that the plastic deformation of the crystal occurs on specific planes and in specific directions in the crystal. This is explained by dislocation slip.

Slip occurs when the material is loaded sufficiently to cause dislocations to move from their current locations and to propagate through the crystal. The motion of dislocations results in a portion of the crystal displacing relative to the remaining part, as is shown in Figure 5-7. The motion of screw and edge dislocations differs. An edge dislocation, under an applied load, glides in the direction of its Burgers vector. The process of edge dislocation glide is shown in Figure 5-8. It is apparent from Figure 5-8 that the formation of surface steps from an edge dislocation is the result of the dislocation moving one lattice site at a time through the crystal, and not an instantaneous shearing of several lattice sites. The surface discontinuity shown in Figure 5-8 is for a single edge dislocation; in a physical sample many dislocations are likely to follow this process, thereby exaggerating the surface effect.

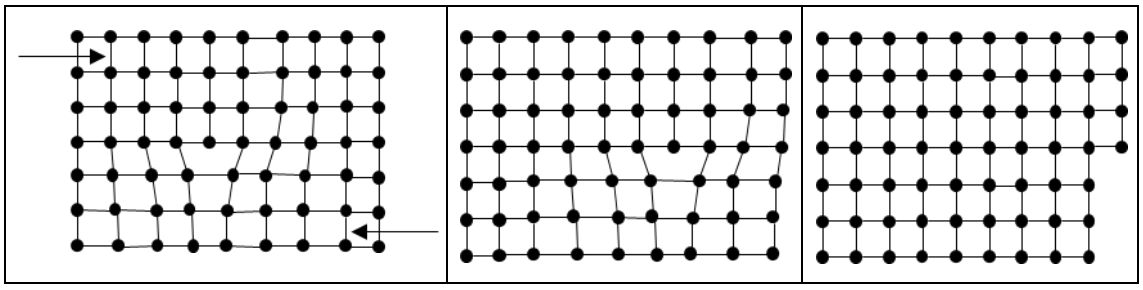

Figure 5-8: Schematic diagram of an edge dislocation moving to the edge of the crystal under an applied shear load. The three diagrams show the initial dislocation (left), the step formed on the edge of the crystal (right) and the

dislocation during propagation (centre). The shear loading is indicated by arrows on the left hand diagram.

The propagation of a screw dislocation is depicted in Figure 5-9, where it is seen that, similar to the edge dislocation, the formation of the step on the surface occurs as the dislocation moves one lattice site at a time. There is however one notable difference; the motion of the screw dislocation is perpendicular to the direction of its Burgers vector, which results in the direction of motion of screw dislocations being perpendicular to the direction of slip. This is highlighted in Figure 5-9, where the rotation axis is used to form a clockwise loop around the travelling dislocation in the crystal. To vector required to close the loop, i.e. the Burgers vector, is seen the be directed along rotation axis, however the motion of the screw dislocation can clearly be seen to be travelling perpendicular to the axis.

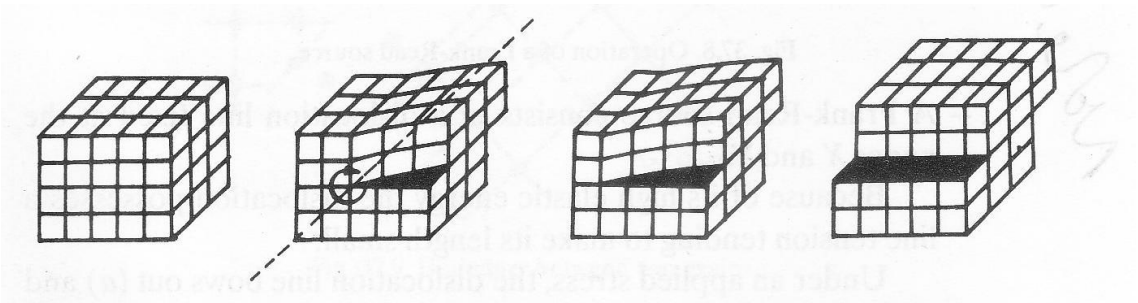

Figure 5-9: Diagram showing the propagation of a screw dislocation under an applied shear stress (Anon., 2012)

The process of dislocation slip is referred to as conservative motion of dislocations, as the number of lattice sites on the slip plane is conserved throughout.

5.4.1 Slip planes

Within a crystal there are various planes. Slip does not occur on all planes in the crystal; certain planes are much more susceptible to slip than others. These are referred to as the slip planes and are commonly the planes of greatest interplanar spacing. The planes with the greatest inter-planar spacing are also the planes of

closest packing. Due to these properties being structure dependent, the slip planes are dependent on the crystal structure of the metal being examined.

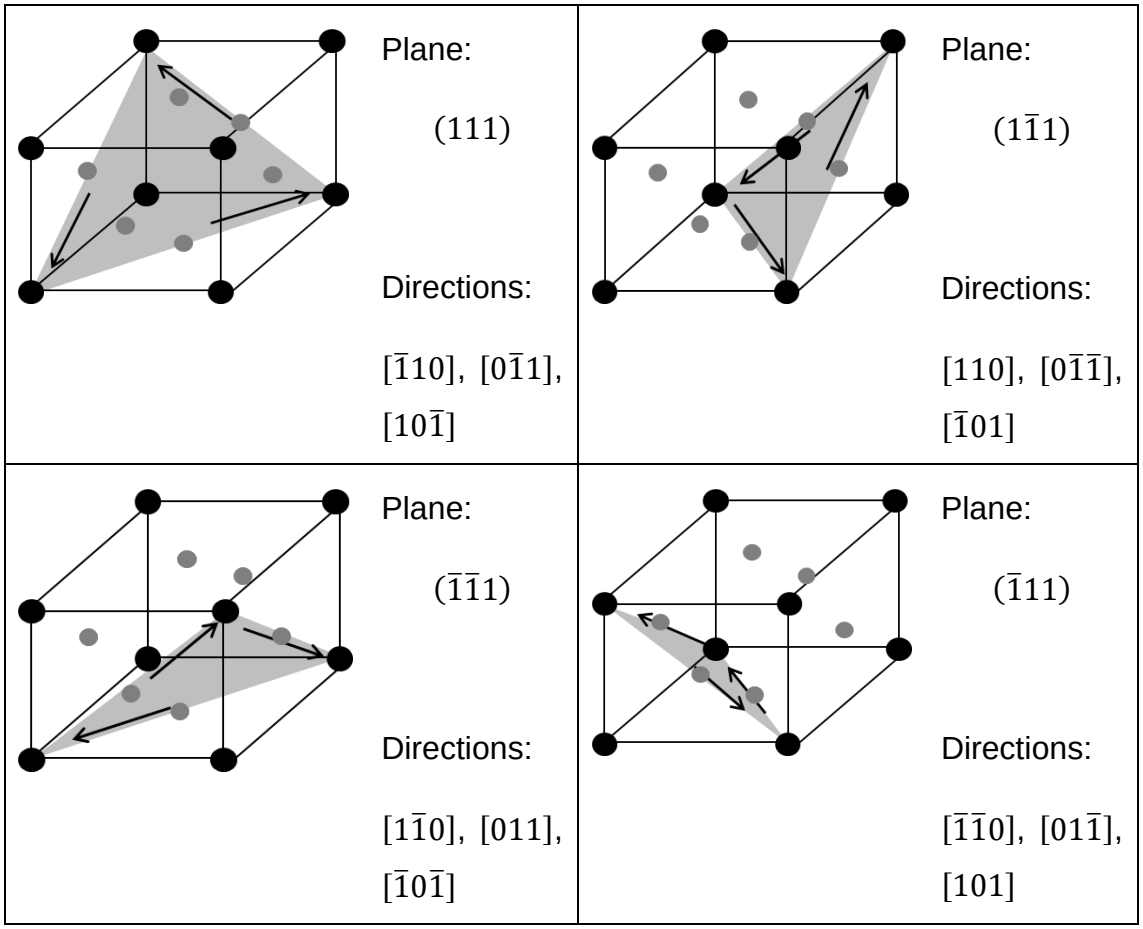

Figure 5-10: Schematic diagrams showing the slip systems in fcc crystals. The four {111} planes are shown with the arrows indicating the three <110> directions of each plane.

Along with the slip planes, the direction of slip is also defined. This is done by taking the possible directions of the slip planes. The combination of the slip plane and the slip direction are then referred to as the slip system.

The slip systems for fcc metals are shown in Figure 5-10. The planes of closest packing, and therefore the slip planes, are the $\{111\}$ planes, of which there are four. The directions of these planes are the $\langle 110 \rangle$ directions, and it is seen that

each plane has three of these directions. Therefore, an fcc metal has a total of 12 slip systems.

The slip systems in bcc metals consist of the $\{110\}$ planes and the $\langle 111 \rangle$ directions. There are six $\{110\}$ planes, each with two $\langle 111 \rangle$ directions, giving twelve slip systems. These are shown in Figure 5-11 and are common to all bcc metals. Additional to these twelve, some bcc metals have additional slip systems. These are the $\{112\}$ planes, of which there are twelve, and the $\{123\}$ planes, of which there are twenty-four. Each of these planes have only one $\langle 111 \rangle$ direction, giving an additional thirty-six slip planes, which, when combined with the original twelve, results in a possible forty-eight slip systems.

5.5 Climb

Additional to slip, non-conservative motion of dislocations is also possible under certain conditions. Non-conservative motion of dislocations is denoted as such, due to the number of lattice sites on the slip plane not being conserved during the dislocation motion. This can occur when the dislocation moves perpendicular to the slip plane, and effectively climbs out of it. The process of climb can enable a dislocation to overcome a point obstacle, which would otherwise inhibit its motion. If only a part of the dislocation line experiences climb, a jog is formed, whereby the dislocation has segments over two (or more) slip planes, while still being connected to one another.

5.6 Mixed dislocation

From the definition of a dislocation, the dislocation line can be thought of as a boundary between an area over which slip displacement has occurred and an un-slipped region of the crystal (Hirth & Lothe, 1982). Using this concept, it is apparent that the dislocation line cannot terminate in the body of the crystal; it must terminate at a grain boundary, free surface or an interaction with another dislocation or defect, form a closed dislocation loop.

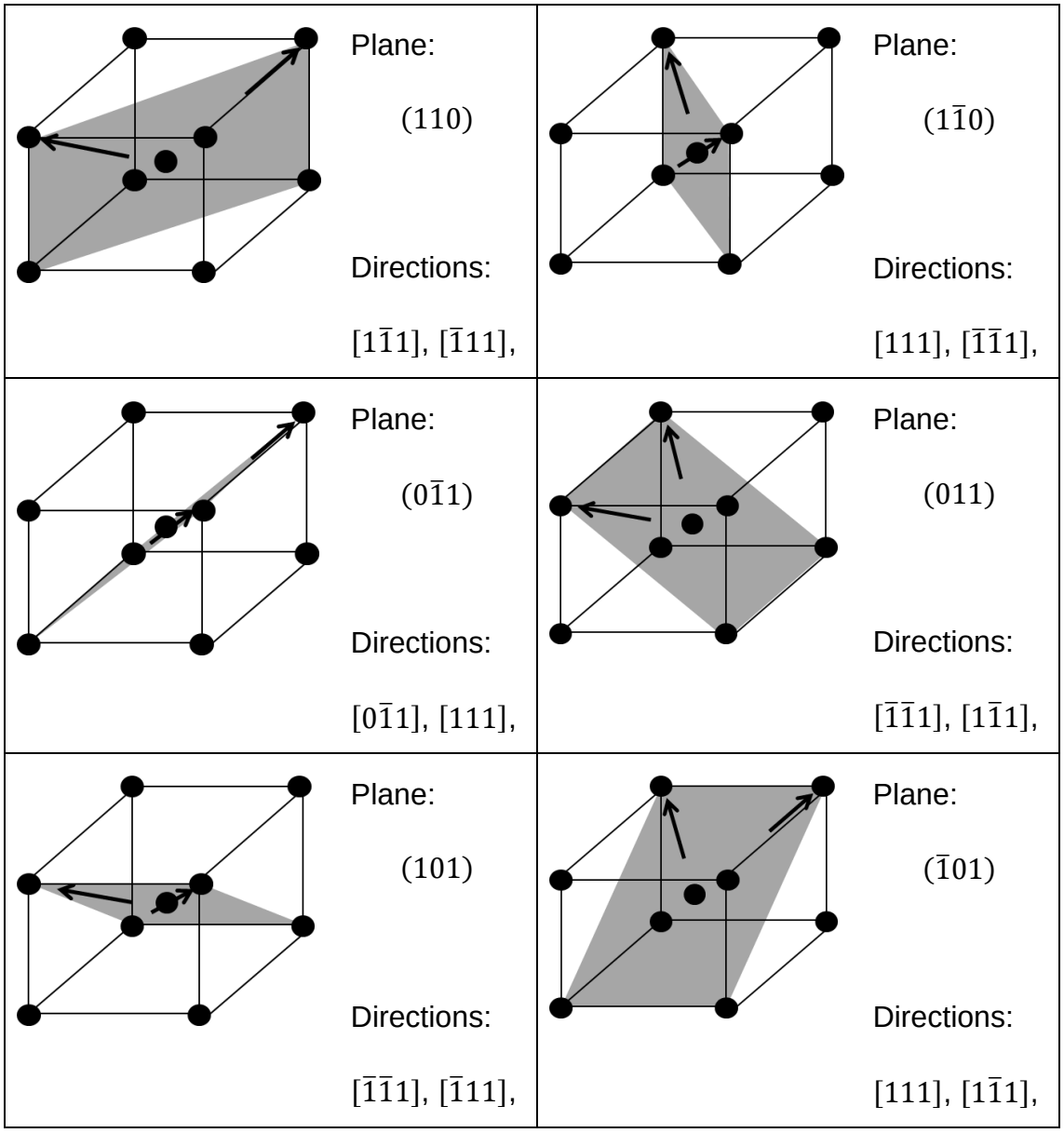

Figure 5-11: Schematic diagrams showing the 12 common slip systems in BCC crystals. The six {110} planes are shown with the arrows indicating the two <111> directions of each plane.

When a dislocation is curved, as is the case in a dislocation loop, it is no longer applicable to determine the dislocation to be either an edge dislocation or a screw dislocation. The dislocation line shown in Figure 5-12 can be seen, at point A to be purely a screw dislocation, but at point C purely an edge dislocation, and at point B a mixture of both screw and edge. Such a dislocation is referred to as a mixed dislocation.

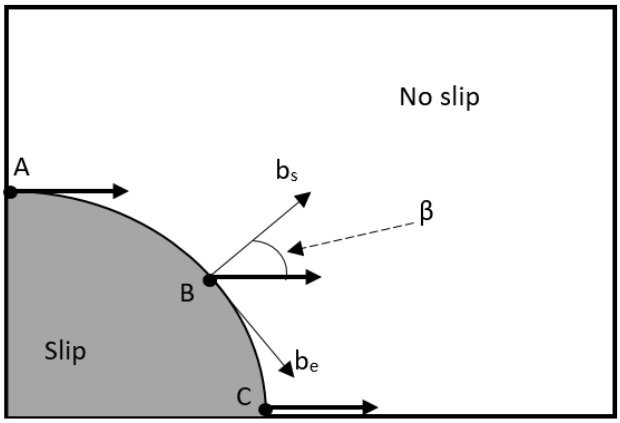

Figure 5-12: Diagram showing a segment of a dislocation loop bounding a region where slip has occurred in the crystal. The direction of the Burgers vector is shown at points A, B and C.

The total Burgers vector of the dislocation loop is the same at all points and can be resolved into screw and edge components:

$$b_s = b\cos\beta \tag{2.4}$$

$$b_e = b\sin\beta \tag{2.5}$$

Where b_e is the edge component of the total Burgers vector, b_s is the screw component of the total Burgers vector and β is the angle between the total Burgers vector and the screw component of the Burgers vector.

5.7 Strain energy of screw dislocation

It is seen that, the presence of the screw dislocation shown in Figure 5-13 induces a displacement around the z-axis. It is reasonable to assume that the induced deformation increases uniformly with angle θ (Hirth & Lothe, 1982), allowing the following relation to be written:

$$u_z(r,\theta) = \frac{b\theta}{2\pi} \tag{2.6}$$

Where u_z is the displacement around the z-axis.

The stress associated with this displacement is given from elasticity theory to be:

$$\sigma_{\theta z} = \frac{Gb}{2\pi r} \tag{5.7}$$

$$\sigma_{rz} = \sigma_{r\theta} = \sigma_{rr} = \sigma_{\theta\theta} = \sigma_{zz} = 0 \tag{5.8}$$

Where $\sigma_{\theta z}$ is the stress associated with the displacement and G is the shear modulus.

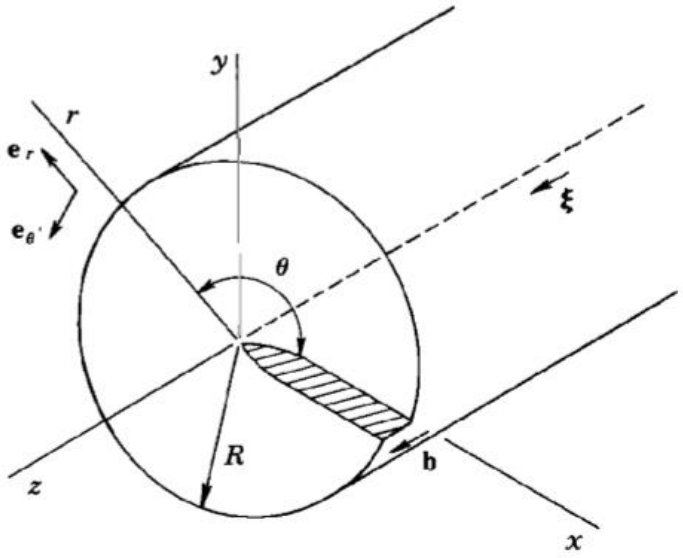

Figure 5-13: A screw dislocation in a cylinder showing the displacement caused along the z-axis by the presence of the dislocation (Hirth & Lothe, 1982)

As a result of the crystal displacements caused by the presence of a screw dislocation, an elastic strain field is present surrounding the dislocation, which has an associated energy.

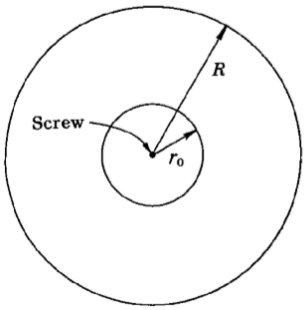

Figure 5-14: Schematic diagram of a screw dislocation in a cylinder showing the relative distances R and r_0 (Hirth & Lothe, 1982).

Considering the field surrounding the dislocation in Figure 5-14 the energy stored per unit length can be expressed:

$$\frac{W}{L} = \int_{r_0}^{R} \frac{\sigma_{\theta z}^2}{2G} 2\pi r \, dr \tag{5.9}$$

Where W/L is the energy stored per unit length of the dislocation.

Substitution of the stress component, equation (5.7), into equation (5.9) and integrating results:

$$\frac{W}{L} = \frac{Gb^2}{4\pi} \ln \frac{R}{r_0} \tag{5.10}$$

From equation (5.10) it is apparent that the stored energy, W/L, diverges as $R \to \infty$ or $r_0 \to 0$, which means that the energy stored is dependent on the crystal size and therefore it is impossible to determine a characteristic value. Approximations for the value of R can be made. When considering a single dislocation in a sample of the crystal, approximating $R \approx l$, where l is the shortest distance between the dislocation and the nearest free surface is a good choice (Hirth & Lothe, 1982). In the case a many dislocations, a good choice of the value of R is found to be half the average distance between dislocations (Hirth & Lothe, 1982).

The divergence of r_0 limits this analysis to hold only for regions at greater radius than $r_0 \approx b$. Therefore, equation (5.10) can be re-written as:

$$\frac{W}{L} = \frac{Gb^2}{4\pi} \ln \frac{\alpha R}{b} \tag{5.11}$$

Where α is equal to one.

5.8 Force on a screw dislocation

Generally, a force is defined relative to a general configurational coordinate η by the requirement that the change in total energy is equal to the force multiplied by the displacement, which can be expressed mathematically as:

$$\delta W_t = -F_\eta \delta\eta \tag{5.12}$$

Where, W_t is the total energy, F_η is the force relative to the coordinate η.

Thermodynamically, the forces acting on a dislocation are defined as (Hirth & Lothe, 1982): "*Forces on dislocations are virtual forces representing the change in free energy of the system with displacement of the dislocation* (Hirth & Lothe, 1982)*"*.

The total energy, W_t, can be decomposed into the elastic energy, W_e, and the potential energy of mechanisms exerting external force on the dislocation, W_p , as:

$$W_t = W_e + W_p \tag{5.13}$$

It has been seen that the total energy depends on the position of the dislocation, therefore the force is also dependent on the position of the dislocation.

Considering the dislocation shown in Figure 5-13, and making the assumption that it is parallel to the free surface, at a distance l from it, the energy is given, using equation(5.10) to be:

$$\frac{W}{L} = \frac{Gb^2}{4\pi} \ln \frac{\alpha l}{b} \tag{5.14}$$

Therefore, applying equation (5.12), the force per unit length tending to move the dislocation towards the surface is calculated to be:

$$\frac{F}{L} = -\frac{\partial(W/L)}{\partial(-l)} = \frac{Gb^2}{4\pi l} \tag{5.15}$$

This force arises solely from change in elastic energy in the crystal, and is considered to be an image force.

If the dislocation is far from the boundaries of the material, image forces are negligible, and the energy is independent of the x-coordinate. Considering a dislocation under these conditions, and allowing it to move from position x_1 to position x_2, the surfaces above and below the dislocation are displaced by $\boldsymbol{b}$, relative to one another over an area $L(x_2 - x_1)$. If this displacement is caused by a uniformly applied shear stress, in moving the dislocation the shear stress does work, $\sigma_{yz}L(x_2 - x_1)b$. This work done is at the expense of the potential energy of external mechanisms acting on the dislocation, and is expressed:

$$\Delta W_p = \sigma_{yz} L(x_2 - x_1) b \tag{2.16}$$

Substitution of this into equation (5.15) provides the force per unit length as:

$$\frac{F_x}{L} = \sigma_{yz} b \tag{2.17}$$

In the region of the dislocation core (the region of severe dislocation immediately surrounding the dislocation), the total stress, σ_t, can be expressed as a sum of the dislocation self-stress, σ_d, and the stress caused by image effects, external loads, and other stress sources, σ, in the form:

$$\sigma_t = \sigma_d + \sigma \tag{5.18}$$

The self-stress of the dislocation does no work during motion of the screw dislocation, therefore the change in energy per unit length is given:

$$\frac{\delta W}{L} = \delta x \int_{-\infty}^{\infty} \sigma_{yz_d} \frac{\partial}{\partial x} \Delta u dx = 0 \tag{5.19}$$

Whereas, the external stress field, σ_{yz}, does do work, which is given:

$$\frac{\delta W}{L} = \delta x \sigma_{yz} \int_{-\infty}^{\infty} \frac{\partial}{\partial x} \Delta u dx = \delta x \sigma_{yz} b \tag{5.20}$$

which is at the expense of the total energy of the system, therefore:

$$\frac{\delta W_t}{L} = -\delta x \sigma_{yz} b \tag{5.21}$$

From this the total force per unit length acting on the dislocation core is calculated to be:

$$\frac{F_x}{L} = \sigma_{yz} b \tag{5.22}$$

Or for motion in the y-direction:

$$\frac{F_y}{L} = -\sigma_{xz} b \tag{5.23}$$

Comparing equations (5.19) and (5.20) is apparent that the self-stress does not impose any force of the screw dislocation.

5.9 Edge Dislocations

Similar to the analysis of screw dislocations, edge dislocations will now be discussed in terms of the stresses, strain energy, and forces acting on them.

Analysis of the edge dislocation in a cylinder allows for the stress components to be obtained with the aid of the stress function ψ_e

$$\psi_e = -\frac{Gby}{4\pi(1-\upsilon)} \ln\left(x^2 + y^2\right) \tag{5.24}$$

As:

$$\sigma_{xx} = -\frac{Gb}{2\pi(1-\upsilon)} \frac{y\left(3x^2 + y^2\right)}{\left(x^2 + y^2\right)^2} \tag{5.25}$$

$$\sigma_{yy} = \frac{Gb}{2\pi(1-\upsilon)} \frac{y\left(x^2 - y^2\right)}{\left(x^2 + y^2\right)^2} \tag{5.26}$$

$$\sigma_{xy} = \frac{Gb}{2\pi(1-\upsilon)} \frac{x\left(x^2 - y^2\right)}{\left(x^2 + y^2\right)^2} \tag{5.27}$$

$$\sigma_{zz} = \upsilon\left(\sigma_{xx} + \sigma_{yy}\right) = -\frac{Gb\upsilon}{\pi(1-\upsilon)} \frac{y}{x^2 + y^2} \tag{5.28}$$

$$\sigma_{xz} = \sigma_{yz} = 0 \tag{2.29}$$

Where υ is Poissons ratio.

The displacements caused by the presence of the edge dislocation in the crystal are found to be:

$$u_x = \frac{b}{2\pi}\left[-\tan^{-1}\frac{x}{y} + \frac{xy}{2(1-\upsilon)\left(x^2 + y^2\right)}\right] + C \tag{5.30}$$

Where the constant C is determined by the condition that $u_x = 0$ when $y = 0$. Applying this condition yields $C = b/4$, therefore:

$$u_x = \frac{b}{2\pi}\left[\tan^{-1}\frac{x}{y} + \frac{xy}{2(1-\upsilon)\left(x^2 + y^2\right)}\right] \tag{5.31}$$

Likewise,

$$u_y = -\frac{b}{2\pi}\left[\frac{1-2\upsilon}{4(1-\upsilon)}\ln\left(x^2 + y^2\right) + \frac{x^2 - y^2}{4(1-\upsilon)\left(x^2 + y^2\right)}\right] \tag{5.32}$$

Where the constant, $C = b/4\pi(1-\upsilon)$ is introduced to yield a symmetric expression in x and y.

5.9.1 Strain energy of an edge dislocation

The strain energy per unit length of a dislocation between two cylindrical surfaces of radius r_0 and R about an edge dislocation is given by:

$$\frac{W}{L}=\int_{r_0}^{R} r dr \int_{0}^{2\pi} d\theta \left[\frac{1}{2G}\sigma_{xy}^2+\frac{1}{2\mathrm{E}}\left(\sigma_{xx}^2+\sigma_{yy}^2-2\upsilon\sigma_{xx}\sigma_{yy}-\sigma_{zz}^2\right)\right] \tag{5.33}$$

Where E is Young's modulus.

Which integrates to yield:

$$\frac{W}{L}=\frac{Gb^2}{4\pi\left(1-\upsilon\right)}\ln\frac{R}{r_0} \tag{5.34}$$

Comparing this result to that obtained in the analysis of screw dislocations, equation (5.10), it is seen that they are the same, except for the $(1-\upsilon)$ factor. Similar to the treatment of screw dislocations, this can be expressed

$$\frac{W}{L}=\frac{Gb^2}{4\pi\left(1-\upsilon\right)}\ln\frac{R\alpha}{b} \tag{5.35}$$

5.9.2 Forces acting on an edge dislocation

In direct analogy to screw dislocations, the total stress field, σ_t, can be decomposed into self-stress, σ_d, and stress from external sources, σ. Applying the same principles as for screw dislocations, only σ does work as the dislocation moves on the glide plane, with the force per unit length produced purely by σ. In the x-direction, this force is given:

$$\frac{F_x}{L}=\sigma_{xy}b \tag{5.36}$$

If the motion of the dislocation is non-conservative, i.e. climb, both the elastic energy, W_e and the potential energy of external mechanisms acting on the dislocation, W_p, change.

The force required for climb can be derived from the derivative of the sum of strain energy and potential energy with respect to the y-position of the edge dislocation.

The process of climb involves the removal of the extra half plane of atoms from the slip plane (i.e. motion perpendicular to the slip direction), which will therefore reduce the strain energy and potential energy of external mechanisms acting on the dislocation. At the expense of these, energy flows to the dislocation core and is dissipated there (Hirth & Lothe, 1982). The expression for climb force can be developed from this. As with the glide forces, self-stress does not exert climb force.

In the presence of a compressive force acting over the region of the dislocation core, a climb force is experienced. The climb force is determined by the energy lost from the system during motion. Consider the diagram in Figure 5-15, which depicts a schematic diagram of an edge dislocation climbing a distance δy. It is seen that as the dislocation climbs, distortion to the surrounding lattice is caused, through which the energy required for climb flows If the value of h is set large enough, the compressive stress σ_{xx} will be much larger than the self stress, σ_d, rendering it negligible. Therefore, in analogy with previous, the climb force is found from the change in energy as:

$$\frac{\delta W}{L} = \frac{F_y}{L}\delta y = -\sigma_{xx} n \delta y + \frac{\sigma_{xx}^2}{2E} b \delta y \tag{5.37}$$

The last term on the left hand side of equation (5.37) is neglected as it is of the same order of magnitude as the imprecision of linear elasticity theory. Therefore, the climb force is given as:

$$\frac{F_y}{L} = -\sigma_{xx} b \tag{5.38}$$

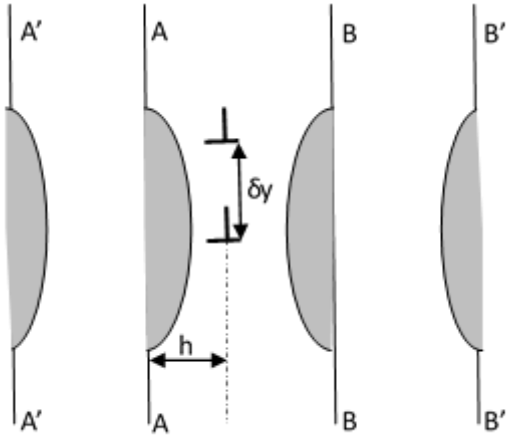

Figure 5-15: Schematic diagram showing that as the edge dislocation climbs a distance δy, energy flows into the region surrounding the dislocation through the parallel planes AA and BB.

5.10 Mixed straight dislocations

So far, the analysis has assumed the dislocations to be either pure screw or pure edge in nature. However, in general dislocations in real crystals are more likely to be of mixed nature, containing both screw and edge components. This section considers the forces acting on straight mixed dislocations.

The glide plane of a straight mixed dislocation is defined by the edge component only. This is due to the fact that the glide plane is defined as the plane containing both the dislocation line and the Burgers vector, which for screw dislocations are parallel, and therefore there are no defined slip planes for screw dislocations.

To determine the forces acting on a straight mixed dislocation, it is first necessary to consider the energy stored per unit length of dislocation. This is achieved by superposition of the screw and edge components of stored energy per unit length, whereby equations (5.11) and (5.35) are used in combination with the following decomposition of the Burgers vector.

As has been outlined in section 5.6, for a mixed dislocation the total Burgers vector, b, can be decomposed into its screw and edge components, b_s and b_e, respectively:

$$b = b_s + b_e \tag{5.39}$$

Where

$$\begin{aligned} b_s &= b\cos\beta \\ b_e &= b\sin\beta \end{aligned} \tag{5.40}$$

Inserting these expressions into equations (5.11) and (5.35), and superposing them results:

$$\frac{W}{L} = \frac{Gb^2}{4\pi}\left(\left(\cos^2\beta\right) + \frac{\sin^2\beta}{1-\upsilon}\right)\ln\frac{\alpha R}{b} = E\left(\beta\right)\ln\frac{\alpha R}{b} \tag{5.41}$$

Here $E(\beta)$ is termed the pre-logarithmic factor.

To determine the force per unit length acting on the dislocation, it is helpful to consider the effective operation required to displace it. To do this, the following process can be applied; make a cut in the material of area $\boldsymbol{\xi} \times \delta\boldsymbol{r}$**,** per unit length of $\boldsymbol{b}$ and move the material uniformly over the cut by the amount $b_e\delta h$, where δh is the distance climbed normal to the glide plane. Finally restore continuity of the material by displacing the opposite surfaces of the cut relative to one another by the amount $\boldsymbol{b}$**.**

During this operation, work is done by the stress acting over the dislocation core. The work done is quantified by:

$$\frac{\delta W}{L} = \frac{\boldsymbol{F}}{L}\cdot\delta\boldsymbol{r} = \left[\boldsymbol{\sigma}\cdot\left(\boldsymbol{\xi}\times\delta\boldsymbol{r}\right)\right]\cdot\boldsymbol{b} \tag{5.42}$$

Where $\boldsymbol{\sigma}\cdot(\boldsymbol{\xi}\times\delta\boldsymbol{r})$ is the force caused by the stress tensor on the surface $(\boldsymbol{\xi}\times\delta\boldsymbol{r})$**.**

Equation (5.42) can be re-arranged to the form:

$$\frac{\boldsymbol{F}}{L}\cdot\delta\boldsymbol{r} = \left(\boldsymbol{b}\cdot\boldsymbol{\sigma}\right)\cdot\left(\boldsymbol{\xi}\times\delta\boldsymbol{r}\right) = \left[\left(\boldsymbol{b}\cdot\boldsymbol{\sigma}\right)\times\boldsymbol{\xi}\right]\cdot\delta\boldsymbol{r} \tag{5.43}$$

Now, eliminating the $\delta\boldsymbol{r}$ multiplier from both sides results in the expression for the force per unut length acting on the dislocation:

$$\frac{\boldsymbol{F}}{L} = (\boldsymbol{b}\cdot\boldsymbol{\sigma})\times\boldsymbol{\xi} \tag{5.44}$$

Or in index form:

$$F_k = -\epsilon_{ijk}\xi_i\sigma_{jl}b_l \tag{5.45}$$

Where ϵ_{ijk} is the permutation operator.

Finally, the total force has glide and climb components, F_{gl} and F_{cl}, respectively:

$$\frac{F_{gl}}{L} = \frac{\left[(\boldsymbol{b}\cdot\boldsymbol{\sigma})\times\boldsymbol{\xi}\right]\cdot\left[\boldsymbol{\xi}\times(\boldsymbol{b}\times\boldsymbol{\xi})\right]}{|\boldsymbol{b}\times\boldsymbol{\xi}|} \tag{5.46}$$

$$\frac{F_{cl}}{L} = \frac{\left[(\boldsymbol{b}\cdot\boldsymbol{\sigma})\times\boldsymbol{\xi}\right]\cdot(\boldsymbol{b}\times\boldsymbol{\xi})}{|\boldsymbol{b}\times\boldsymbol{\xi}|} \tag{5.47}$$

5.11 Effective mass of dislocations

The concept of dislocation mass can be developed through consideration of the elastic strain field and the stored elastic energy in the dislocation core.

It is first important to state that physically a dislocation is merely a distortion or disturbance in the arrangement of atoms in a crystal, so assigning a mass is not physical, however it is often useful to consider the dislocation to be analogous to a piece of string, whereby it possesses a real mass and tension (Suzuki, et al., 1991). It is observed that, as a dislocation moves, the elastic strain field surrounding it shrinks in the direction of motion. This decrease in strain field results in an increase in the stored elastic energy by the dislocation core. The increase in stored energy with increasing velocity can be calculated by application of the Lorenz transformation (Suzuki, et al., 1991):

$$E = \frac{E_0}{\sqrt{1-\frac{V^2}{c_t^2}}} \tag{5.48}$$

Where E_0 is the 'rest' energy, V is the velocity of the dislocation and c_t is the shear wave speed.

From equation (5.48) it can be seen that as $V \to c_t$, $E \to \infty$.

The well-known equation from relativity theory, provides a mass-energy equivalence relationship, therefore, in a similar fashion an effective mass of dislocations can be written as (Meyers, 1994):

$$m = \frac{m_0}{\sqrt{1 - \frac{V^2}{c_t^2}}} \tag{5.49}$$

Where m is the effective mass and m_0 is the 'rest' mass.

An estimate for the value of the rest mass can be obtained by treating the case of a static dislocation and equating the stored energy to the rest mass multiplied by c_t^2. The stored energy of a static screw dislocation is found in section 5.7 to be:

$$E_0 = \frac{Gb^2}{4\pi} \ln \frac{R}{r_0} \tag{5.50}$$

Applying the relation, $E_0 = m_0 c_t^2$ results:

$$m_0 c_t^2 = \frac{Gb^2}{4\pi} \ln \frac{R}{r_0} \tag{5.51}$$

Substituting $c_t = \sqrt{G/\rho}$ and re-arranging provides an estimate for the rest mass as:

$$m_0 = \frac{\rho b^2}{4\pi} \ln \frac{R}{r_0} \tag{5.52}$$

As a result of this relativistic effect, the velocity of dislocations are limited to speeds lower than the shear wave speed. It is expected that as a dislocation is accelerated, at speeds much lower than the shear wave speed, a linear relationship will be observed between the dislocation velocity and the applied stress. As the dislocation velocity approaches the shear wave speed, it will asymptotically approach the limiting value.

5.12 Dislocation interactions

Real crystalline materials contain large numbers of dislocations. Therefore it is inevitable that during deformation, there will be interaction between dislocations. There are a number of ways in which this can happen, with the key processes outlined in this section.

In a real crystal, there will be a large number of dislocations contained within it, ranging from a few thousand to many millions, depending on the previous work done to the material. Therefore, it is inevitable that during deformation, and therefore during dislocation motion, there will be interaction between dislocations. This occurs in many forms, with the outcome resulting in either immobilisation of the dislocations, therefore preventing it from gliding further, multiplication of the dislocation, further dislocations are generated, or annihilation, where two dislocations of opposite sign combine to result in a perfect piece of crystal.

The processes leading to the immobilisation and annihilation of dislocations make it harder for other dislocations to propagate through the crystal, therefore increasing the load required to drive plastic deformation, i.e these processes cause the crystal to harden.

5.13 Work hardening

An important behaviour of metals during deformation is the rate at which work hardening occurs; the change in the resistance to dislocation motion during deformation. It is well established that when the resolved shear stress is plotted against strain, the slope of which determines the work hardening, three distinct stages are observed. Figure 5-16 shows an example of this for a typical fcc metal. The three stages observed are closely related to the dislocation kinematics during material deformation.

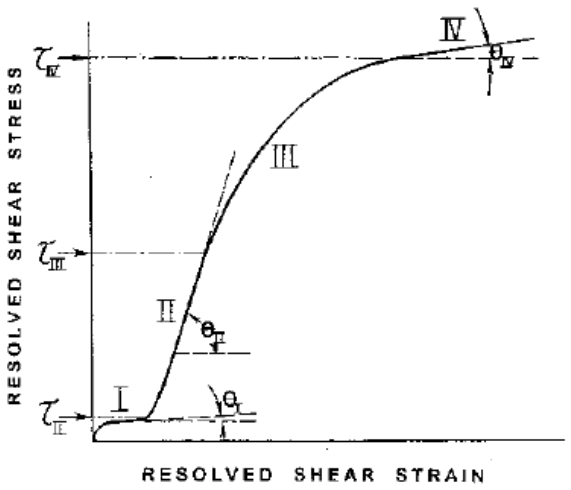

Figure 5-16: Idealised strain-hardening curve typical of fcc metal showing 4 stages (Kuhlmann-Wilsdorf, 2004)

From Figure 5-16, stage I shows little increase in the hardening and the slope, θ_I, or rate of work hardening, is found to be $\theta_I \approx 10^{-4}G$, where G is the shear modulus (Hull & Bacon, 2001). This stage is typically referred to as the 'stage of easy glide', and strain occurring during this stage occurs only on the primary slip system. During this stage, multiplication of dislocations occurs on the primary slip system, however very few dislocations are generated on secondary slip systems.

Stage II begins when secondary slip systems become active. During stage II the rate of hardening, the slope, θ_{II}, is significantly higher than in stage I and is typically in the region between, $\theta_{II} \approx 3 \times \theta_I$ and $\theta_{II} \approx 10 \times \theta_I$ (Hull & Bacon, 2001). The increase in work hardening observed during stage II is due to the densities of dislocations increasing on the secondary slip systems; dislocations on intersecting slip planes interact with one another, reducing or totally inhibiting their mobility.

Finally it is seen in Figure 5-16 that the third stage, Stage III, shows a reduction in the rate of work hardening, the slope, θ_{III}, is less than during that of stage II.

5.14 Summary

The key microscale properties and processes for the development of the dislocation based model have been detailed. The crystal structures of interest to

this work (fcc and bcc) have been discussed, along with the important vectors, the Burgers vector and the slip plane normal, which define the slip systems in a crystal. The forces acting on dislocations which can cause motion, and consequently plastic deformation have been derived. These forces are used in the dislocation based model for driving plasticity. Finally, a discussion has been made regarding the multistage nature of dislocation hardening. This multiscale nature is used later to verify the initial testing of the model.

6 Dislocation based plasticity model

This chapter describes the dislocation based continuum scale shock plasticity model. The chapter starts by derivation of the key plastic strain rate equation, the Generalised Orowan equation, which provides the link between the microscale variables and the continuum scale. Following this, the evolution of the dislocation based internal state variables are discussed in turn.

It has been identified in previous work that the basis of this work should consist of the constitutive model developed by Mayer et al. (Mayer, et al., 2013). This model, from herein referred to as the Mayer model, was developed to model plasticity and fracture of metals at shock loading. As is identified in (Kiely, 2013) only the plasticity part of this model is of interest in this work due to large inaccuracies of the fracture representation compared to the damage model available in (Djordjevic, 2011).

In (Kiely, 2013) the Mayer model (Mayer, et al., 2013) is shown to have potential for the basis of future improvements to the current continuum modelling capabilities available at present due to a number of reasons. Firstly, the model is multiscale in nature. This means that deformation can be reproduced on a continuum scale using properties and processes on the microscale to evolve plasticity. An advantage of this is the full model will be able to capture details that would otherwise only be obtainable in a molecular dynamics simulation over time and length scale only currently achievable with continuum modelling.

The Mayer model provides the update of stress deviators in terms of the elastic strain, in line with the commonly used method in hydrocode modelling.

$$S_{ik} = 2G\left[u_{ik} - \frac{1}{3}\delta_{ik}\sum_{i=1}^{N}\left(u_{ll}\right) - w_{ik} \right] \tag{6.1}$$

Where S_{ik} is the stress deviators, G is the shear modulus, u_{ik} is the total strain, δ_{ik} is the Kronecker delta and w_{ik} is the plastic strain.

6.1 Rate of plastic strain

The plastic strain tensor updated from the rate of plastic strain. The plastic strain rate is calculable from the dislocation density and velocity via the Orowan equation. This simple relation can easy be derived by considering the passage of a single dislocation through and otherwise perfect piece of crystal.

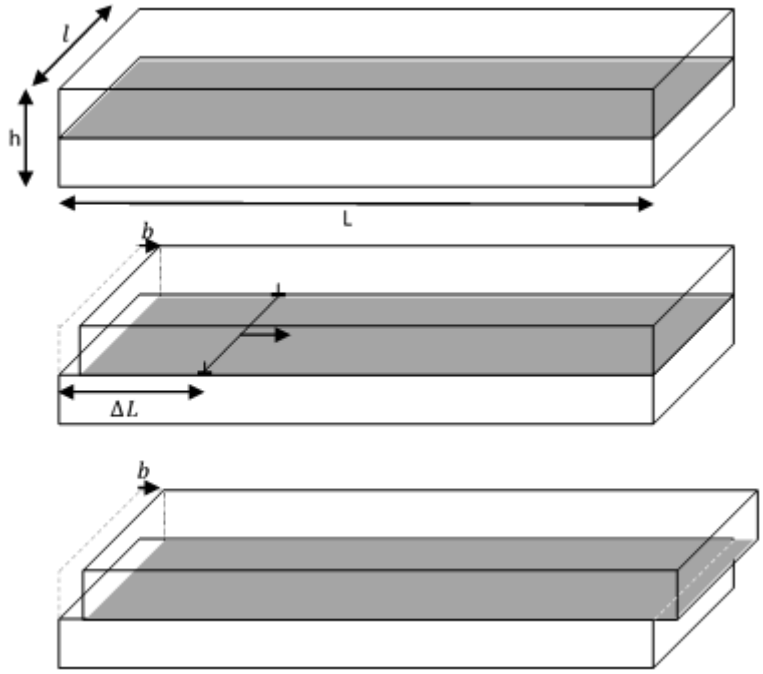

Figure 6-1:Schematic diagrams showing an un-deformed piece of crystal, the same piece of crystal where a dislocation has glided partially through it, and finally the piece of crystal after a dislocation has propagated completely through it.

Considering the piece of crystal shown in Figure 6-1 it is seen that its volume is

$$V = Lhl \tag{6.2}$$

If a single, straight dislocation propagates fully through the entire crystal, then the added shear strain will be:

$$\gamma = \frac{b}{h} \tag{6.3}$$

However, in the case of a single dislocation propagating through only part of the crystal, as is shown in Figure 6-1 then the added shear strain is

$$\gamma = \frac{\Delta L}{L}\frac{b}{h} \tag{6.4}$$

Now consider multiple dislocations gliding through the same piece of crystal, the added shear strain will be:

$$\gamma = N\frac{\Delta L}{L}\frac{b}{h} = \frac{Nl}{l}\frac{\Delta L}{L}\frac{b}{h} = \frac{Nl\Delta Lb}{V} \tag{6.5}$$

The dislocation density can be defined as:

$$\rho = \frac{Nl}{V} \tag{6.6}$$

Substitution of this into equation (6.5) results:

$$\gamma = \rho\Delta Lb \tag{6.7}$$

Finally, the rate of plastic strain is given by the derivative of equation (6.7) with respect to time:

$$\dot{\gamma} = \frac{\partial\gamma}{\partial t} = \frac{\partial\left(\rho\Delta Lb\right)}{\partial t} = \rho b\frac{\partial\left(\Delta L\right)}{\partial t} \tag{6.8}$$

$$\dot{\gamma} = \rho bv \tag{6.9}$$

Where v is the average velocity of dislocations during glide.

Equation (6.9) is the Orowan equation relating microscale dislocation processes to macroscale plastic strain rate.

This analysis so far only considers dislocations in a single slip system. In crystals there are several slip systems active and therefore these must be taken into account when calculating the total plastic strain. This is achieved projecting the rates of shear onto the directions of the slip systems using Schmid's tensor (Meyers, 1994) and then summing over all slip systems:

$$\boldsymbol{u}^{pl} = \sum_{\beta}\dot{\gamma}\left(\boldsymbol{s}^{\beta}\otimes\boldsymbol{n}^{\beta}\right) \tag{6.10}$$

Where $\boldsymbol{s}$ is the direction of slip and $\boldsymbol{n}$ is the unit vector normal to the slip plane and β indicates that the values are for a specified slip system. The total rate of plastic deformation can then be decomposed into the rate of plastic strain and the rate of spin, $\dot{\boldsymbol{\varepsilon}}^{p}$ and $\boldsymbol{d}$, respectively:

$$\dot{\boldsymbol{\varepsilon}}^{pl} = \frac{1}{2}\sum_{\beta}\dot{\gamma}^{\beta}\left(\left(\boldsymbol{s}^{\boldsymbol{\beta}} \otimes \boldsymbol{n}^{\boldsymbol{\beta}}\right) + \left(\boldsymbol{n}^{\boldsymbol{\beta}} \otimes \boldsymbol{s}^{\boldsymbol{\beta}}\right)\right) \tag{6.11}$$

$$\mathbf{d} = \frac{1}{2}\sum_{\beta}\dot{\gamma}^{\beta}\left(\left(\boldsymbol{s}^{\boldsymbol{\beta}} \otimes \boldsymbol{n}^{\boldsymbol{\beta}}\right) - \left(\boldsymbol{n}^{\boldsymbol{\beta}} \otimes \boldsymbol{s}^{\boldsymbol{\beta}}\right)\right) \tag{6.12}$$

From equation (6.9) it is apparent that in order to determine the rate of plastic strain, the dislocation velocity as well as the density of mobile dislocations is required to be known. The following sections will discuss in turn how each of these are determined.

6.2 Equation of motion

Following the derivations of the forces acting upon dislocations in section 5.10, an equation of motion is developed for dislocations by Mayer. The equation of motion has the form of Newton's second Law of motion, and is simply the mass multiplied by acceleration on the left hand side, with the right hand side being a sum of the forces acting on the dislocation. The equation is then written as:

$$m_0\zeta_{\beta}^{3}\frac{dV_D^{\beta}}{dt} = \left[\sum_{i=1}^{N}\sum_{k=1}^{N}S_{ik}b_i^{\beta}n_k^{\beta} \pm \frac{1}{2}bY\right] - B\zeta_{\beta}^{3}V_D^{\beta} \tag{6.13}$$

It is seen that the right hand side of equation (6.13) is a summation of the force acting on dislocations from external mechanical stress, minus the resistance yield resistance of the crystal and minus the dynamic drag caused by phonon interaction. In line with equations (6.10), (6.11) and (6.12), the superscript β's indicate the values are for a specific slip system, specified by the Burger's vector and the normal to the slip plane, $\boldsymbol{b}$ and $\boldsymbol{n}$, respectively.

The first term on the right hand side is the mechanical force acting on dislocations as is derived in section 5.10. The second term is the 'static resistance', where the yield strength Y is calculated by:

$$Y = Y_0 + A_I Gb\sqrt{\rho_I} \tag{6.14}$$

Where Y_0 accounts for the resistance due to the Peierls barrier, that is the stress required to move a single dislocation in an otherwise perfect crystal, A_I is a coefficient calculated from curve fitting, and ρ_I is the total immobilise dislocation density, where:

$$\rho_I = \sum_{\beta} \rho_I^{\beta} \tag{6.15}$$

It is observed that, for dislocation acceleration to occur, the Peach-Koehler force acting on the dislocation must be greater than the static friction term. The plus/minus sign appears in the equation of motion as the force from mechanical stresses must always be of opposite sign to the resistance.

6.2.1 Resistance forces

The second resistive term on the right hand side of equation (6.13) accounts for the dynamic drag of dislocations. As a dislocation is accelerated through a crystal, it experiences a drag force due to interactions with conduction electrons and phonons (Suzuki, et al., 1991). This drag force is proportional to the velocity of the dislocation, and is determined by the multiplication of the coefficient of dynamic drag, B.

In general, B is given to be a sum of the friction coefficient due to conduction electrons, B_e and the friction coefficient due to phonon interactions, B_p. However, in Mayer's formulation of the equation of dislocation motion only phonon drag is taken into account, therefore $B = B_p$.

Phonon friction arises as, when the dislocation is in motion, it is forced to oscillate by other lattice vibrations, i.e. phonons. These forced oscillations results in the dissipation of energy from the dislocation, resulting in the dislocation

experiencing an effecting retarding force. The coefficient of phonon friction is given by Mayer (Mayer, et al., 2013) and also by Suzuki (Suzuki, et al., 1991) to be:

$$B = \frac{4\theta^2 k_B^3}{h^2 c_b^3} T \tag{6.16}$$

Where θ is the Debye temperature, k_B is the Boltzmann constant, h is Planck's constant, c_b is the bulk speed of sound, and T is the temperature.

6.3 Evolution of dislocation densities

The second key calculations required for the calculation of the plastic strain caused by dislocation motion is the updates of the densities of the mobile and immobilised dislocations. Equations governing the rates of change of these densities are given by Mayer (Mayer, et al., 2013) in the form:

$$\frac{d\rho_D^\beta}{dt} = Q_D^\beta - Q_I^\beta - k_a b \left| V_D^\beta \right| \rho_D^\beta \left(2\rho_D^\beta + \rho_I^\beta \right) \tag{6.17}$$

$$\frac{d\rho_I^\beta}{dt} = Q_I^\beta - k_a b \left| V_D^\beta \right| \rho_D^\beta \rho_I^\beta \tag{6.18}$$

where Q_D^β is the rate of generation of new mobile dislocations, Q_I^β is the rate of immobilisation of previously mobile dislocations, k_a is a coefficient of annihilation.

Physically, equation (6.17) is saying that the rate of change of density of mobile dislocations on the slip system β is equal to the rate at which new dislocations are generated during deformation, minus the rate at which existing mobile dislocations are immobilised minus the rate at which annihilation occurs between mobile dislocations with other mobile dislocations and also with immobilised dislocation.

Equation (6.18) physically says that the rate of change in density of immobilised dislocations on the slip systems β is equal to the rate at which mobile dislocations are immobilised minus the rate at which previously immobile dislocation are annihilated by mobile dislocations.

The rate of generation of new mobile dislocations in equation (6.17) is written in terms of the work done during dislocation motion in overcoming resistance forces, multiplied by a coefficient of generation, k_g.

$$Q_D^\beta = k_g b \left[\frac{2B\left(V_D^\beta\right)^2}{\sqrt{1-\left(V_D^\beta / c_t\right)^2}} + bY\left|V_D^\beta\right| \right] \rho_D^\beta \tag{6.19}$$

It can be seen that the term in the brackets in equation (6.19) is simply the resistance forces from the equation of dislocation motion, equation (6.13) multiplied by the velocity of dislocations. These forces multiplied by the velocity physically result in the power dissipated during plastic deformation. This is transformed into the number of dislocations generated per unit time by the definition of the coefficient k_g. It is established during calorimetric experiments that a certain percentage of the energy dissipated plastically is used by the metal for the generation of new dislocations, this percentage is approximately ten percent (Krasnokov, et al., 2011) (Mayer, et al., 2013). Taking this portion of energy and dividing it by the energy required to form a single dislocation in the crystal results in the number of dislocations generated when this value is multiplied by the energy dissipated.

$$k_g = \frac{\eta}{\epsilon_L} \tag{6.20}$$

Where η is the portion of power dissipated overcoming resistance forces and ϵ_L is the energy per unit line required for generation of new dislocations, where the value of ϵ_L is found to be approximately $8\ eV/b$.

Right hand side of (6.19) is finally multiplied by ρ_D^β as, the term contain inside the brackets and then multiplied by k_g provides the power dissipated by a single dislocation, and therefore by multiplication of the number of dislocations per unit area, this will result in the number generated per unit area of the slip system.

The rate of immobilisation, Q_I^β, which is present in both equations (6.17) and (6.18) determined via the following relation:

$$Q_I^\beta = V_I \left(\rho_D^\beta - \rho_0 \right) \sqrt{\rho_I^\beta} \tag{6.21}$$

This relation is written by making the assumption that, when the mobile dislocation density reaches a certain threshold, value of ρ_0, all excess mobile dislocation will be immobilised into dislocation structures. This immobilisation occurs over a characteristic time, τ_c, during which the dislocation will move a characteristic distance, l_c. Combining these two characteristic values results in definition of the characteristic velocity of dislocations during the immobilisation process, V_I:

$$V_I = \frac{l_c}{\tau_c} \tag{6.22}$$

The characteristic distance is estimated as $l_c \approx \left(\rho_I^\beta \right)^{-\frac{1}{2}}$, so by substitution and rearrangement, the characteristic time is estimated as:

$$\tau_c \approx \frac{1}{V_I \sqrt{\rho_I^\beta}} \tag{6.23}$$

Simple division of the number of dislocations above the threshold value, ρ_0, by this characteristic time results in the rate of immobilisation expression, equation (6.21).

6.4 Summary

The formulation of the dislocation based continuum plasticity shock model has been outlined. The key equation for calculation of the rate of plastic strain, the Generalised Orowan equation, has been derived, before the evolution of the internal state variable have been discussed in turn. Implementation of this model in the hydrocode is described in the next chapter

7 Implementation of the dislocation based plasticity model in DYNA3d

The implementation of the model described in chapter 6 in the DYNA3d hydrocode is described in this chapter. An overview of the hydrocode is firstly presented, followed by a discussion of the numerical schemes used for integration of the model. The system of equations is then presented in algorithmic style, firstly for the update of the deviatoric stress then the pressure update, which includes coupling of the model with an equation of state.

7.1 Overview of the DYNA3d hydrocode

The first stage of model development is to implement the model published by Mayer et al. (Mayer, et al., 2013) into the hydrocode available at Brunel University. The code available is DYNA3d. DYNA3d is an explicit, non-linear hydrocode developed by Lawrence Livermore National Laboratories (LLNL), and is an open source research code. DYNA3d contains many features of standard finite element codes, including (Kiely, 2013):

- Different element formulations, including 3d solid elements, 2d shell element and beam and truss elements
- Boundary, initial and loading conditions
- A range of contact algorithms
- Several equations of state which are coupled to the relevant material models
- A large number of constitutive models applicable to a wide range of materials and deformation conditions

The new dislocation model is being implemented as material model number 224 (mat_224) and is coupled with the vector equation of state available, and makes use of the stress decomposition proposed by (Vignjevic, et al., 2008) and used previously by (Djordjevic, 2011).

7.2 Implementation of the dislocation densities based model for deviatoric stress update

Following the initialisation phase, the update of the stress deviators is performed using the dislocation based plasticity model. To achieve this, the rate of change of dislocation densities equations are integrated numerically using an improved Euler method. The improved Euler method is a predictor-corrector method consisting of two steps; first predicted values are calculated using the forward Euler method, these predicted values are then used to calculate the predicted rate of change at the next time instant, with the final update performed using the mean of the rate of change at the previous and next time instances. Integration of the dislocation velocity is performed using an analytical solution which is available in (Krasnokov, et al., 2011).

7.2.1 System of equations

The first step in the update of the deviatoric stress is the rotation of all variable into the material coordinate system. The lattice vectors calculated during the initialisation are determined in the material coordinate system, but the strain rate, strains and stress are all stored in the global coordinate system. This transformation is achieved simply by applying the rotation matrix, determined from the element coordinates and input material axes options, to the tensors of interest.

With all the history variables now in the same coordinate system, update of the deviatoric stress can be calculated.

The first steps of the deviatoric stress update are the calculations of the material stiffness and compliance matrices from the input material properties.

$$\mathbf{C} = \frac{1}{\Delta}\begin{bmatrix} \frac{1-\nu_{23}\nu_{32}}{\mathrm{E}_2\mathrm{E}_3} & \frac{\nu_{21}+\nu_{23}\nu_{31}}{\mathrm{E}_2\mathrm{E}_3} & \frac{\nu_{31}+\nu_{21}\nu_{32}}{\mathrm{E}_2\mathrm{E}_3} & 0 & 0 & 0 \\ \frac{\nu_{12}+\nu_{32}\nu_{13}}{\mathrm{E}_1\mathrm{E}_3} & \frac{1-\nu_{13}\nu_{31}}{\mathrm{E}_1\mathrm{E}_3} & \frac{\nu_{32}+\nu_{12}\nu_{31}}{\mathrm{E}_1\mathrm{E}_3} & 0 & 0 & 0 \\ \frac{\nu_{13}+\nu_{12}\nu_{23}}{\mathrm{E}_1\mathrm{E}_2} & \frac{\nu_{23}+\nu_{13}\nu_{21}}{\mathrm{E}_1\mathrm{E}_2} & \frac{1+\nu_{12}\nu_{21}}{\mathrm{E}_1\mathrm{E}_2} & 0 & 0 & 0 \\ 0 & 0 & 0 & G_{23}\Delta & 0 & 0 \\ 0 & 0 & 0 & 0 & G_{31}\Delta & 0 \\ 0 & 0 & 0 & 0 & 0 & G_{12}\Delta \end{bmatrix} \quad (7.1)$$

Where $\Delta = \left(1-\nu_{12}\nu_{21}-\nu_{23}\nu_{32}-\nu_{31}\nu_{13}-2\nu_{21}\nu_{32}\nu_{13}/\mathrm{E}_1\mathrm{E}_2\mathrm{E}_3\right)$

$$B_{ijkl} = \begin{bmatrix} \frac{1}{\mathrm{E}_1} & \frac{-\nu_{21}}{\mathrm{E}_2} & \frac{-\nu_{31}}{\mathrm{E}_3} & 0 & 0 & 0 \\ \frac{-\nu_{12}}{\mathrm{E}_1} & \frac{1}{\mathrm{E}_2} & \frac{-\nu_{32}}{\mathrm{E}_3} & 0 & 0 & 0 \\ \frac{-\nu_{13}}{\mathrm{E}_1} & \frac{-\nu_{23}}{\mathrm{E}_2} & \frac{1}{\mathrm{E}_3} & 0 & 0 & 0 \\ 0 & 0 & 0 & \frac{1}{G_{23}} & 0 & 0 \\ 0 & 0 & 0 & 0 & \frac{1}{G_{31}} & 0 \\ 0 & 0 & 0 & 0 & 0 & \frac{1}{G_{12}} \end{bmatrix} \quad (7.2)$$

Now calculate the ψ_{ij} tensor required for the generalised pressure update:

$$\psi_{(ii)} = \frac{C_{i1}+C_{i2}+C_{i3}}{\sqrt{\frac{\left(C_{11}+C_{12}+C_{13}\right)^2+\left(C_{12}+C_{22}+C_{23}\right)^2+\left(C_{13}+C_{23}+C_{33}\right)^2}{3}}} \quad (7.3)$$

Next, the deviatoric part of the Piola-Kirchhoff stress tensor is defined, according to the decomposition outlined in section 3.10:

$$ {}^{n}\bar{\boldsymbol{S}}^{\tilde{D}} = {}^{n}\bar{\boldsymbol{S}} + {}^{n}\bar{P}\boldsymbol{\psi} \tag{7.4} $$

With the rate of deviatoric stress defined:

$$ {}^{n+1/2}\dot{\bar{\boldsymbol{S}}}^{\tilde{D}} = {}^{n+1/2}\dot{\bar{\boldsymbol{S}}} - {}^{n+1/2}\dot{\bar{P}}\boldsymbol{\psi} = {}^{n+1/2}\dot{\bar{\boldsymbol{S}}} - \frac{1}{3}\left({}^{n+1/2}\dot{\bar{\boldsymbol{S}}} : \boldsymbol{\psi} \right)\boldsymbol{\psi} \tag{7.5} $$

Trial stress is now calculated. This is done by making the assumption that the increment is elastic deformation only. The trial value (denoted by the superscript asterisk) is obtained at the middle of the time step by:

$$ {}^{*n+1}\bar{\boldsymbol{C}}_e = {}^{n}\bar{\boldsymbol{C}}_e + {}^{*n+1/2}\dot{\bar{\boldsymbol{C}}}_e \, {}^{n+1/2}\Delta t \tag{7.6} $$

$$ {}^{*n+1/2}\bar{\boldsymbol{C}}_e = \frac{1}{2}\left({}^{n}\bar{\boldsymbol{C}}_e + {}^{*n+1/2}\dot{\bar{\boldsymbol{C}}}_e \, {}^{n+1/2}\Delta t + {}^{n}\bar{\boldsymbol{C}}_e \right) = {}^{n}\bar{\boldsymbol{C}}_e + \frac{1}{2} {}^{*n+1/2}\dot{\bar{\boldsymbol{C}}}_e \, {}^{n+1/2}\Delta t \tag{7.7} $$

The rate of trial elastic deformation now defined:

$$ {}^{*n+1/2}\dot{\bar{\boldsymbol{C}}}_e = {}^{n+1/2}\bar{\boldsymbol{C}}_e \left[{}^{n+1/2}\bar{\boldsymbol{d}} - {}^{n+1/2}\bar{\boldsymbol{d}}_p \right] = {}^{n+1/2}\bar{\boldsymbol{C}}_e \, {}^{n+1/2}\bar{\boldsymbol{d}} \tag{7.8} $$

Equation (7.7) in combination with equation (7.8) yields:

$$ {}^{*n+1/2}\bar{\boldsymbol{C}}_e = {}^{n}\bar{\boldsymbol{C}}_e \left[1 - \frac{1}{2} {}^{n+1/2}\bar{\boldsymbol{d}} \, {}^{n+1/2}\Delta t \right]^{-1} \tag{7.9} $$

The increment of the trial second Piola Kirchhoff stress is then obtained as:

$$
\begin{aligned}
{}^{*n+1/2}\dot{\bar{\boldsymbol{S}}} &= \bar{\mathbb{C}} : {}^{n+1/2}\dot{\bar{\boldsymbol{E}}}_e \\
&= \bar{\mathbb{C}} : \left(\left[{}^{n+1/2}\bar{\boldsymbol{C}}_e \left({}^{n+1/2}\bar{\boldsymbol{d}} - {}^{n+1/2}\bar{\boldsymbol{d}}_p \right) \right] - \left[{}^{n+1/2}\bar{\boldsymbol{C}}_d \, {}^{n+1/2}\bar{\boldsymbol{d}}_d \right] \right) \\
&= \bar{\mathbb{C}} : \left[{}^{*n+1/2}\bar{\boldsymbol{C}}_e \, {}^{n+1/2}\bar{\boldsymbol{d}} \right] \\
&= \bar{\mathbb{C}} : {}^{n}\bar{\boldsymbol{C}}_e \left[1 - \frac{1}{2} \, {}^{n+1/2}\bar{\boldsymbol{d}} \, {}^{n+1/2}\Delta t \right]^{-1} {}^{n+1/2}\bar{\boldsymbol{d}}
\end{aligned}
\tag{7.10}
$$

And then used to calculate the increment of the deviatoric stress:

$$
\begin{aligned}
{}^{*n+1/2}\dot{\bar{\boldsymbol{S}}}^{\tilde{D}} &= {}^{*n+1/2}\dot{\bar{\boldsymbol{S}}} - \frac{1}{3}\left({}^{*n+1/2}\dot{\bar{\boldsymbol{S}}} : \boldsymbol{\psi} \right)\boldsymbol{\psi} \\
&= \bar{\mathbb{C}} : {}^{n}\bar{\boldsymbol{C}}_e \left[1 - \frac{1}{2} \, {}^{n+1/2}\bar{\boldsymbol{d}} \, {}^{n+1/2}\Delta t \right]^{-1} {}^{n+1/2}\bar{\boldsymbol{d}} \\
&- \frac{1}{3}\left(\bar{\mathbb{C}} : {}^{n}\bar{\boldsymbol{C}}_e \left[1 - \frac{1}{2} \, {}^{n+1/2}\bar{\boldsymbol{d}} \, {}^{n+1/2}\Delta t \right]^{-1} {}^{n+1/2}\bar{\boldsymbol{d}} : \boldsymbol{\psi} \right)\boldsymbol{\psi}
\end{aligned}
\tag{7.11}
$$

Deviatoric part of stress is then updated in the isoclinic configuration:

$$
\begin{aligned}
{}^{*n+1}\bar{\boldsymbol{S}}^{\tilde{D}} &= {}^{n}\bar{\boldsymbol{S}}^{\tilde{D}} + {}^{n+1/2}\dot{\bar{\boldsymbol{S}}}^{\tilde{D}} \, {}^{n+1/2}\Delta t \\
&= {}^{n}\bar{\boldsymbol{S}} + {}^{n}\bar{P}\boldsymbol{\psi} + \left(\begin{array}{c} \bar{\mathbb{C}} : {}^{n}\bar{\boldsymbol{C}}_e \left[1 - \frac{1}{2} \, {}^{n+1/2}\bar{\boldsymbol{d}} \, {}^{n+1/2}\Delta t \right]^{-1} {}^{n+1/2}\bar{\boldsymbol{d}} - \\ \\ -\frac{1}{3}\left(\bar{\mathbb{C}} : {}^{n}\bar{\boldsymbol{C}}_e \left[1 - \frac{1}{2} \, {}^{n+1/2}\bar{\boldsymbol{d}} \, {}^{n+1/2}\Delta t \right]^{-1} {}^{n+1/2}\bar{\boldsymbol{d}} : \boldsymbol{\psi} \right)\psi \end{array} \right)\Delta t
\end{aligned}
\tag{7.12}
$$

The main plasticity calculation is now ready to be performed. The first step of this is the calculation of the slip deformation and slip spin tensors, by

$$
{}^{n}slpdef^{\beta} = \frac{1}{2}\left({}^{n}b_i^{\beta} \, {}^{n}n_k^{\beta} + {}^{n}b_k^{\beta} \, {}^{n}n_i^{\beta} \right) \tag{7.13}
$$

$$
{}^{n}slpspn^{\beta} = \frac{1}{2}\left({}^{n}b_i^{\beta} \, {}^{n}n_k^{\beta} - {}^{n}b_k^{\beta} \, {}^{n}n_i^{\beta} \right) \tag{7.14}
$$

Which are later used to resolve the plastic strain increments in the correct directions, as well as being used in the update of the lattice vectors.

Next summation of the immobile dislocation density over all slip systems is performed in order to set up the calculation of the yield strength, where ${}^{n}\rho_I$ is the current total immobile dislocation density, ${}^{n}\rho_I = \sum_{\beta} {}^{n}\rho_I^{\beta}$.

$$ {}^{n}Y = Y_0 + A_I G b \sqrt{{}^{n}\rho_I} \tag{7.15} $$

The mechanical force acting on the dislocations is now calculated from the deviatoric stress:

$$ {}^{n}F_D^{\beta} = {}^{n}S_{ik}\, {}^{n}b_i\, {}^{n}n_k \tag{7.16} $$

Which allows for assessment of whether plasticity will occur on the slip system β . For plasticity to occur, the resolved force driving dislocation motion must have a greater magnitude than the static friction inherent in the lattice, $\frac{1}{2} b Y$, which is summarised by the plasticity criterion:

$$ \left| {}^{n}F_D^{\beta} \right| > \frac{1}{2} b\, {}^{n}Y \tag{7.17} $$

If the mechanical force has a magnitude lower than the static friction, a purely elastic response is assumed on that slip system, with the remainder of the plasticity calculation skipped, and the plastic strain rate set to zero for the slip system. However, assuming the mechanical force has greater magnitude than the static resistance, mobile dislocations will move and plasticity will occur on the slip system.

The dynamic drag coefficient and the shear wave speeds are now calculated by equations (7.18) and (7.19), respectively.

$$ B = \frac{4\theta^2 k_b^3}{h^2\, {}^{n}c_b^3} T \tag{7.18} $$

$$ c_t = \sqrt{\frac{G}{\rho}} \tag{7.19} $$

The rate of generation of new mobile dislocations and the rate of immobilisation of dislocations, respectively, at the current time are now calculated for use in the first stage of the dislocation density updates.

$$ {}^{n}Q_D^{\beta} = k_g b \left[\frac{2B\left({}^{n}V_D^{\beta}\right)^2}{\sqrt{1-\left(\frac{{}^{n}V_D^{\beta}}{c_t}\right)^2}} + b\,{}^{n}Y\left|{}^{n}V_D^{\beta}\right| \right] {}^{n}\rho_D^{\beta} \tag{7.20} $$

$$ {}^{n}Q_I^{\beta} = V_I\left({}^{n}\rho_D^{\beta} - \rho_0\right)\sqrt{{}^{n}\rho_I^{\beta}} \tag{7.21} $$

The results of equations (7.20) and (7.21) are now used in for the calculation of the rate of change of the dislocation densities at the current time instant:

$$ {}^{n}\dot{\rho}_D^{\beta} = {}^{n}Q_D^{\beta} - {}^{n}Q_I^{\beta} - k_a b\left|{}^{n}V_D^{\beta}\right|{}^{n}\rho_D^{\beta}\left(2\,{}^{n}\rho_D^{\beta} + {}^{n}\rho_I^{\beta}\right) \tag{7.22} $$

$$ {}^{n}\dot{\rho}_I^{\beta} = {}^{n}Q_I^{\beta} - k_a b\left|{}^{n}V_D^{\beta}\right|{}^{n}\rho_D^{\beta}\,{}^{n}\rho_I^{\beta} \tag{7.23} $$

The forward Euler is now applied to determine the ‘predicted’ values of updated dislocation densities, with the superscript asterisk indicating the value is a predicted value.

$$ {}^{*n+1}\rho_I^{\beta} = {}^{n}\rho_I^{\beta} + {}^{n}\dot{\rho}_I^{\beta}\Delta t \tag{7.24} $$

$$ {}^{*n+1}\rho_D^{\beta} = {}^{n}\rho_D^{\beta} + {}^{n}\dot{\rho}_D^{\beta}\Delta t \tag{7.25} $$

Next the dislocation velocity is updated using the analytical solution found in (Krasnikov, Mayer and Yalovets, 2011):

$$ {}^{n+1}V_D^{\beta} = {}^{n}V_D^{\beta}\exp\left(-\frac{B\cdot\Delta t}{m_0}\right) + c_t\cdot\frac{\left(F_D^{\beta} \pm b\,{}^{n}Y/2\right)}{\sqrt{B^2\cdot c_t^2 + \left(F_D^{\beta} \pm b\,{}^{n}Y/2\right)^2}}\cdot\left[1-\exp\left(-\frac{B\cdot\Delta t}{m_0}\right)\right] \tag{7.26} $$

The predicted rate of immobilisation at the next time instant is now calculated using the results of (7.24), (7.25) and (7.26).

$$ {}^{*n+1}Q_I^{\beta} = V_I\left({}^{*n+1}\rho_D^{\beta} - \rho_0\right)\sqrt{{}^{*n+1}\rho_I^{\beta}} \tag{7.27} $$

And the rate of generation of new mobile dislocations:

$$ {}^{*n+1}Q_D^\beta = k_g b \left[\frac{2B\left({}^{n+1}V_D^\beta\right)^2}{\sqrt{1-\left(\frac{{}^{n+1}V_D^\beta}{c_t}\right)^2}} + b\,{}^{*n+1}Y\left|{}^{n+1}V_D^\beta\right| \right] {}^{*n+1}\rho_D^\beta \tag{2.28} $$

Now the predicted rates of change of dislocation densities are determined:

$$ {}^{*n+1}\dot{\rho}_I^\beta = {}^{*n+1}Q_I^\beta - k_a b\left|{}^{n+1}V_D^\beta\right| {}^{*n+1}\rho_D^\beta\, {}^{*n+1}\rho_I^\beta \tag{7.29} $$

$$ {}^{*n+1}\dot{\rho}_D^\beta = {}^{*n+1}Q_D^\beta - {}^{*n+1}Q_I^\beta - k_a b\left|{}^{n+1}V_D^\beta\right| {}^{*n+1}\rho_D^\beta \left(2\,{}^{*n+1}\rho_D^\beta + {}^{*n+1}\rho_I^\beta\right) \tag{7.30} $$

The final values of the dislocations densities at the next time step are now determined using a centred difference approach applied to the rates of change calculated at the current time step and the predicted rate at the next time step:

$$ {}^{n+1}\rho_I^\beta = {}^{n}\rho_I^\beta + \frac{1}{2}\Delta t\left({}^{n}\dot{\rho}_I^\beta + {}^{*n+1}\dot{\rho}_I^\beta\right) \tag{7.31} $$

$$ {}^{n+1}\rho_D^\beta = {}^{n}\rho_D^\beta + \frac{1}{2}\Delta t\left({}^{n}\dot{\rho}_D^\beta + {}^{*n+1}\dot{\rho}_D^\beta\right) \tag{7.32} $$

With the dislocation densities and dislocation velocity now updated, update is made of the plastic strain rate tensor. This is achieved by summation over all slip systems, with the slip deformation tensor, determined by equation (7.13) resolving the direction of each slip system in the overall plastic strain rate tensor:

$$ {}^{n+1}\dot{\varepsilon}_{ij}^{pl} = \sum {}^{n}slpdef^{\beta}\, {}^{n+1}V_D^\beta\, {}^{n+1}\rho_D^\beta b \tag{7.33} $$

With update of the plastic strain tensor made using the implicit Euler method:

$$ {}^{n+1}\varepsilon_{ij}^{pl} = {}^{n}\varepsilon_{ij}^{pl} + {}^{n+1}\dot{\varepsilon}_{ij}^{pl}\Delta t \tag{7.34} $$

The plastic strain tensor is now updated and is used to scale the deviatoric stress to obtain the current value.

The rate of plastic deformation is now used to update the elastic deformation:

$$\overset{n+1/2}{\dot{\bar{\boldsymbol{C}}}}_e = {}^{n+1/2}\bar{\boldsymbol{C}}_e \left[{}^{n+1/2}\bar{\boldsymbol{d}} - {}^{n+1/2}\bar{\boldsymbol{d}}_p \right] \tag{7.35}$$

$${}^{n+1/2}\bar{\boldsymbol{C}}_e = {}^{n}\bar{\boldsymbol{C}}_e + \frac{1}{2} {}^{n+1/2}\bar{\boldsymbol{C}}_e \left[{}^{n+1/2}\bar{\boldsymbol{d}} - {}^{n+1/2}\bar{\boldsymbol{d}}_p \right]^{n+1/2} \Delta t \tag{7.36}$$

Finally, the deviatoric parts of the second Piola Kirchhoff and Mandel stresses are found:

$$\begin{aligned} \overset{n+1/2}{\dot{\bar{\boldsymbol{S}}}} &= \bar{\mathbb{C}} : \left[{}^{n+1/2}\bar{\boldsymbol{C}}_e \left({}^{n+1/2}\bar{\boldsymbol{d}} - {}^{n+1/2}\bar{\boldsymbol{d}}_p \right) \right] \\ &= \bar{\mathbb{C}} : \left[{}^{n}\bar{\boldsymbol{C}}_e + \frac{1}{2} {}^{n+1/2}\bar{\boldsymbol{C}}_e \left[{}^{n+1/2}\bar{\boldsymbol{d}} - {}^{n+1/2}\bar{\boldsymbol{d}}_p \right] \right] \left({}^{n+1/2}\bar{\boldsymbol{d}} - {}^{n+1/2}\bar{\boldsymbol{d}}_p \right)^{n+1/2} \Delta t \end{aligned} \tag{7.37}$$

$$\begin{aligned} {}^{n+1/2}\dot{\bar{S}}^{\tilde{D}} &= {}^{n+1/2}\dot{\bar{S}} - \frac{1}{3} \left({}^{n+1/2}\dot{\bar{S}} : \boldsymbol{\psi} \right) \boldsymbol{\psi} \\ &= \bar{\mathbb{C}} : \left[{}^{n}\bar{\mathbf{C}}_e + \frac{1}{2} {}^{n+1/2}\bar{\mathbf{C}}_e \left[{}^{n+1/2}\bar{\mathbf{d}} - {}^{n+1/2}\bar{\mathbf{d}}_p \right] \right] \left({}^{n+1/2}\bar{\mathbf{d}} - {}^{n+1/2}\bar{\mathbf{d}}_p \right)^{n+1/2} \Delta t \\ &- \frac{1}{3} \left(\bar{\mathbb{C}} : \left[{}^{n}\bar{\mathbf{C}}_e + \frac{1}{2} {}^{n+1/2}\bar{\mathbf{C}}_e \left[{}^{n+1/2}\bar{\mathbf{d}} - {}^{n+1/2}\bar{\mathbf{d}}_p \right] \right] \left({}^{n+1/2}\bar{\mathbf{d}} - {}^{n+1/2}\bar{\mathbf{d}}_p \right)^{n+1/2} \Delta t : \boldsymbol{\psi} \right) \boldsymbol{\psi} \end{aligned} \tag{7.38}$$

By combining the results from equations (7.37) and (7.38), this results in the updated deviatoric Piola Kirchhoff stress at the end of the time step as:

$${}^{n+1}\bar{\boldsymbol{S}}^{\tilde{D}} = {}^{n}\bar{\boldsymbol{S}}^{\tilde{D}} + \overset{n+1/2}{\dot{\bar{\boldsymbol{S}}}}^{\tilde{D}} {}^{n+1/2}\Delta t \tag{7.39}$$

The deviatoric stress update is now complete. The stress update is completed by the pressure update, which is determined from the equation of state.

7.2.2 Update of the pressure by the Gruneisen equation of state

In order to update the pressure, and therefore complete the stress update in to the current configuration, the internal energy, which is stored in the DYNA3D code, must first be calculated. The internal energy stored by DYNA3D, e, differs from the internal energy used in the development of the model, u, as the stored energy is divided by the initial volume, whereas the internal energy used in the

model development is given per unit volume. The two values are related by (Djordjevic, 2011):

$$\rho\dot{u} = \frac{1}{v}\dot{e} \tag{7.40}$$

The rate of change of internal energy is now given as:

$$\dot{e} = v\bar{\boldsymbol{\Sigma}} : \bar{\boldsymbol{d}}_e \tag{7.41}$$

Which has made use of the definition of u given in (Djordjevic, 2011).

As with other internal variables, the update is calculated by solving equation (7.41) using the central difference algorithm:

$$^{n+1}e = {}^{n}e + {}^{n+\frac{1}{2}}v\,{}^{n+\frac{1}{2}}\bar{\boldsymbol{\Sigma}} : {}^{n+\frac{1}{2}}\bar{\boldsymbol{d}}_e\,{}^{n+\frac{1}{2}}\Delta t \tag{7.42}$$

Expansion of (7.42) by inclusion of the decomposition of the stress, as is outlined in section 3.10 results:

$$\begin{aligned} ^{n+1}e = {}^{n}e &+ {}^{n+\frac{1}{2}}v\,{}^{n+\frac{1}{2}}\bar{\boldsymbol{C}}_e\,{}^{n+\frac{1}{2}}\bar{\boldsymbol{S}}^{\tilde{D}} : {}^{n+\frac{1}{2}}\bar{\boldsymbol{d}}_e\,{}^{n+\frac{1}{2}}\Delta t \\ &- {}^{n+\frac{1}{2}}v\,{}^{n+\frac{1}{2}}\bar{P}\,{}^{n+\frac{1}{2}}\bar{\boldsymbol{C}}_e\boldsymbol{\psi} : {}^{n+\frac{1}{2}}\bar{\boldsymbol{d}}_e\,{}^{n+\frac{1}{2}}\Delta t \end{aligned} \tag{7.43}$$

The pressure term is now written in terms of the pressure at the beginning and end of the time step by application of the central difference algorithm to ${}^{n+1/2}\tilde{\bar{P}}$, and the internal energy is modified slightly to account for an artificial viscosity that is used in DYNA3D, resulting in the trial value of internal energy:

$$\begin{aligned} &{}^{*}{}^{n+1}e = \\ &{}^{n}e + \left(\begin{array}{l} {}^{n+\frac{1}{2}}v\,{}^{n+\frac{1}{2}}\bar{\boldsymbol{C}}_e\,{}^{n+\frac{1}{2}}\bar{\boldsymbol{S}}^{\tilde{D}} : {}^{n+\frac{1}{2}}\bar{\boldsymbol{d}}_e \\ -\frac{1}{2}\,{}^{n+\frac{1}{2}}v\,{}^{n}\bar{P}\,{}^{n+\frac{1}{2}}\bar{\boldsymbol{C}}_e\boldsymbol{\psi} : {}^{n+\frac{1}{2}}\bar{\boldsymbol{d}}_e\,{}^{n+\frac{1}{2}}\Delta t - {}^{n+\frac{1}{2}}q\,{}^{n+\frac{1}{2}}\dot{v} \end{array} \right)^{n+\frac{1}{2}}\Delta t \end{aligned} \tag{7.44}$$

With e given at the end of the time step as:

$$^{n+1}e = {}^{*}{}^{n+1}e - \frac{1}{2}\,{}^{n+\frac{1}{2}}\bar{\boldsymbol{C}}_e\,{}^{n+1}\bar{P}\boldsymbol{\psi} : {}^{n+\frac{1}{2}}\bar{\boldsymbol{d}}_e\,{}^{n+\frac{1}{2}}v\,{}^{n+\frac{1}{2}}\Delta t \tag{7.45}$$

The internal energy that is stored in DYNA3D is updated by:

$$^{n+1}E = \frac{^{n+1}e}{v_0} \tag{7.46}$$

The updated internal energy is now used to calculate the update of pressure which is given by:

$$^{n+1}\bar{P} = {}^{n+1}A + {}^{n+1}B\,{}^{n+1}E \tag{7.47}$$

Where ^{n+1}A and ^{n+1}B are determined by loading type. Substitution of (7.45) into (7.47) leads to:

$$^{n+1}\bar{P}\left(1 + \frac{^{n+\frac{1}{2}}v}{2v_0}\,{}^{n+1}B\,{}^{n+\frac{1}{2}}\bar{\boldsymbol{C}}_e\boldsymbol{\psi} : {}^{n+\frac{1}{2}}\bar{\boldsymbol{d}}_e\,{}^{n+\frac{1}{2}}\Delta t\right) = {}^{n+1}A + {}^{n+1}B\frac{^{*n+1}e}{v_0} \tag{7.48}$$

Which gives the pressure update in terms of the trial value of the specific internal energy as:

$$^{n+1}\bar{P}_{EOS} = \frac{^{n+1}A + {}^{n+1}B\,{}^{*n+1}E}{1 + \frac{^{n+\frac{1}{2}}v}{2v_0}\,{}^{n+1}B\,{}^{n+\frac{1}{2}}\bar{\boldsymbol{C}}_e\boldsymbol{\psi} : {}^{n+\frac{1}{2}}\bar{\boldsymbol{d}}_e\,{}^{n+\frac{1}{2}}v\,{}^{n+\frac{1}{2}}\Delta t} \tag{7.49}$$

The pressure update now completes the internal energy update given in equation (7.45). With the pressure update calculated, and the deviatoric update from before, the full Mandel stress tensor can be updated, and therefore pushed forward into the current configuration resulting in $^{n+1}\boldsymbol{\tau}$:

$$^{n+1}\bar{\boldsymbol{\Sigma}} = {}^{n+1}\bar{\boldsymbol{C}}_e\,{}^{n+1}\bar{\boldsymbol{S}}^{\tilde{D}} + {}^{n+1}\bar{P}\,{}^{n+1}\bar{\boldsymbol{C}}_e\boldsymbol{\psi} \tag{7.50}$$

$$^{n+1}\boldsymbol{\tau} = {}^{n+1}\bar{\boldsymbol{F}}_{ed}^{-T}\,{}^{n+1}\bar{\boldsymbol{\Sigma}}\,{}^{n+1}\bar{\boldsymbol{F}}_{ed}^{T} \tag{7.51}$$

This completes the stress update in the model.

7.3 Flowchart of subroutines of new material model in DYNA3d

This section presents a flowchart overview of the subroutines of the new material model in DYNA3d.

The flow chart presented below consists of three regions, each contained within a coloured box. The subroutines contained within the black box are the subroutines required for the input phase of the model. These subroutines have the purpose of reading in the simulation data to the main DYNA3d database. The subroutine highlighted in green is a new subroutine developed for the new material model and reads in model specific data.

The subroutines contained within the green box are the subroutine which control the initialisation phase of the simulation. As with the input subroutines, the subroutines highlighted in green are developed for the new material model. The first of these, inse224.f sets the initial values of the material model variables to zero, and the second, slpsys.f determines the slip system vectors for the structure of the material being modelled. At present this subroutine is only capable of determining the slip systems for FCC and BCC crystals.

The final set of subroutines, contained within the red box are the subroutines in the solution phase. These subroutines contain the main plasticity model and control the evolution of the model.

The subroutine in the solution phase highlighted in blue, f3dm224.f, contains the main constitutive model, and it is in this subroutine that the new dislocation dynamics based model sits. Also in the solution phase, the subroutine mat224_csq.f has been modified. This subroutine is used for time step control. Finally, the subroutines hieupd224.f and eqos224.f have been modified. These subroutines calculate the internal energy update required by the equation of state, and compete the stress update using equation of state data, respectively.

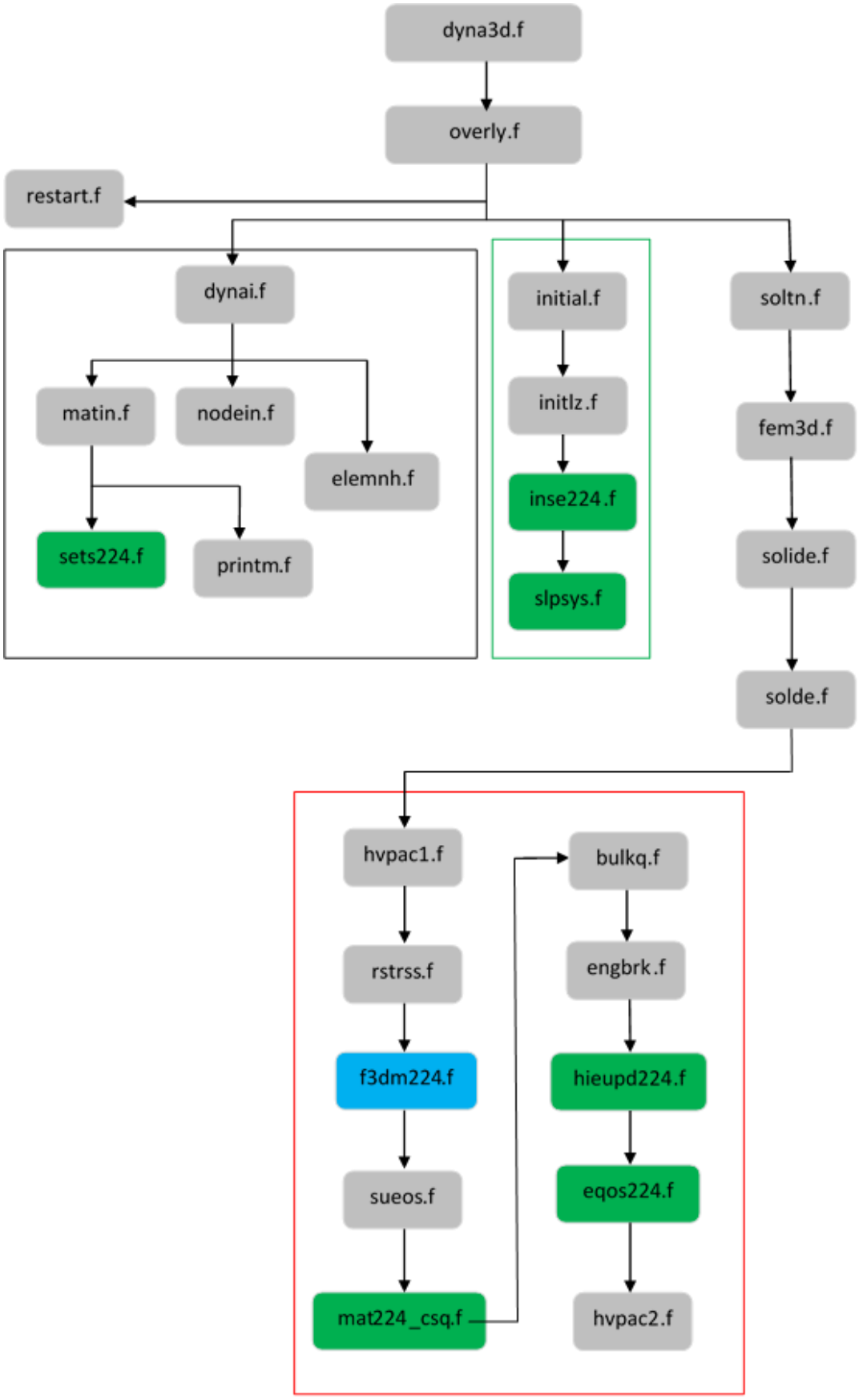
dyna3d.f
overly.f
restart.f
dynai.f
matin.f
nodein.f
elemnh.f
sets224.f
printm.f
initial.f
initlz.f
inse224.f
slpsys.f
soltn.f
fem3d.f
solide.f
solde.f
hvpac1.f
rstrss.f
f3dm224.f
sueos.f
mat224_csq.f
bulkq.f
engbrk.f
hieupd224.f
eqos224.f
hvpac2.f

7.4 Artificial viscosity

It has been discussed in chapter 4 that a shockwave propagates as a discontinuity, with jumps in pressure, density, particle velocity and energy. In order to simulate this stably, the DYNA3d hydrocode adds an artificial bulk viscosity, which effectively smear the shock front over a few element. The form of the artificial viscosity added by DYNA3d has the form :

$$q = \rho l\left(C_0 l\dot{\varepsilon}_{kk}^2 - C_l a\dot{\varepsilon}_{kk}\right) \text{ when } \dot{\varepsilon}_{kk} < 0 \qquad (2.52)$$

$$q = 0 \text{ when } \dot{\varepsilon}_{kk} > 0$$

Where q is the artificial viscosity, ρ is the mass density, $l = \sqrt[3]{v}$ where v is the volume, $\dot{\varepsilon}_{kk}$ is the strain rate, a is the local speed of sound and C_l and C_0 are dimensionless constants.

The dimensionless constants C_o and C_l are commonly referred to as the quadratic and linear constants, respectively, and have default values of 1.5 and 0.06. Effectively in simulations, the quadratic constant controls the number of elements over which the shock is smeared, and the linear term damps out noise behind the shock front. Following an analysis of the sensitivity of the new material model to artificial viscosity, see Appendix B, it is concluded that an increased value of C_l is required, with the value of 0.1 being optimal.

In addition to the increased shock viscosity values, a decreased time step scale factor of 0.1 (default =0.9) is required. This is due to the numerical methods used within the model and provides stability.

7.5 Summary

This chapter has presented an algorithmic style system of discretised equations that replicate those implemented in the DYNA3d hydrocode. For stability a decreased time step scale factor of 0.1 is required (default = 0.9).

8 Validation of the new material model for face centred cubic (fcc) metals

Following the implementation of the new material model presented in chapter 7, validation of the model is presented in this chapter. Validation has been achieved in two stages; stage one consisted of single element tests, with comparison made between the new material model and an existing, previously validated model available in DYNA3d, and stage two consisted of simulation of plate impact experiments, with comparison made between the simulations and experimental data. Finally, analysis is made of the new models ability to reproduce superelastic precursor behaviour.

8.1 Stage one validation: single element compression and tension tests

The first stage of testing is conducted using simple single element tests, whereby a single cubic solid element has been created, constrained and loaded depending on the test. The single element tests utilised in this work represent an unphysical situation, however the use of these is of benefit as, but performing the tests with the new material model and an existing, previously validated model available in DYNA3d, it is possible to verify that the stress calculated by the new material model is correct. For the sake of brevity, two identical single elements have been created, one modelled using the new material model and the second using an existing model in DYNA3d under identical conditions. The element modelled using an existing model in DYNA3d is used as a reference model for the comparison of calculated stress. The MTS model, outlined in section 2.1.4 is used as the reference model.

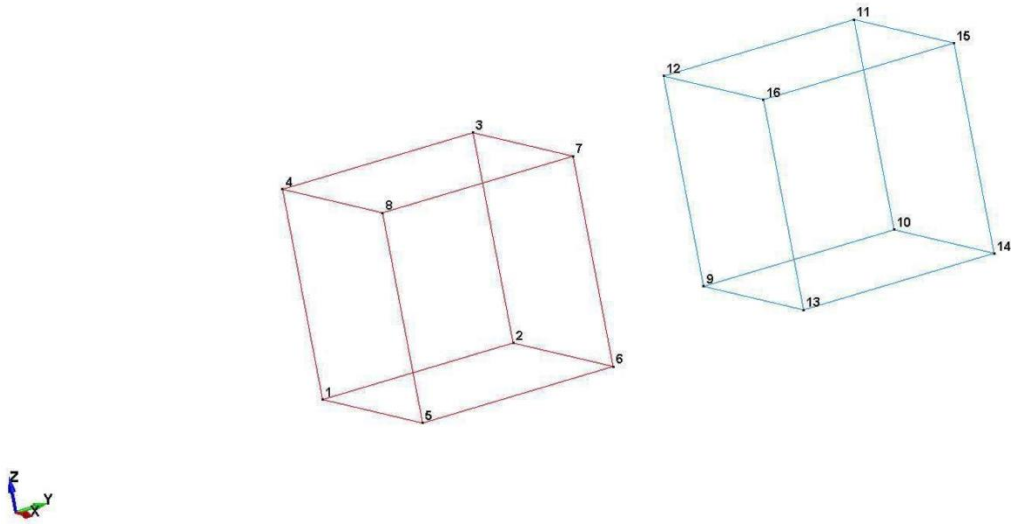

Figure 8-1: Two single elements created with the node numbers shown

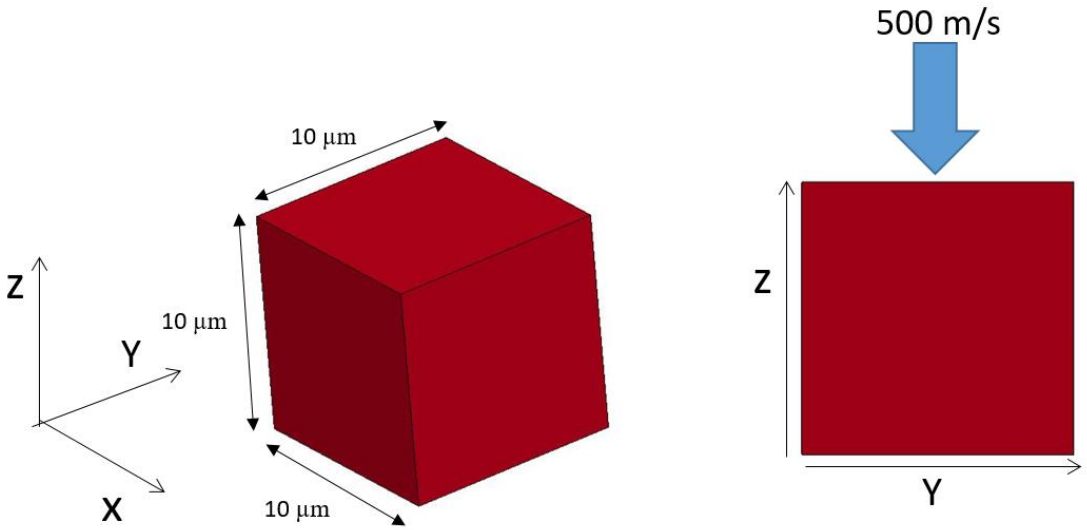

Figure 8-2: Geometry and loading condition of the single element tests

The geometry of the single elements is shown in Figure 8-2, with the applied nodal constraints outlined in Table 8-1. Loading is applied in the form of a prescribed velocity in the z-direction, to the nodes unconstrained in the z-direction. The prescribed velocity ensures that these nodes have a constant velocity throughout the test, which in turn will provide a constant strain rate. The prescribed velocity has a magnitude of 500 m/s. The direction of the velocity is reversed in separate tests to ensure both compressive and tensile loading is tested. The prescribe velocity used ensures that the strain rate observed in the

single element models is of the order of $10^7 s^{-1}$ which is typical of the strain rates observed during shock loading.

At the strain rates observed in the single element tests, the reference MTS model is performing outside of limit of applicability, however, due to the non-physical nature of these tests, and that the main purpose is to ensure the new model is calculating sensible stress levels, use of the MTS model as a reference can be justified.

Table 8-1: Nodal constraints applied to single element tests.

Nodes	Constraints for uniaxial strain
1, 2, 5, 6, 9, 10, 13, 14	x, y, z
3, 4, 7, 8, 11, 12, 15, 16	x, y

The single element tests are run using the material properties and parameters of aluminium along with the Gruneisen equation of state parameters for aluminium (Steinberg, 1996), summarised in Table 8-2.

Table 8-2: Gruneisen equation of state parameters for Aluminium (Steinberg, 1996)

Equation of state parameter	Value for Al
Velocity curve intercept, C	0.52 cm/μs
First slope coefficient, S_1	1.36
Gruneisen coefficient, γ_0	2.2
First order volume correction coefficient, a	0.48

The single element tests are performed over a time period of 0.5ns. This short time period is used to analyse the performance of the model as, at times greater

than 0.5ns, the total strain exceeds 20% which is far beyond the physically achievable value in metals.

8.1.1 Analysis of the stress histories in the single element tests

Comparison of the stress histories calculated by the new material model and the reference MTS model for the single element compression tests are made in Figure 8-3 - Figure 8-5.

Figure 8-3 and Figure 8-4, comparing the X and Y stress components, respectively, show that the values calculated by the new material model follows the values calculated by the reference MTS model, with a maximum discrepancy of 6%. Notably, it is observed that at a time of 0.0003μs (0.3ns) a kink appears in the traces of the X and Y stresses of the new material model. This kink can be explained as this is the instant in time where plastic deformation is initiated.

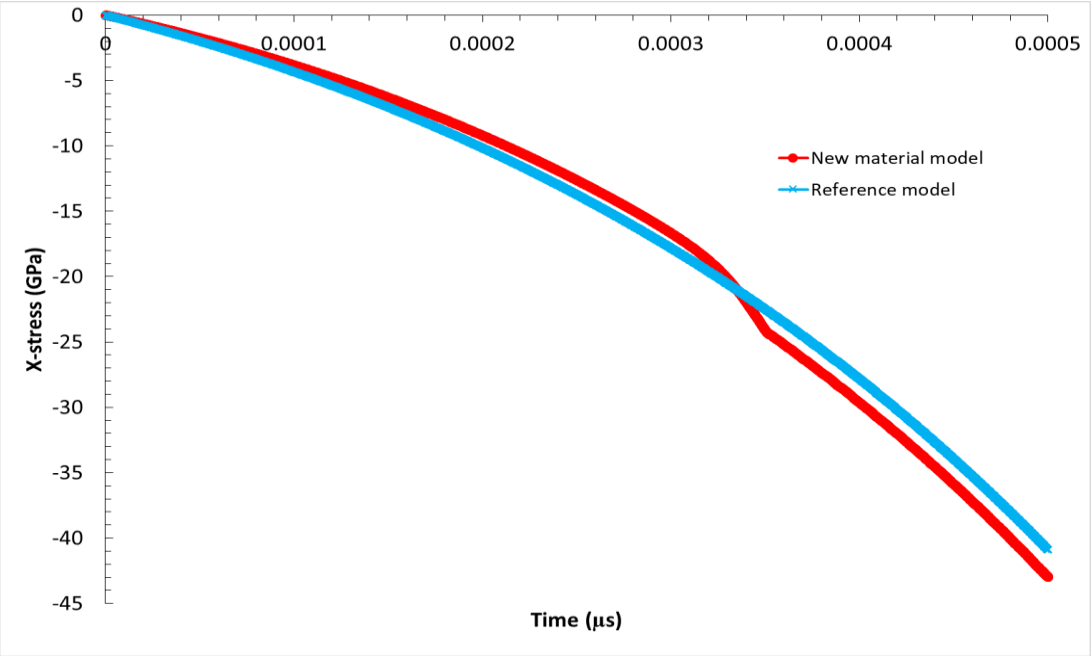

Figure 8-3: Comparison of the X-stress component history of the new material model and the reference MTS model for the single element compression test.

The z-stress history, shown in Figure 8-5, shows an over estimation of the magnitude of the z-stress obtained by the new material model when compared to

the reference MTS model, before relaxation to a value within 6% of the MTS value. This large overshoot, 25% at the most extreme, can be expected as an overshoot of the elastic stresses is a motivating factor for this work, and a feature that cannot be reproduced by existing models implemented in DYNA3d. Figure 8-6 verifies that the time instant of 0.0003μs does indeed correspond to the onset of plasticity, as it can be seen in Figure 8-6 that this is when plastic strain starts to evolve. The onset of plastic deformation relaxes the overestimated Z-stress value to a level that agrees with the reference model, within 6%.

The calculated strains shown in Figure 8-6 show that the over rate of strain appears to be constant. This is due to the conditions applied to the driven nodes in the single element tests. The nodes are driven at a constant velocity, and therefore a constant rate of strain is observed. It would be expected that the rate of strain would harden, similar to the rate of plastic strain presented in Figure 8-6, if the loading conditions were different.

Figure 8-7 - Figure 8-9 show the same stress histories obtained in the tension tests, with the same features as the compression tests being observed. In line with the compression tests, the z-stress calculated using the new material model, presented in Figure 8-9, shows an initial over estimation compared to that of the reference model, before relaxing to a level within 6% of the MTS value. Similar to the single element compression test, this overshoot behaviour can be expected as this is one of the key motivations for this work. It is seen in Figure 8-10 that the relaxation of the Z-stress corresponds to the time instant that the plastic strain begins to evolve. This confirms that the onset of plasticity provides the mechanism to relax the z-stress. The observation of this expected behaviour, along with the relaxed stress values agreeing within 6% of the MTS model confirms the first stage of validation.

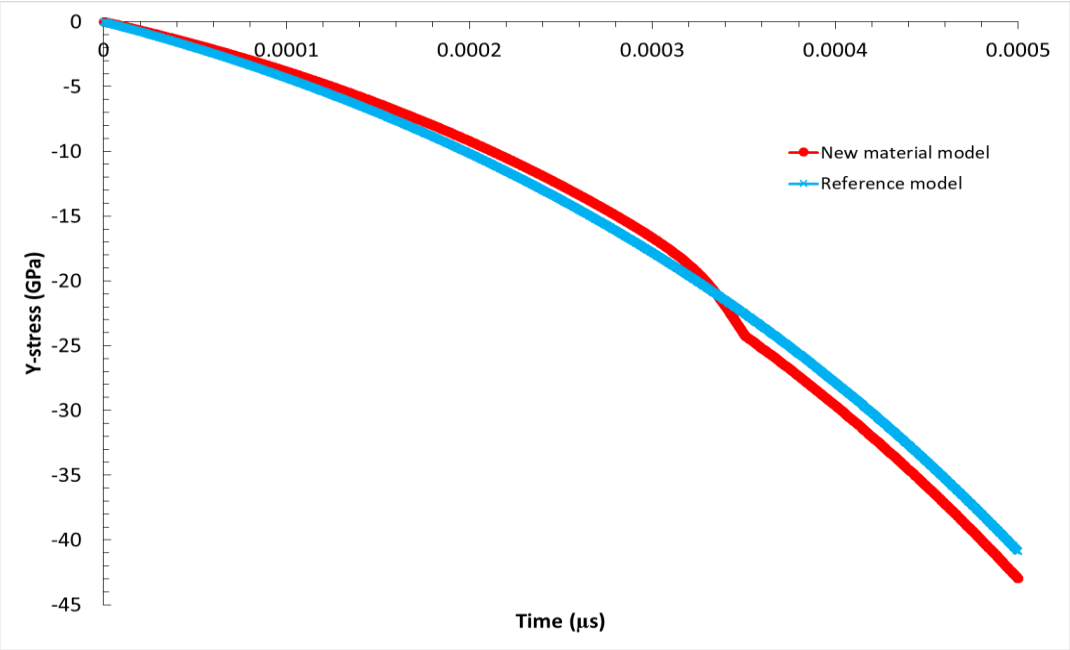

Figure 8-4: Comparison of the Y-stress component history of the new material model and the reference MTS model for the single element compression test.

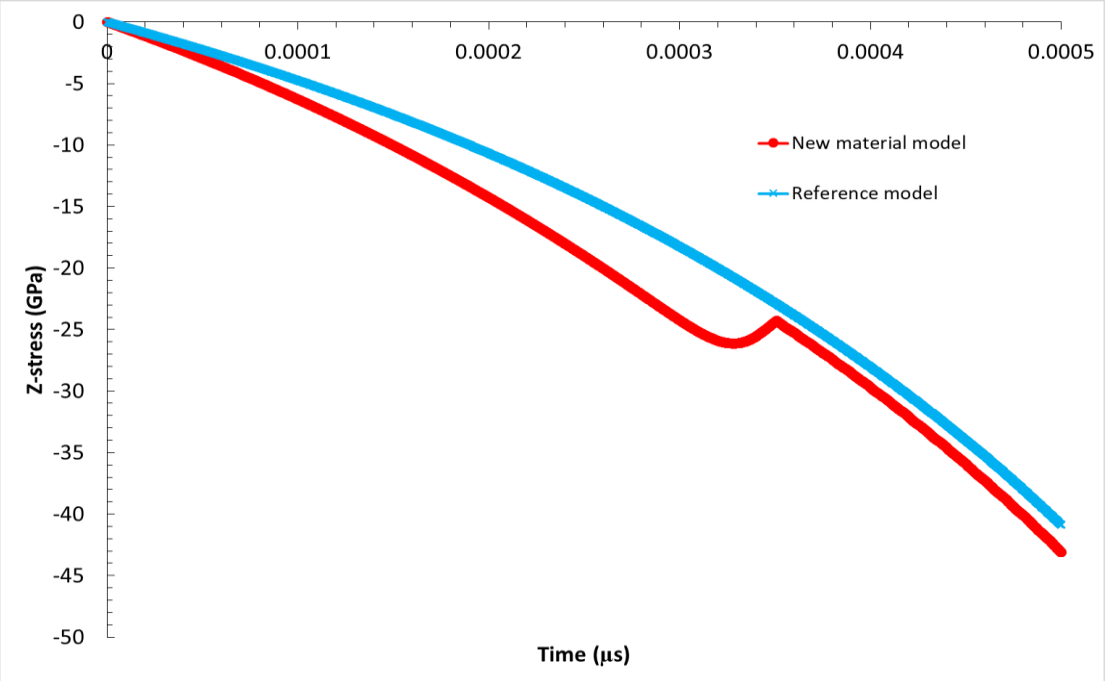

Figure 8-5: Comparison of the Z-stress component history of the new material model and the reference MTS model for the single element compression test.

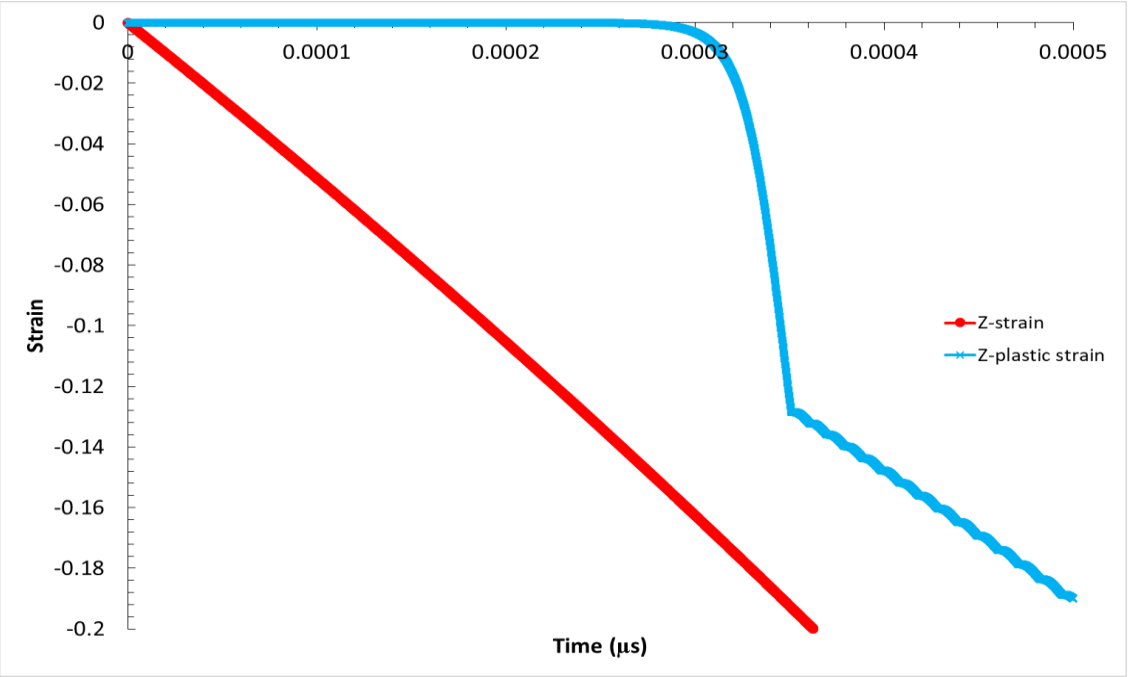

Figure 8-6: Strain and plastic strain history for the single element compression test.

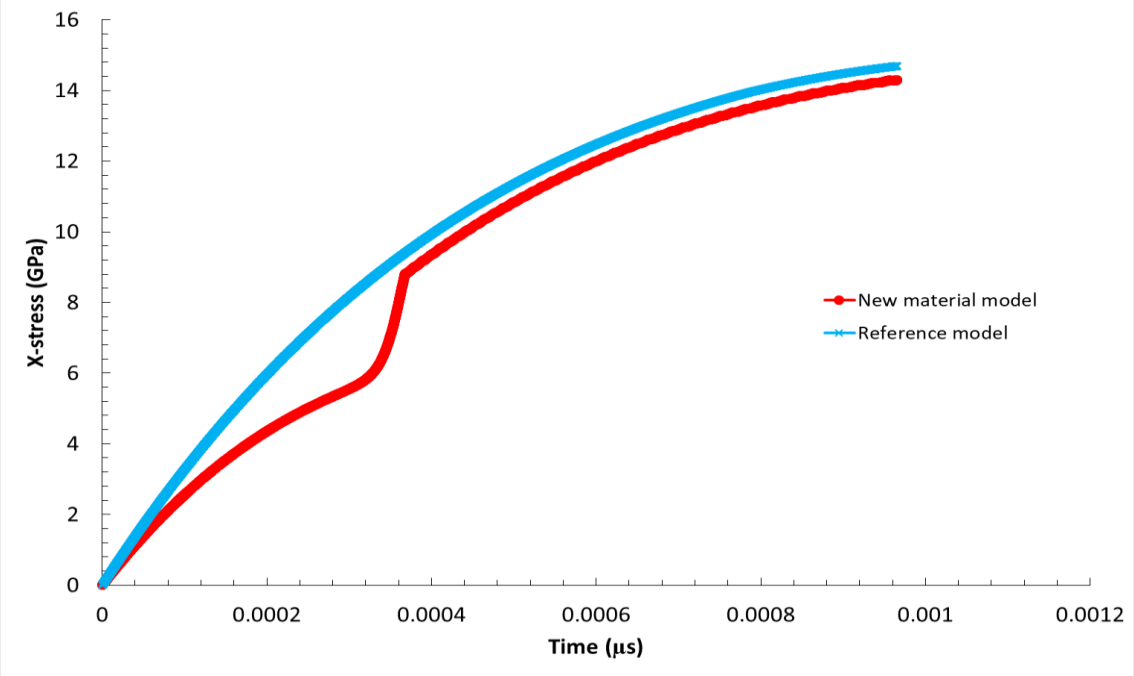

Figure 8-7: Comparison of the X-stress component history of the new material model and the reference MTS model for the single element tension test.

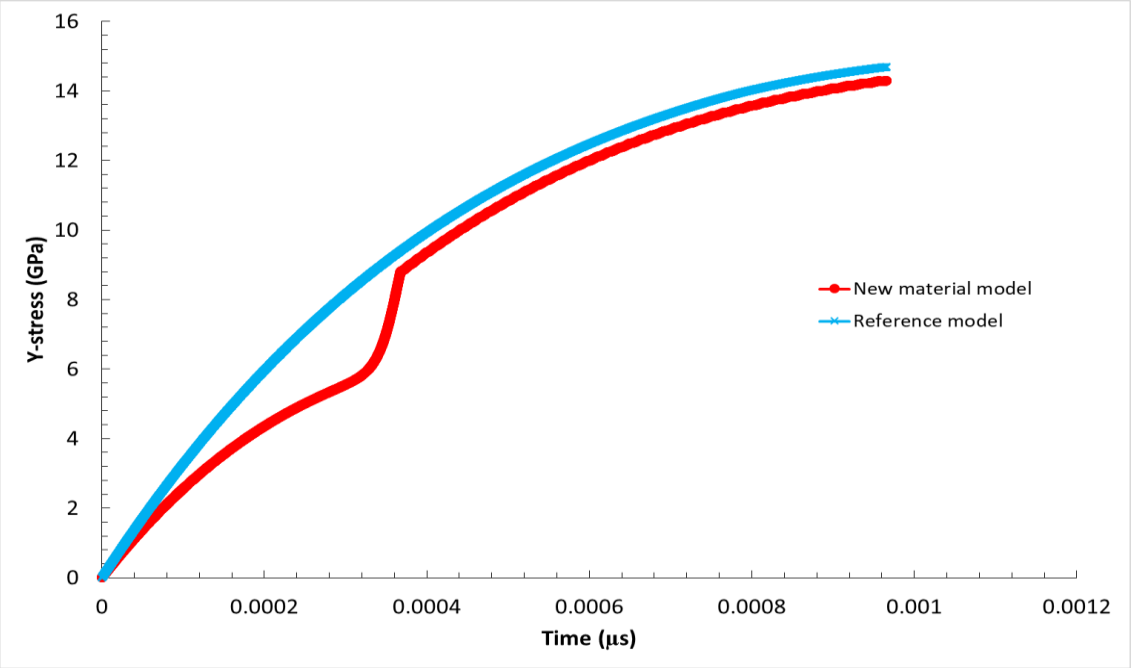

Figure 8-8: Comparison of the Y-stress component history of the new material model and the reference MTS model for the single element tension test.

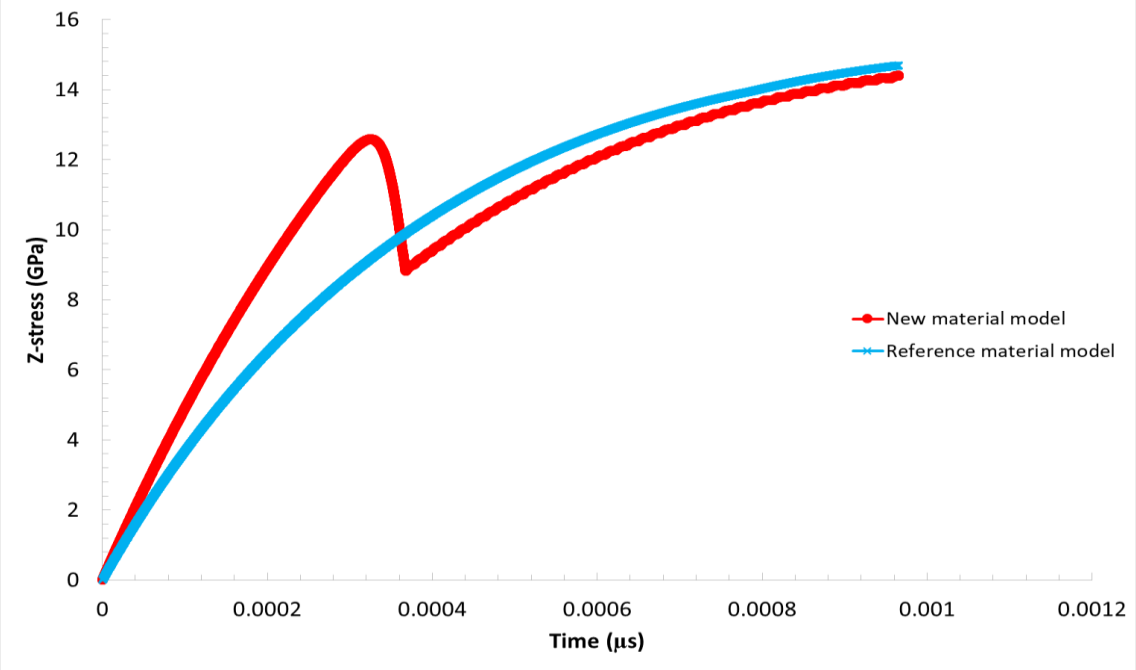

Figure 8-9: Graph showing a comparison of the z-stress calculated using the new material model and the z-stress calculated using the MTS model in the single element in tension.

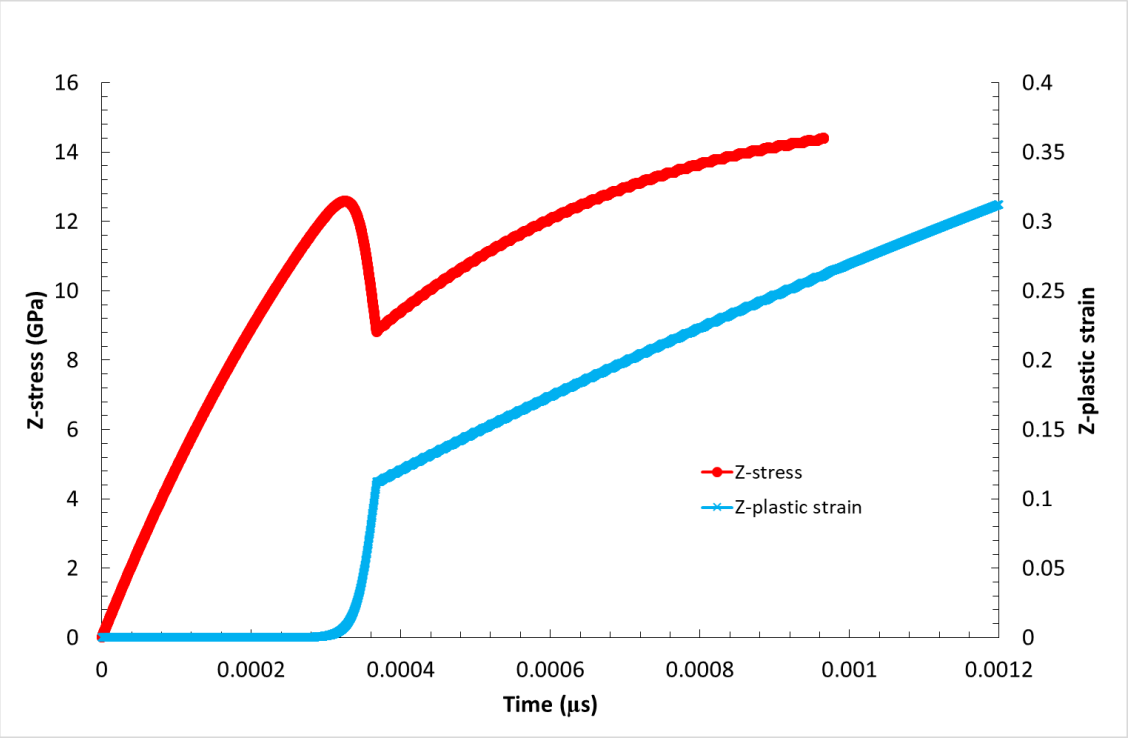

Figure 8-10: Comparison between z-stress and z-plastic strain time history for single element tension test calculated using the new material model

8.1.2 Analysis of the evolution of the dislocation based variables

Evolution of the dislocation densities are shown in Figure 8-11, Figure 8-12, Figure 8-13 and Figure 8-14 with the slip system numbering defined in Table 8-3. Due to the un-physical nature of the single element tests, and the vastly different nature of the formulation of the new model, comparison of the values of the three dislocation based state variables against experimental data or a reference model is not possible. However, analysis of these are still of significant use for ensuring the correct trends of each are observed and that the values achieved are reasonable.

Due to the geometry of the single element test, the slip systems which are perpendicular to the loading direction are expected to remain inactive throughout the duration of the single element tests. The expected inactive slip systems are the systems with planes with zero Z component, systems 3, 5, 8 and 12 in Table 8-3: Definition of the slip system numbering for fcc metals. The time histories for

the mobile and immobile dislocation densities are plotted in Figure 8-12 and Figure 8-14, respectively. It is seen in both Figure 8-12 and Figure 8-14 the values of the dislocation densities remain constant at the initial value, implying that no plastic evolution occurs on these slip systems, as expected.

The time histories of the mobile dislocation density for the remaining 8 active slip systems is shown in Figure 8-11, and the time history of the immobile dislocation densities for the 8 active slip systems in Figure 8-13. It is observed in both Figure 8-11 and Figure 8-13 that evolution of densities on each active slip system is identical. This behaviour is expected, as due to the geometry of single element tests, each of the eight active slip systems are equivalent with respect to the direction of loading.

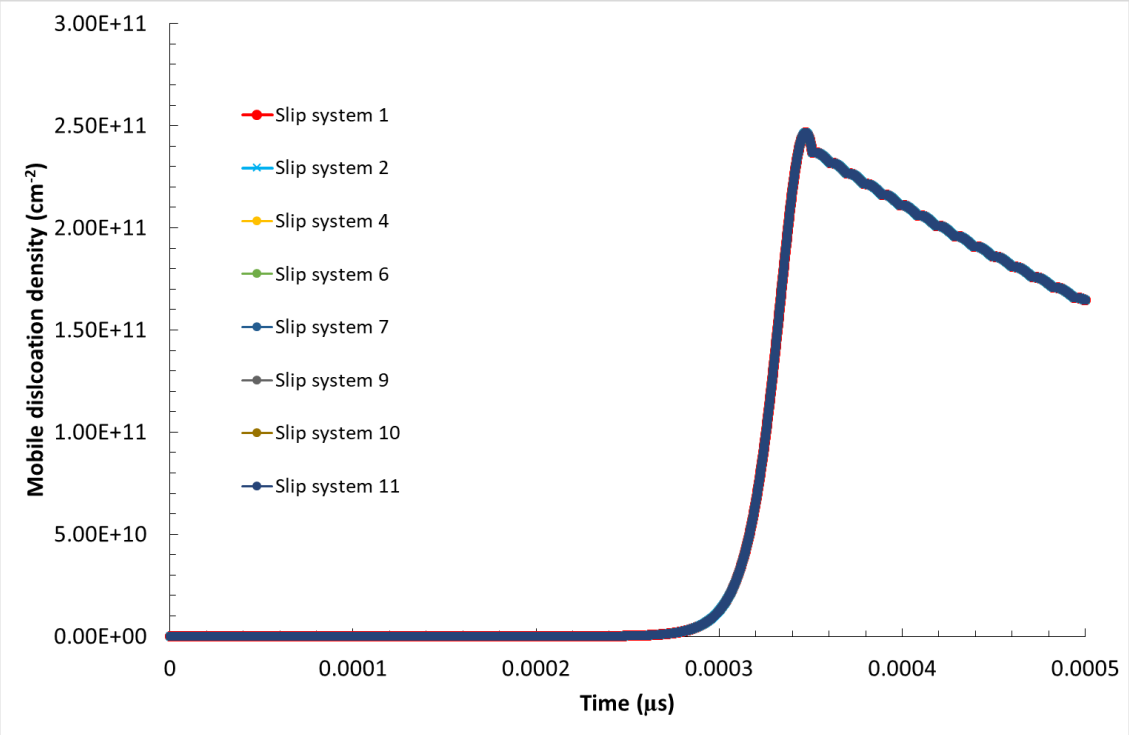

Figure 8-11: Mobile dislocation density history for the 8 active fcc slip systems in the compressed single element

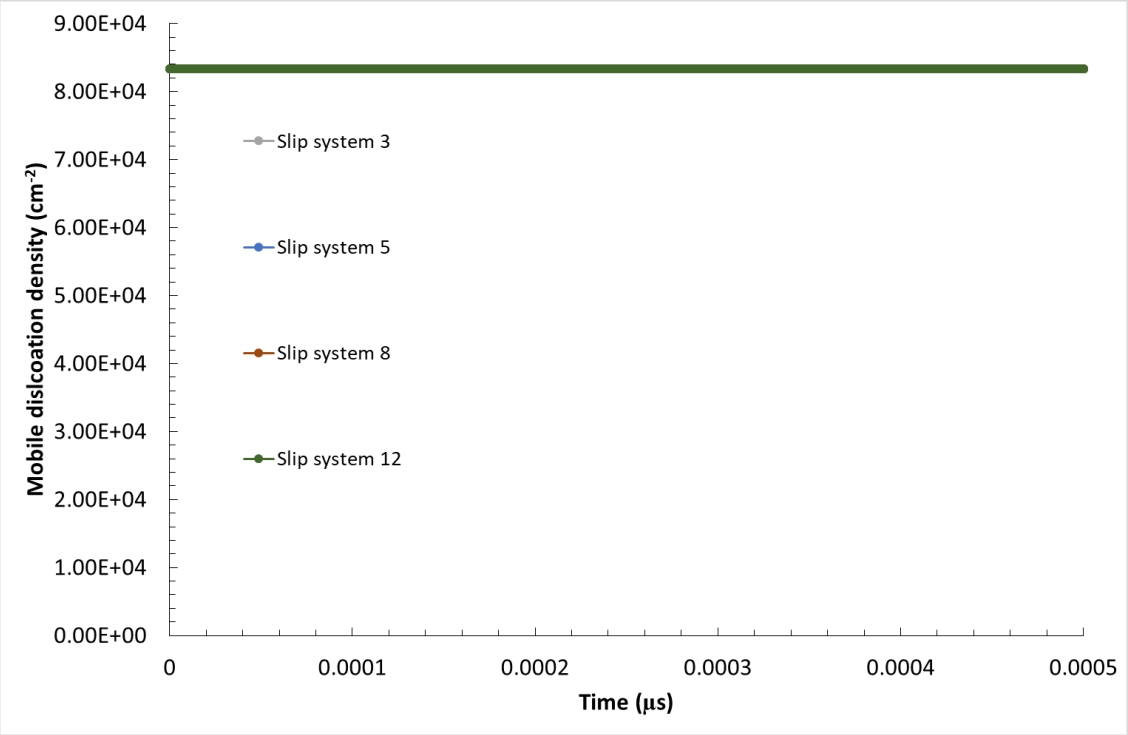

Figure 8-12: Mobile dislocation density history for the 4 inactive fcc slip systems in the compressed single element

Evolution of the mobile dislocation density, Figure 8-11, is observed to initiate with the onset of plasticity, ~0.3ns, with the value then rising sharply to a peak of $\approx 2.5\times10^{11} cm^{-2}$. In this region, the generation term in equation (6.17) is dominant, with little dislocation immobilisation or annihilation occurring. After reaching this peak value, the mobile dislocation density beings to decrease. This occurs at the same instant in time (0.3ns), seen in Figure 8-13, as the start of significant growth in the immobile dislocation density. The rise in immobile dislocation density indicates that the second term in equation (6.17) is now more significant, with strong dislocation annihilation also indicated by the order of magnitude difference between the decrease in mobile dislocation density and the rise in immobile dislocation density.

Observations of these trends verify that the model is performing as expected as these patterns and trends identified follows those outlined in section-5.13 where the multistage nature of strain hardening is discussed.

Table 8-3: Definition of the slip system numbering for fcc metals.

Slip system number	Slip system
1	$[0\bar{1}1](111)$
2	$[10\bar{1}](111)$
3	$[\bar{1}10](111)$
4	$[101](\bar{1}11)$
5	$[110](\bar{1}11)$
6	$[0\bar{1}1](\bar{1}11)$
7	$[011](1\bar{1}1)$
8	$[110](1\bar{1}1)$
9	$[10\bar{1}](1\bar{1}1)$
10	$[011](11\bar{1})$
11	$[101](11\bar{1})$
12	$[\bar{1}10](11\bar{1})$

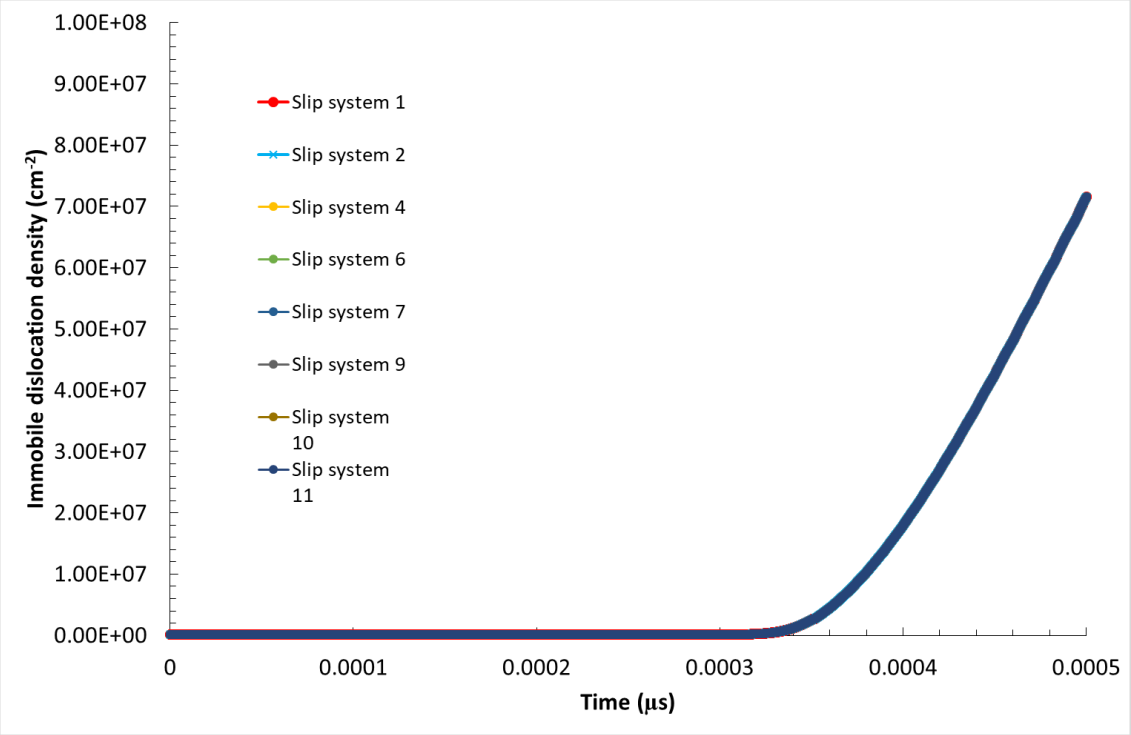

Figure 8-13: Immobile dislocation density history for the 8 active fcc slip systems in the compressed single element

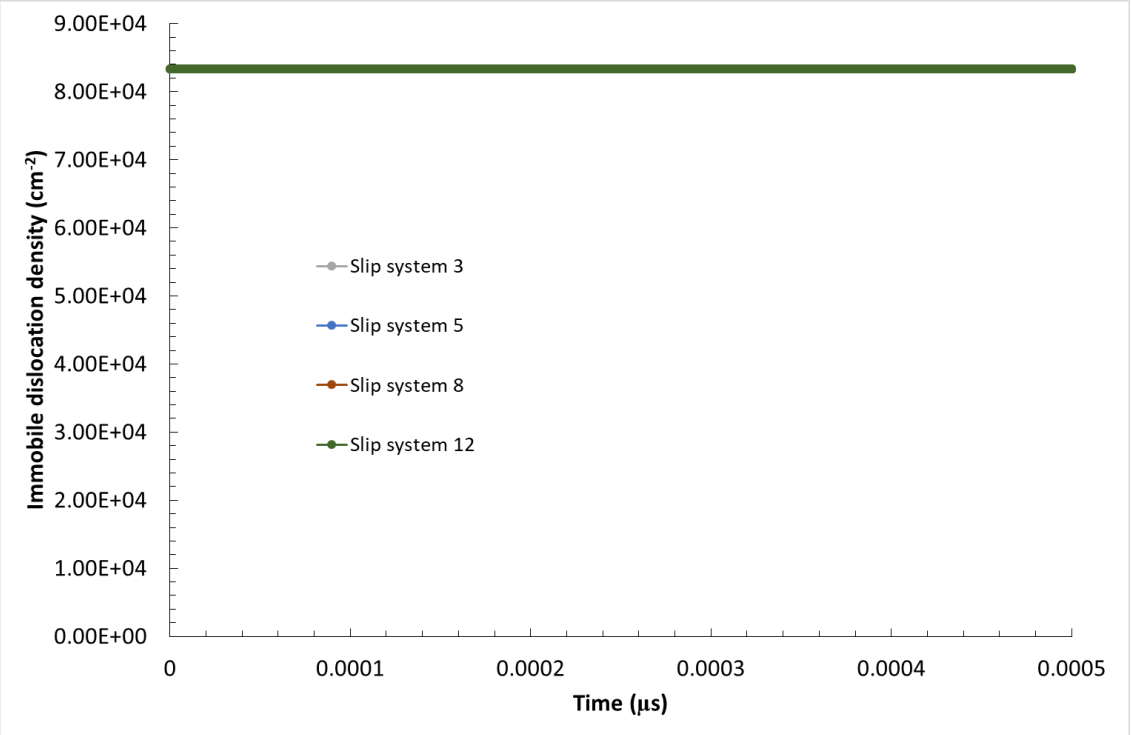

Figure 8-14: Immobile dislocation density history for the 4 inactive fcc slip systems in the compressed single element

8.2 Insight into plate impact tests

The plate impact test is a useful method of generating shocks in materials in a laboratory. The plate impact test typically consists of a flyer plate attached to a projectile, called a sabot, being fired from a gas gun towards a stationary target plate. The plates are normally aligned so that the impacting faces are perfectly parallel at impact. Upon impact, providing the velocity of the flyer plate is suitably high, both the target plate and the flyer undergo deformation in the uniaxial strain regime, with the presence of shock waves. The typical plate impact experimental set up is shown in Figure 8-15 where target plate is impacted by a flyer plate attached to a sabot and fired from a gas gun. The instrumentation typically used to measure the acceleration of the flyer plate upon impact is termed Velocity interferometer system for any reflector (VISAR) which uses laser interferometry to measure velocity. Plate impact data used within this work is obtained in this way with a sampling rate of $10^{11}s^{-1}$ with an accuracy of ±1m/s.

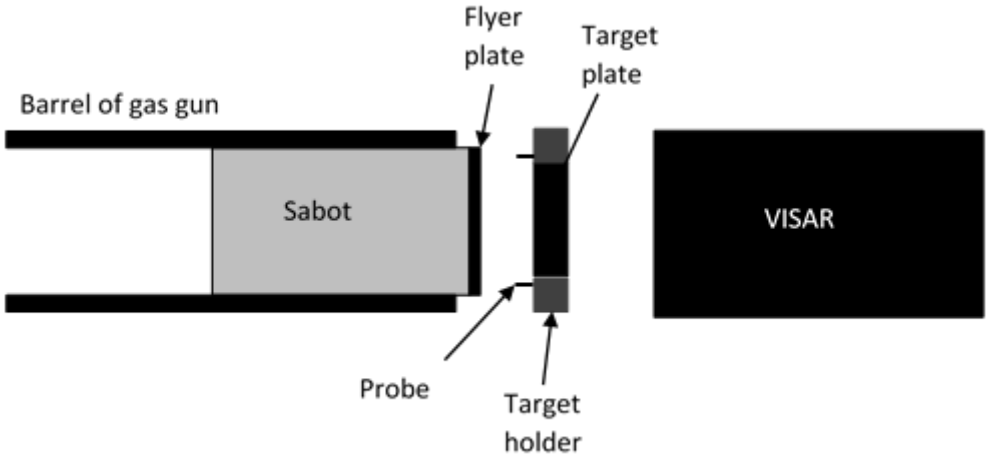

Figure 8-15: Schematic diagram of a typical plate impact test, consisting of a flyer plate fired from a gas gun into a target plate, with the rear surface velocity of the target measured using VISAR.

A key property of the plate impact test is the geometry of both the flyer and target plates. To ensure a state of uniaxial strain is maintained during the time of propagation of the shock, the thickness of the plates must be small in comparison to the dimensions of the plate perpendicular to the direction of impact. This ensures that release waves from the edges of the plate do not reach the central cross section of the plate, from which the shock response is measured.

When simulating plate impact tests, only the central cross section of the plates are simulated, with symmetry boundary conditions applied along the faces along the direction of impact. Application of these conditions ensures accurate representation of the relatively large dimensions of the plates is achieved. Setting the simulation up in this manner ensures a state of uniaxial strain is maintained throughout, which is a reasonable approximation over the time scales of interest.

A typical measurable output of a plate impact experiment is the particle velocity at the rear surface of the target plate. Figure 8-16 shows an idealised rear surface velocity plot, displaying the main features observed experimentally.

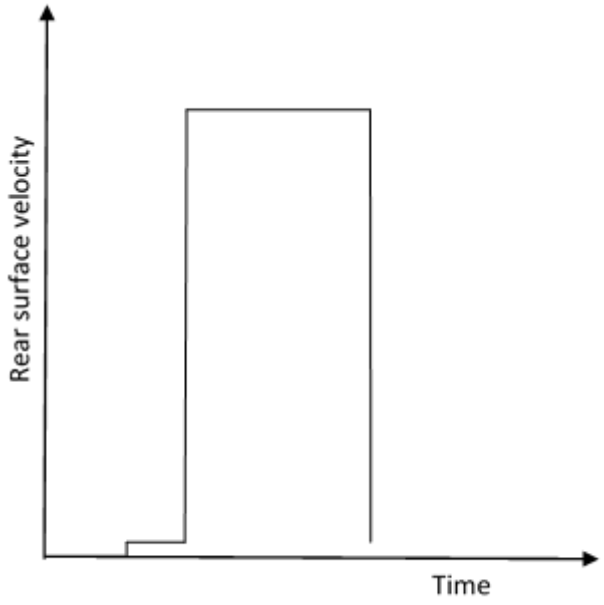

Figure 8-16: Idealised rear surface velocity plot

It is seen in Figure 8-16 that two accelerations of the rear surface occur. Firstly, a small acceleration is observed, which coincides with the precursor wave arriving at the rear surface. This is followed by a steep jump in the velocity, which is caused by the main shock front arriving at the rear surface. Finally a decrease in the velocity is observed due to the release wave.

The main features of the rear surface velocity plot are controlled by the material properties, the impact velocity and the geometry of the plates. Firstly, the width of the precursor pulse is controlled by the difference in velocities of the elastic wave and the main shock front. In the case of strong shocks, this difference will be minimal, and the precursor response may not always be observed. The width of the main shock pulse is typically controlled by the flyer plate thickness. The duration of this pulse is typically twice the time taken for the shock in the flyer plate to reach the rear surface of the flyer. Reflection of this shock from the rear surface of the flyer results in the release wave propagating first through the flyer and then the target plate. The amplitude of the rear surface velocity is determined by the impact velocity of the flyer plate.

It should be noted that experimentally additional spall pulses will be observed after the release , however analysis of these are omitted from this work due to

this typically being accepted as the region in which damage is initiated, which is currently not included in the developed material model.

Validation of the material model is made by comparison of simulation data against experimental rear surface velocity data for aluminium and copper, with rear surface data available for single crystal tantalum used when investigating the application of the model to bcc material.

8.3 Simulation of plate impact tests using the new material model

The second stage of model validation was performed by simulation of plate impact tests, with comparison made to experimental data obtained in a similar fashion to the experimental techniques outlined in the previous section.

Plate impact simulations were performed for two materials; single crystal aluminium and single crystal copper, both of which have an fcc structure. The mesh computational mesh generated consisted of a single continuous mesh divided into two regions; a target plate region and a flyer region. The nodes in the flyer plate section of the mesh were assigned an initial velocity equal to the flyer plate impact velocity of the corresponding experimental data, while the nodes in the target region have an initial velocity of zero.

The aluminium plate impact test consisted of a 2.9mm target plate, impacted by a 0.4mm target plate at a velocity of 660 m/s. The mesh generated to model this consisted of a single continuous mesh divided into two regions; a flyer region, with the nodes assigned an initial velocity of 660m/s in the z-direction, and a target region, with the nodes initially stationary. The mesh was generated in this way to eliminate the need of a contact algorithm. Figure 8-17 shows a schematic diagram of the mesh generated.

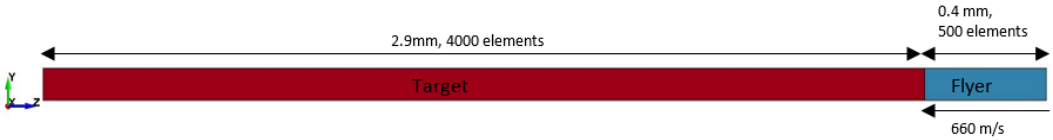

Figure 8-17: Diagram of the computational model generated for modelling single crystal aluminium plate impact test. The x and y dimensions are not to scale here and have been expanded for clarity.

Impact is made along the z-direction, with the material coordinate system aligned with the global coordinate system. This results in the single crystal effectively being impacted along the [001] crystal direction. Following mesh density studies, detailed in Appendix A, 4000 elements are used along the z-direction of the target plate, corresponding to an element size of 0.725μm. To ensure the conditions for uniaxial strain are met, symmetry planes are applied along the faces perpendicular to the impact faces.

Similarly, the copper plate impact simulations are set up in the same way, with only the dimensions and impact velocity different to match experimental values. Two copper plate impact tests are simulated, firstly a 0.7mm thick copper target is impacted by a 0.2mm thick aluminium flyer at a flyer velocity of 560m/s, and the second test having a 4.2mm thick copper target impacted by a 0.4mm thick aluminium flyer at 660m/s. The same mesh density is used as in the aluminium plate impact tests. Full data samples are taken every 5ns for the aluminium plate impact test and both the copper plate impact tests.

The material model parameters used for modelling both single crystal aluminium and single crystal copper are summarised in Table 8-4, with the values taken from (Mayer, et al., 2013), and the equation of state input parameters, available in (Steinberg, 1996) shown in Table 8-5.

Table 8-4: Material model parameters for aluminium and copper (Mayer, et al., 2013).

Model parameter	Parameter Definition	Aluminium	Copper	Equation parameter required for
E	Young's Modulus	62.4 GPa	117 GPa	
G	Shear modulus	24 GPa	47.7 GPa	
μ	Poissons ratio	0.34	0.337	
ρ_0	Dislocation immobilisation threshold	10^7 cm^{-2}	10^7 cm^{-2}	6.21
k_g	Coefficient of generation of mobile dislocations	7.9 x 10^{19} J^{-1}	7.9 x 10^{19} J^{-1}	6.19
k_a	Coefficient of annihilation of dislocations	10	10	6.18
A_1	Hardening parameter	6	4	6.14
V_1	Characteristic velocity of dislocations during immobilisation	5 ms^{-1}	2 ms^{-1}	6.21
θ	Debye temperature	430 K	280 K	6.16
Y_0	Resistance due to Peierls barrier	22 MPa	30 MPa	6.14
m_0	Effective mass of dislocation	10^{-16} kgm^{-1}	10^{-16} kgm^{-1}	6.13
a_0	Lattice constant	4.046 Å	3.610 Å	2.1

Table 8-5: Gruneisen equation of state parameters for aluminium and copper (Steinberg, 1996).

Equation of state parameter	Aluminium	Copper
Velocity curve intercept, C	0.52 cm/μs	0.394 cm/μs
First slope coefficient, S_1	1.36	1.489
Gruneisen coefficient, γ_o	2.2	2.02
First order volume correction coefficient, a	0.48	0.47

In both the aluminium and copper plate impact test cases, the rear surface particle velocity is measured and compared to experimental data (Kanel, et al., 2001) (Kanel, et al., 1996). The results of the aluminium plate impact test is shown in Figure 8-18 and of the copper plate impact tests in Figure 8-19 and Figure 8-20.

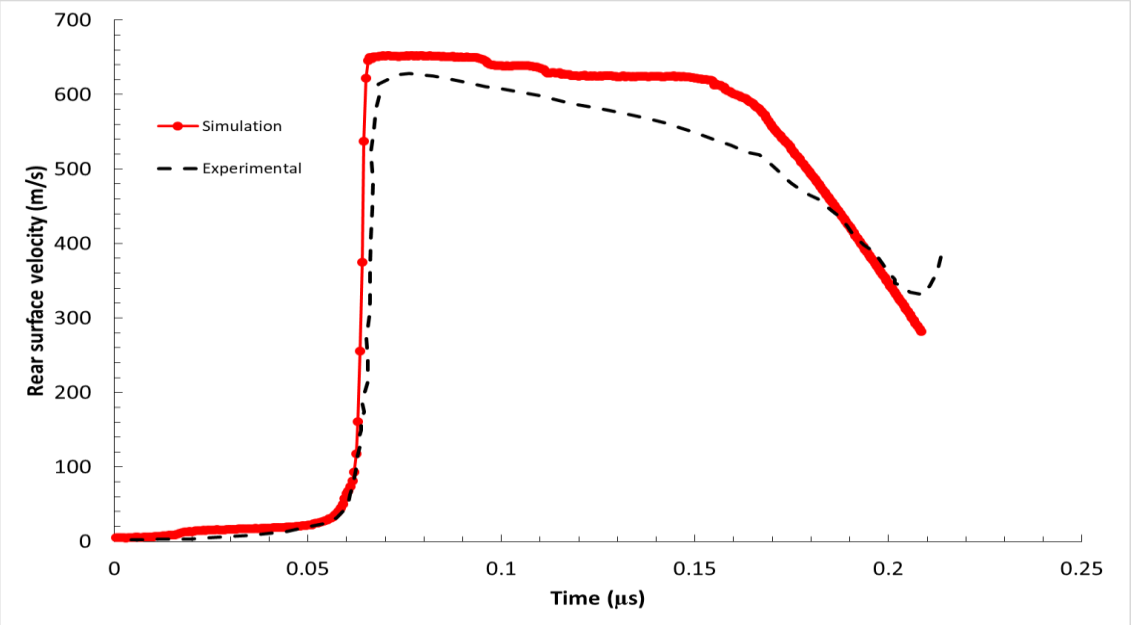

Figure 8-18: Comparison of simulation and experimental rear surface velocity data for a 2.9mm thick aluminium target impacted by a 0.4mm thick aluminium target at 660m/s. Experimental data taken from (Kanel, et al., 2001) (Mayer, et al., 2013)

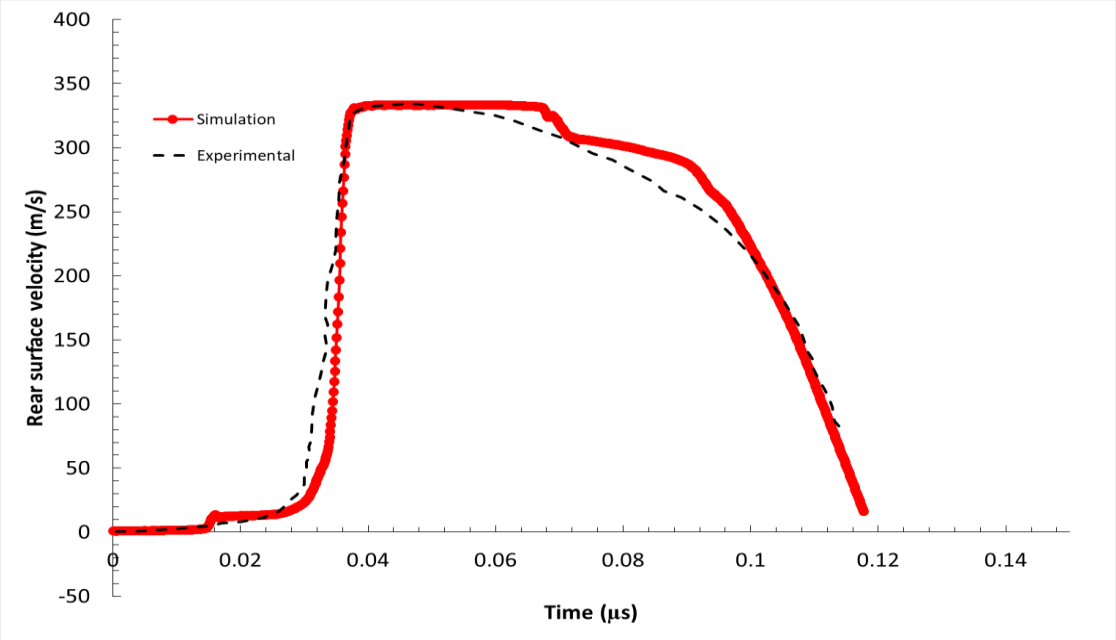

Figure 8-19: Comparison of simulation and experimental rear surface velocity data for a 0.7mm thick copper target impacted by a 0.2mm thick aluminium flyer at 560m/s. Experimental data taken from (Kanel, et al., 1996) (Mayer, et al., 2013).

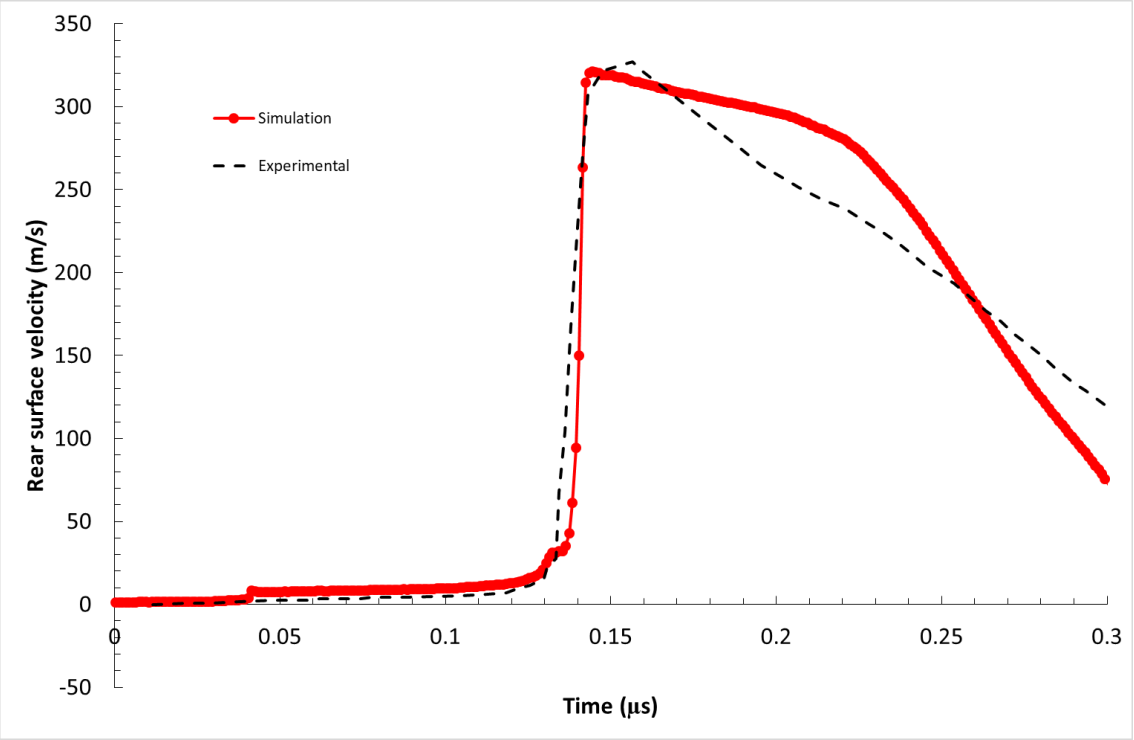

Figure 8-20: Comparison of simulation and experimental rear surface velocity data for a 4.2mm copper target plate being impacted by a 0.4mm aluminium flyer at 660m/s. Experimental data taken from (Kanel, et al., 1996) (Krasnokov, et al., 2011)

It can be seen in Figure 8-18 that the simulation over predicts the rear surface velocity by approximately 3%. This minor discrepancy could be due to a slight difference in the flyer plate impact velocity between the experimental data and the simulation set up, due to a incorrectly recorded experimental measurable.

In the case of the copper plate impact tests, shown in Figure 8-19 and Figure 8-20, the rear surface velocity predicted by the simulations show a very close agreement to the experimental data, indicating that the model captures this correctly.

Additionally, large discrepancies are observed in both the aluminium and copper plate impact tests during the unloading, or release. The simulation over-predicts the stress amplitude by approximately 14% for the aluminium plate impact and 20% for the copper plate impact at the most extreme. This behaviour is expected as the current model only accounts for plasticity and does not incorporate

damage, and it is this region of the rear surface velocity graphs that the effects of damage would be seen.

Each of Figure 8-18, Figure 8-19 and Figure 8-20 shows that the simulated data predicts a small acceleration of the rear surface due to the arrival of the precursor wave, however this is not clearly apparent in the experimental data. This could be due to the lack of clarity in the experimental curve surrounding the initial rise in velocity.

Finally, the pulse durations in both Figure 8-18 and Figure 8-19 show a very good level of agreement between the simulation data and the experimental data, with differences of less than 1% observed in both cases. This confirms the model is suitable and valid for modelling of shock induced plasticity in fcc metals.

8.4 Analysis of dislocation history variables in plate impact

One of the advantages of using a dislocation based model over a more traditional continuum model, for example the MTS model, is that additional to the output stresses and strains, details about the state of the microstructure can be obtained. Here an analysis is made of the dislocation based state variables. The analysis is made for the copper plate impact test with a 0.7mm thick target. Similar analyses have been made for the aluminium plate impact and the 4.3 mm thick target copper plate impact, but for the sake of clarity, only the 0.7mm thick copper plate impact analysis is presented here.

The analysis is carried out by analysis of the dislocation state variables, the longitudinal stress and the nodal velocity in an element 20μm from the rear surface. This element is selected as it is sufficiently far back from the rear surface for boundary effects not to have an effect.

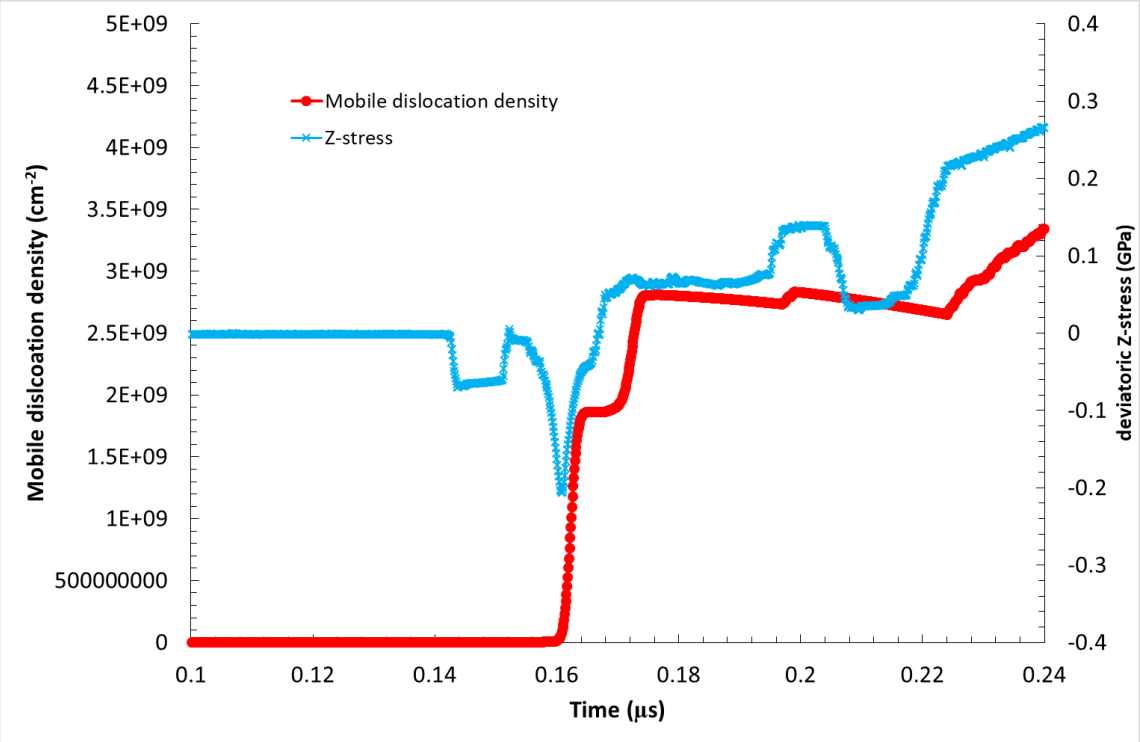

Figure 8-21: Plot showing the evolution of the mobile dislocation density in an element 20µm from the rear surface.of a 0.7mm thick copper target that is impacted by a 0.2 mm thick aluminium flayer at a velocity of 560 m/s. The deviatoric z-stress history is also plotted to aid understanding.

Analysis of the density of mobile dislocations is shown in Figure 8-21. Due to the symmetry of the slip planes relative to the loading direction, the mobile dislocation density history of only one slip system is presented. Eight slip systems have a mobile dislocation density history identical to this, with the remaining four, the four with directions perpendicular to the loading direction (i.e. [110] or [-110]) remaining constant throughout due to these being inactive.

It is seen in Figure 8-21 that the density of mobile dislocations grows significantly, from initial values of the order of 10^5 cm^{-2}, on the shock front, before remaining fairly constant behind the shock, with a slightly decreasing trend. This behaviour is explained by the fact that it is the deviatoric component of the stress that drives dislocation motion, and consequently the generation of mobile dislocations, which is seen in Figure 8-22 to have a near zero value behind the shock front. Additionally, Figure 8-22 shows that the dislocation velocity returns to zero behind

the shock front, further confirming that the mobile dislocation density should not increase in this region.

The slightly decreasing nature of the mobile dislocation density at times between 0.18 and 0.22ns can be explained by Figure 8-23. It is observed here that the density of immobile dislocations grows steadily behind the shock front, which indicates that mobile dislocations are being immobilised in this region and therefore the growth of immobile dislocations results in a decrease of mobile dislocation density.

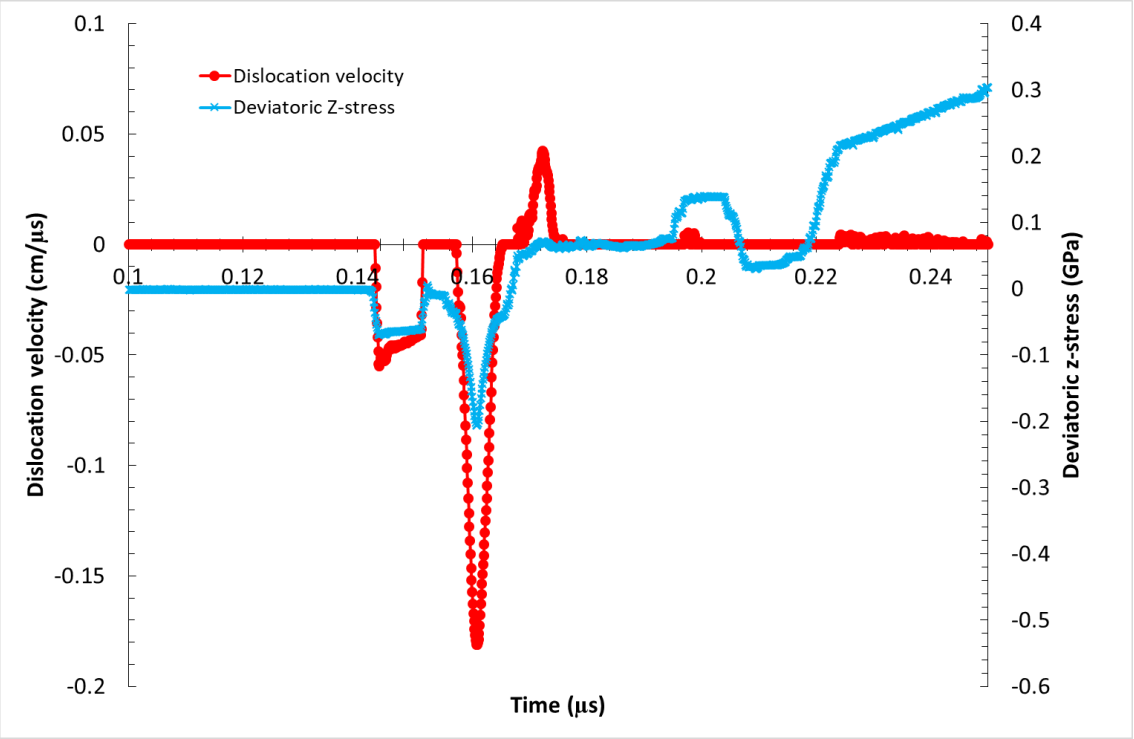

Figure 8-22: Dislocation velocity history compared to deviatoric component of z-stress in an element 20μm from the rear surface of a 0.7mm thick copper target plate that is impacted by a 0.2mm thick aluminium flyer plate at a velocity of 560 m/s.

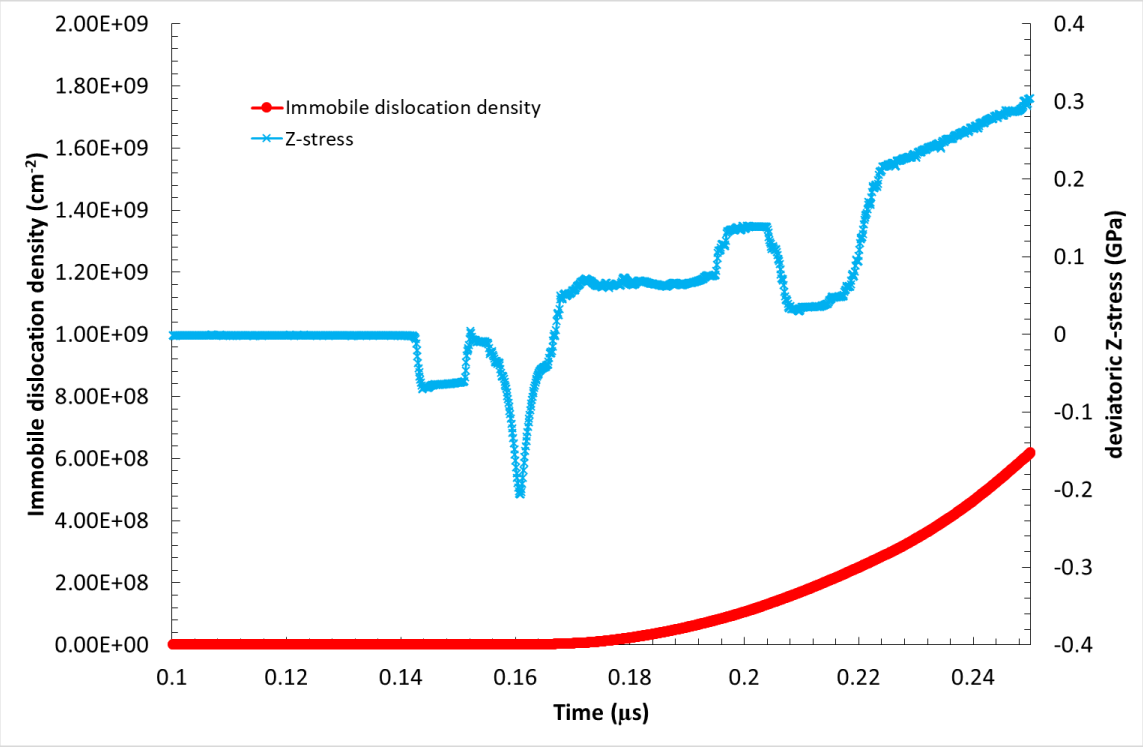

Figure 8-23: Plot showing the evolution of the immobile dislocation density in an element 20µm from the rear surface.of a 0.7mm thick copper target that is impacted by a 0.2 mm thick aluminium flayer at a velocity of 560 m/s. The deviatoric z-stress history is also plotted to aid understanding.

8.5 Investigation of precursor decay using symmetric plate impact tests

It was identified in chapter 2 that the main motivation for the development of this model was due to its ability to reproduce the initial overshoot of the amplitude of the precursor wave, with decay occurring over short (nanosecond) time scale. Investigation into the ability of the model to reproduce this behaviour when implemented in the framework of the orthotropic continuum model is assessed with the simulation of a symmetric plate impact.

The symmetric plate impact is simulated using a single, continuous computational mesh split into two regions of equal size, see Figure 8-24. Similar to the single crystal aluminium plate impact tests, impact is made in the z-direction, with the material axes defined so that this corresponds to impact along the [001]

crystallographic direction. Both plates are assigned an initial velocity of 250m/s directed towards the centre of the mesh, resulting in a relative impact velocity of 500m/s. A diagram of the computational mesh is shown in Figure 8-24, where it can be seen that 1000 elements are modelled along the z-direction of both plates, with an initial element size of 0.725 μm. This provides a suitable mesh density required to capture the features of interest.

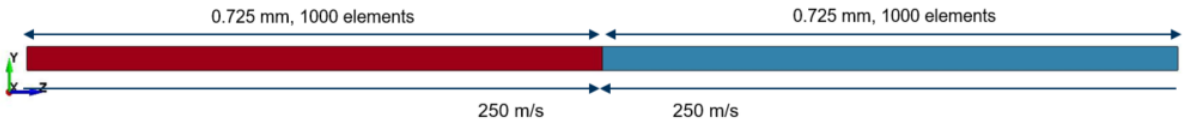

Figure 8-24: Diagram of the computational mesh generated for simulation of the symmetric plate impact. The x and y dimensions are not to scale, having been expanded for clarity of the image.

The material parameters for aluminium provided in Table 8-4 are input, with the equation of state parameters from (Steinberg, 1996) displayed in Table 8-5. The initial value of density of mobile dislocations is 10^6 cm^{-2} and the initial value of the density of immobile dislocations is 10^6 cm^{-2}, which follows values reported in a similar model by Krasnikov (Krasnokov, et al., 2011).

The longitudinal stress component is plotted against distance into the target, with the interface between the two regions of the mesh taken to be the zero point, at time intervals of 2, 5, 10 and 20 nanoseconds.

It is seen in Figure 8-25 that a two-wave structure is formed, with the elastic precursor forming ahead of the main shock front and accelerating away from the shock front. The amplitude of the precursor wave is observed, 2ns after impact, to have an amplitude similar to the level of the main shock front, before decaying over the nanosecond timescale.

This precursor decay is widely explained as being caused by an insufficient initial density of mobile dislocations available to dissipate excess shear stress. This explanation can be verified by Figure 8-26, whereby the same wave profiles as in Figure 8-25 are presented, only with the simulation having been set up with the

initial mobile dislocation density increased by an order of magnitude to a value of 10^7 cm^{-2}.

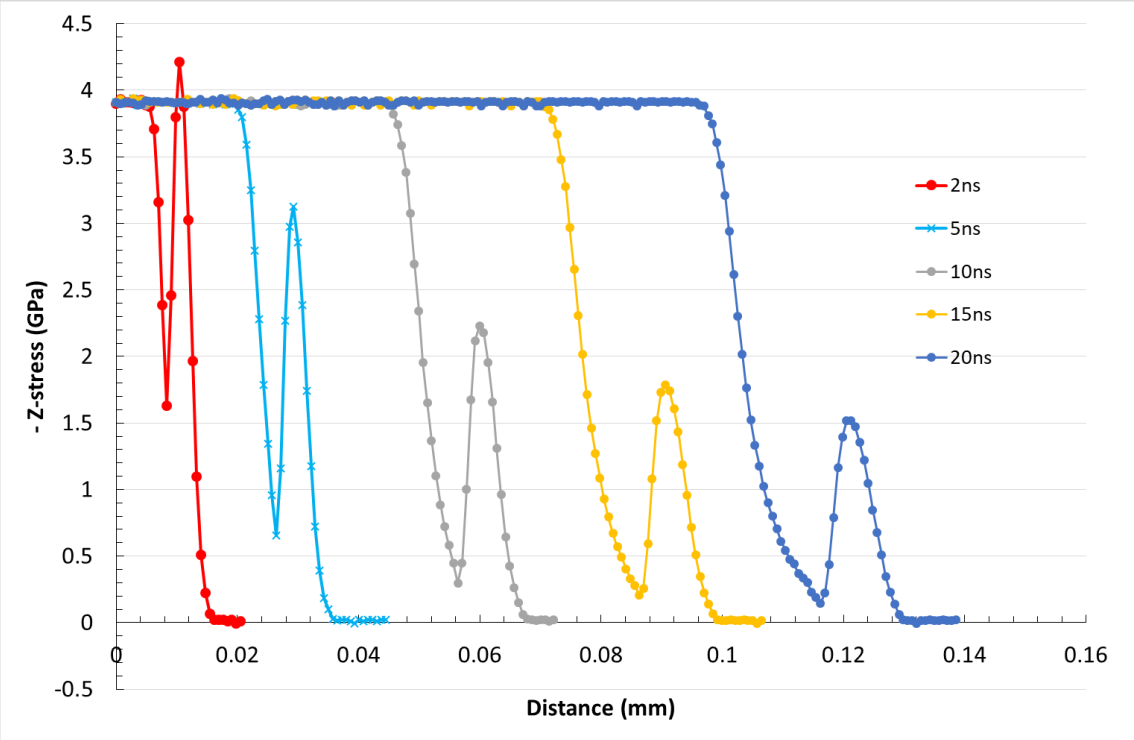

Figure 8-25: Longitudinal stress vs distance in the target plate 2, 5, 10, 15 and 20ns after the impact; with an initial total mobile dislocation density of $10^6 cm^{-2}$.

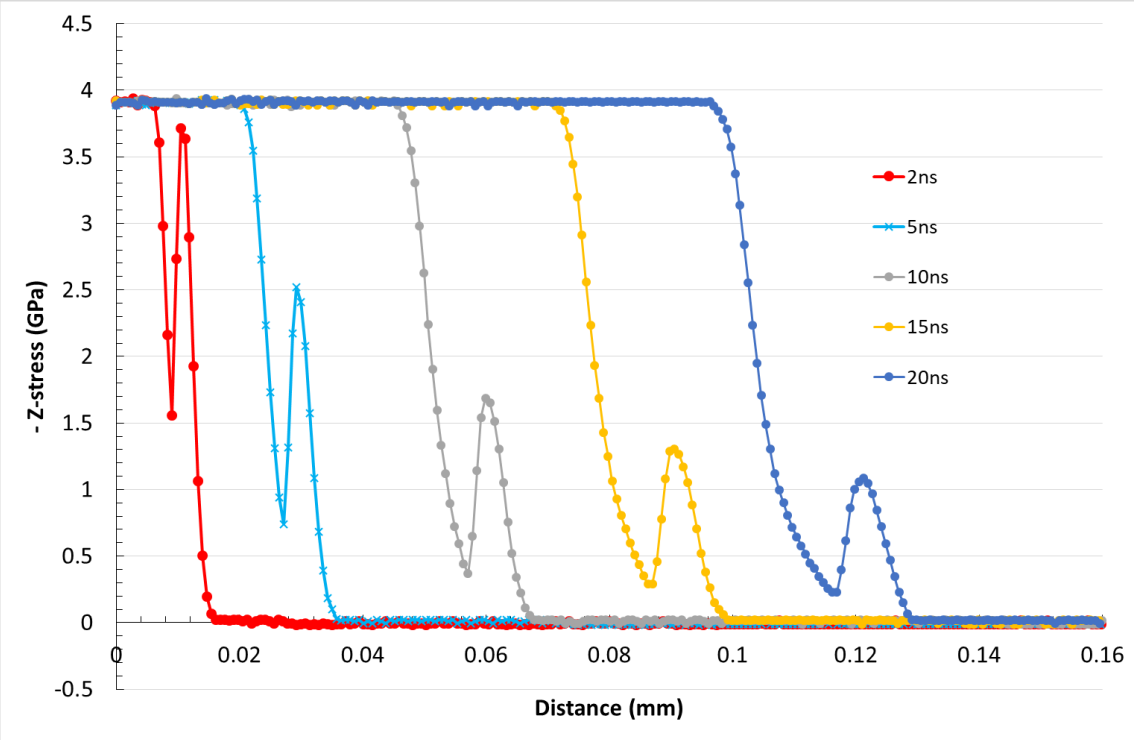

Figure 8-26: Longitudinal stress vs distance in the target plate 2, 5, 10, 15 and 20ns after the impact; with an initial total mobile dislocation density of 10^7 cm^{-2}.

8.6 Summary

A two stage validation process has been carried out, indicating that the new material model is working as expected. The first stage single element tests have verified that the levels of stress calculated by the model are inline with those achieved by other, previously validated models. The second stage of validation, by simulation of plate impact tests, has shown a good level of agreement between the simulated data and experimental data available, with any discrepancies fully explained. Finally, investigation of the precursor wave behaviour over the nanosecond time scale after impact has shown that the model is capable of reproducing superelastic behaviour, as desired.

9 Application of the model to single crystal tantalum (bcc)

The model presented in chapter 6 was primarily developed for fcc metals. In this chapter application of the model is made to a bcc metal in single crystal tantalum. The methodology used to achieve this is discussed, followed by the best result achievable using the model in the current form, and finally a discussion in made outlining the limitations of the model to this application and potential future developments are proposed.

9.1 Determination of material model parameters for single crystal tantalum

Assessment is made of the current models applicability to bcc materials by determination of a set of material parameters for single crystal tantalum and using these to simulate plate impact tests, for which experimental data provided by AWE is readily available for this work (Whiteman, et al., 2014).

The first step of this application is the extension of the slip systems calculated during the initialisation phase. In the fcc model, a single set of 12 slip systems are calculated, the {111} <110> systems; however in the case of the bcc application three sets of slips systems are potentially active. These are the {110} <111>, {112} <111>, and {123} <111> systems, of which there are 12, 12 and 24 systems, respectively, totally 48 slip systems. In line with the fcc model, these are calculated during the initialisation phase, with the material structure indicted (i.e. fcc or bcc) on the material input card.

In addition to extension of the material model to account for 48 bcc slip systems, investigation was made into the determination of nine material model parameters, required for the plasticity part of the model. Four of these parameters, k_a, m_0, ρ_0 and Ω are available in open literature (Mayer, et al., 2013) (Krasnokov, et al., 2011). The parameter $\theta$is the Debye temperature which is widely available in literature (Myers, 1997).

The remaining four parameters, being Y_0, A_I, k_g and V_I, required fitting to the available experimental data for rear surface velocity. Investigation is made to determine the effect varying each of these parameters has on the rear surface velocity of a simulated plate impact test. The aluminium plate impact test, outlined in section-8.3 is used for this purpose. A series of simulations are run, with the value of one of the material parameters of interest changed, while all others retain the values outlined for the aluminium model. Data samples are taken every 5ns for each simulation. This relatively low sampling rate is sufficient for the purposes of this study as the data obtained is only required to provide an indication of the effect each variable has on the rests of the model. This shows directly the effect of each of the parameters on the rear surface velocity trace. Figure 9-1 - Figure 9-3 show the effects the material parameters Y_0, A_I, and V_I, respectively, have on the rear surface velocity trace. It is seen in Figure 9-1 and Figure 9-2 that the parameters Y_0 and A_I control the acceleration of the rear surface caused by the precursor wave. The parameter V_I is seen in Figure 9-3 to only effect the release. Despite Y_0 and A_I also being observed to have effect in the release region, it was decided that these two parameters should be tuned to fit the precursor only, with the velocity parameter, V_I being used to tune the release.

The final fitted parameter, the coefficient of generation of dislocations, k_g, is founds to control the width and shape of the precursor signal.

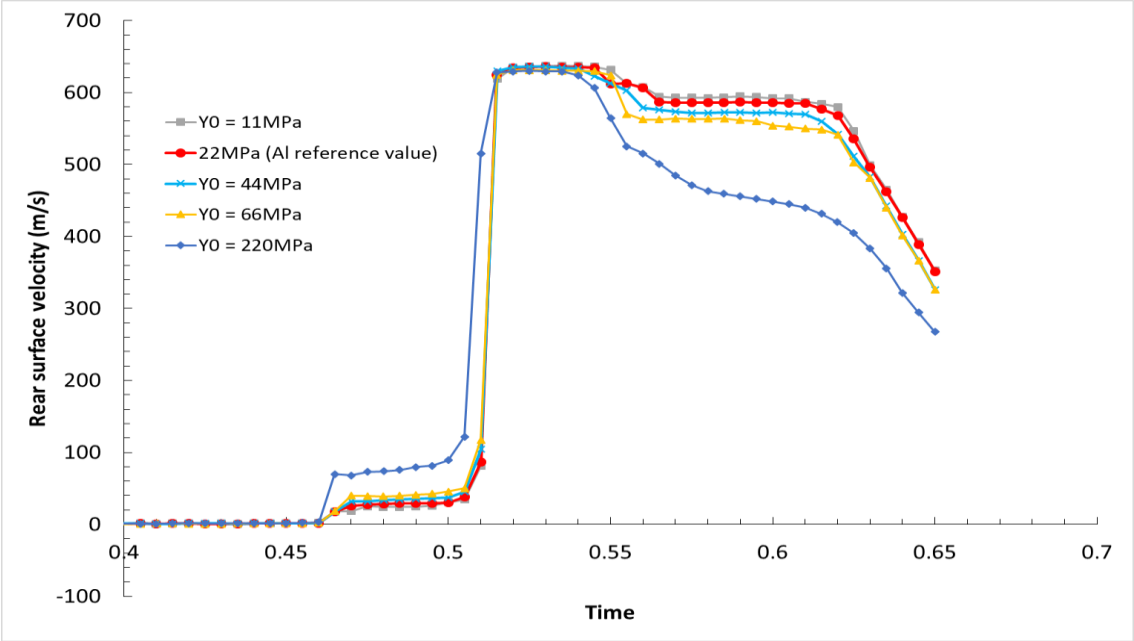

Figure 9-1: Plot showing the rear surface velocity of a 2.9mm thick target plate impacted by a 0.4mm thick flyer plate at 660m/s. Material parameters for aluminium are used for the simulation, with the Y_0 parameter being varied to assess the influence it has on the rear surface velocity. .

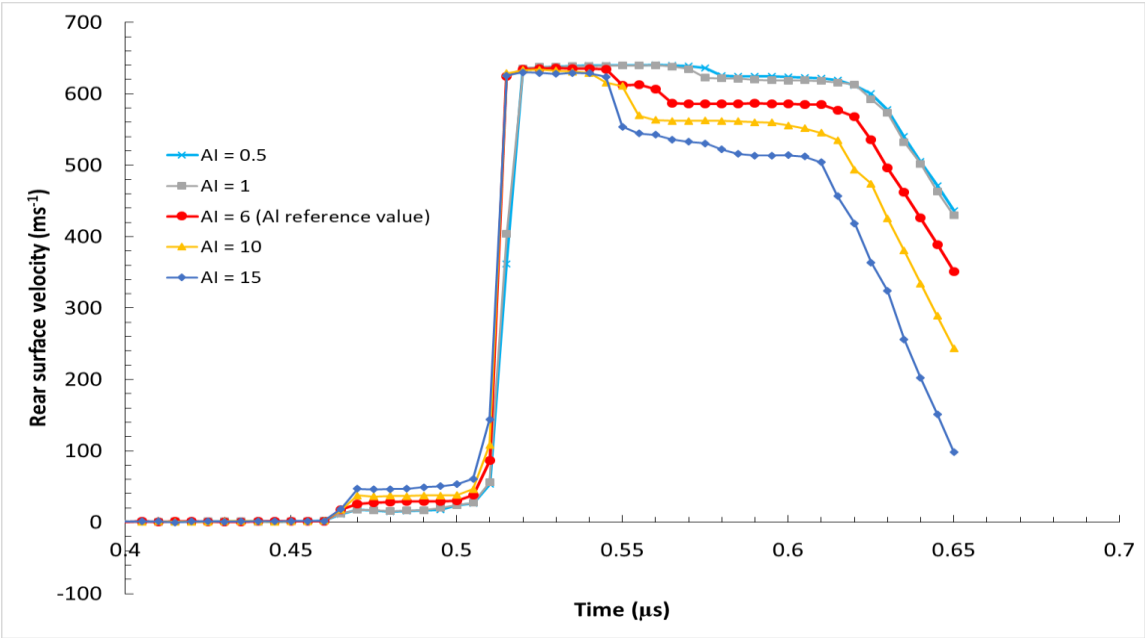

Figure 9-2: Plot showing the rear surface velocity of a 2.9mm thick target plate impacted by a 0.4mm thick flyer plate at 660m/s. Material parameters for aluminium are used for the simulation, with the A_l parameter being varied to assess the influence it has on the rear surface velocity. .

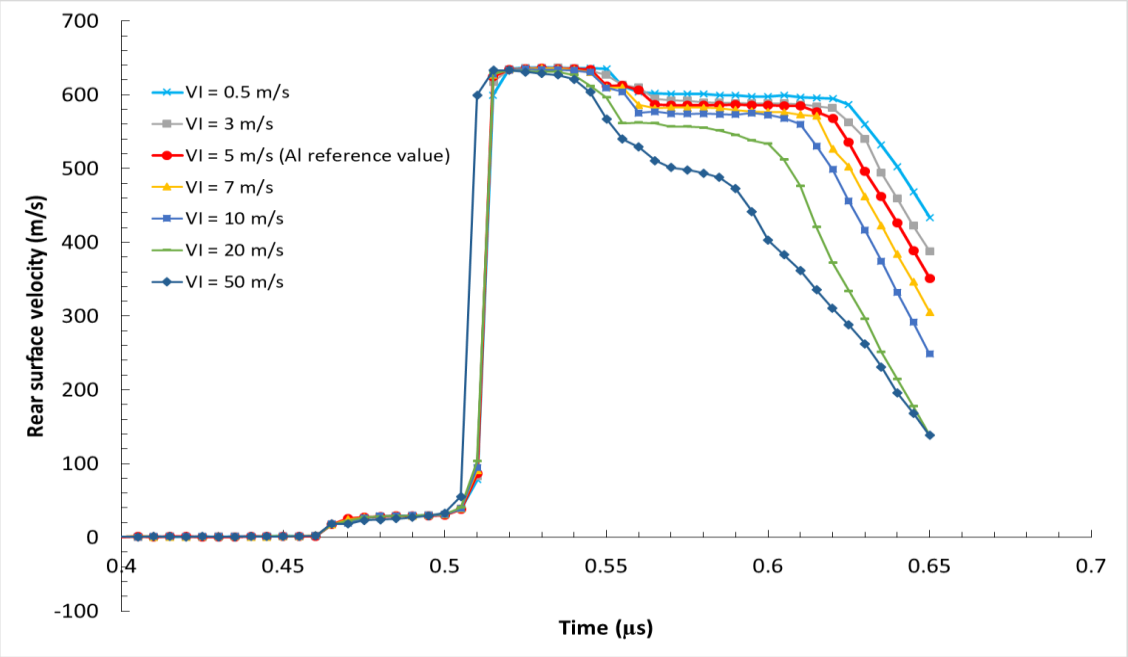

Figure 9-3: Plot showing the rear surface velocity of a 2.9mm thick target plate impacted by a 0.4mm thick flyer plate at 660m/s. Material parameters for aluminium are used for the simulation, with the V_l parameter being varied to assess the influence it has on the rear surface velocity. .

.

9.2 Experimental single crystal tantalum plate impact data

The single crystal tantalum plate impact data available (Whiteman, et al., 2014) consists of the rear surface particle velocity from three experiments. In each experiment a 4mm thick target plate is impacted by a 3mm thick flyer plate at an impact velocity of 726 ms^{-1}. The crystallographic orientation of the target plate, relative to the impact direction, differs between each experiment, with data available for impact along the [100], [110] and [111] directions.

9.3 Simulation of single crystal tantalum plate impact

Simulation of the three single crystal tantalum plate impact experiments is made using a single mesh divided into two separate regions, a flyer region consisting of 4125 solid elements and a target region consisting of 5500 elements. Following mesh density studies, and inline with the validation performed for fcc materials, each element is initially cubic with the dimensions of 0.73 μm. The nodes in the

flyer region are prescribed an initial velocity of 726 ms^{-1}, and the nodes in the target region are initially stationary. Symmetry boundary conditions are applied along the faces parallel to the impact direction to ensure the conditions for uniaxial strain are satisfied.

The material parameters used for simulation of the tantalum plate impact are given in Table 9-1, and the equation of state parameters, available in (Steinberg, 1996), shown in Table 9-2.

Rear surface velocity curves for the plate impact tests are compared to the experimental data (Whiteman, et al., 2014) in Figure 9-4 to Figure 9-6. For all impact directions, the amplitude of the precursor acceleration calculated in the simulations matches that of the experimental data. There is a discontinuity in the experimental data set in Figure 9-4, at the time of the precursor pulse arrival at the rear surface. This discontinuity is explained in (Whiteman, et al., 2014) to be caused by a temporary malfunction of the experimental equipment used. Additionally, the steep rise in velocity caused by the shock front successfully reproduces the same peak velocities as observed experimentally.

The shock front velocity obtained in the simulation of impact in [100] direction given in Figure 9-4, shows a good agreement with the experimental results. It is seen in Figure 9-5 that the model over estimates the velocity of the shock slightly for impact in the [110] direction, with a more pronounced overestimation observed in Figure 9-6 for impact in the [111] direction. The discrepancies are between 1% and 3%. This discrepancy can well be a consequence of the assumptions made within the material model: Equation (6.14) is used with isotropic material constants and does not account for material dependency of the parameters Y_0 and A_I. Equally, error in the fitting of material parameters could not be ruled out due the fitting of material parameters done with the experimental data for [100] impact, without any optimisation applied to minimise fitting errors across all available experimental data. Lastly, the discrepancy could be a limitation of the current form of the model: while the dislocation kinetic equations have been

shown to accurately reproduce fcc metal behaviour, dislocation motion in bcc metals has additional complexities which may need to be accounted for.

Table 9-1: Material model parameters for single crystal tantalum

Model parameter	Tantalum
E	186 GPa
G	69 GPa
μ	0.34
ρ_0	10^7 cm^{-2}
k_g	1 x 10^{18} J^{-1}
k_a	10
A_1	0.1
V_1	1 m/s
θ	255 K
Y_0	800MPa
m_0	10^{-15}
a	3.306 Å

Table 9-2: Gruneisen equation of state parameters for tantalum (Steinberg, 1996)

Equation of state parameter	Tantalum
Velocity curve intercept, C	0.341 cm/μs
First slope coefficient, S_1	1.20
Gruneisen coefficient, γ_0	1.67
First order volume correction coefficient, a	0.42

An interesting feature of the simulation results is the successful prediction of the apparent kink which appears in the sharp rise of rear surface velocity in all test cases considered. These kinks, also observed in characterisation of the shock loaded tantalum published in (Asay, et al., 2011) (Ding & Asay, 2011), can be seen to have different characteristics in the experimental data sets, with the [110] loading direction presented in Figure 9-5 being the most pronounced, a trait which is captured with a good degree of accuracy by the material model. Analysis of the nodal velocity and stress time history, obtained in an element near to the rear surface and illustrated in Figure 9-7, shows that the kink in the velocity curve is a result of a temporary drop in the magnitude of the z-stress component. This temporary drop in the magnitude of the z-stress component can be explained by Figure 9-8. Figure 9-8 shows the time history of the mobile dislocation density for each slip system, plotted alongside the z-stress in an element near to the rear surface. It is seen that, the increase in the density of mobile dislocations occurs at different time instances for different sets of slip systems, implying that slip systems are activated at different time instances. The time instance of the drop in the magnitude of the z-stress component is the same time instant that the delayed slip systems are activated. This activation allows for a higher degree of plastic flow, and therefore the dissipation of a higher amount of shear stress. Similar analysis for the [100] and [111] loading directions show the same characteristics.

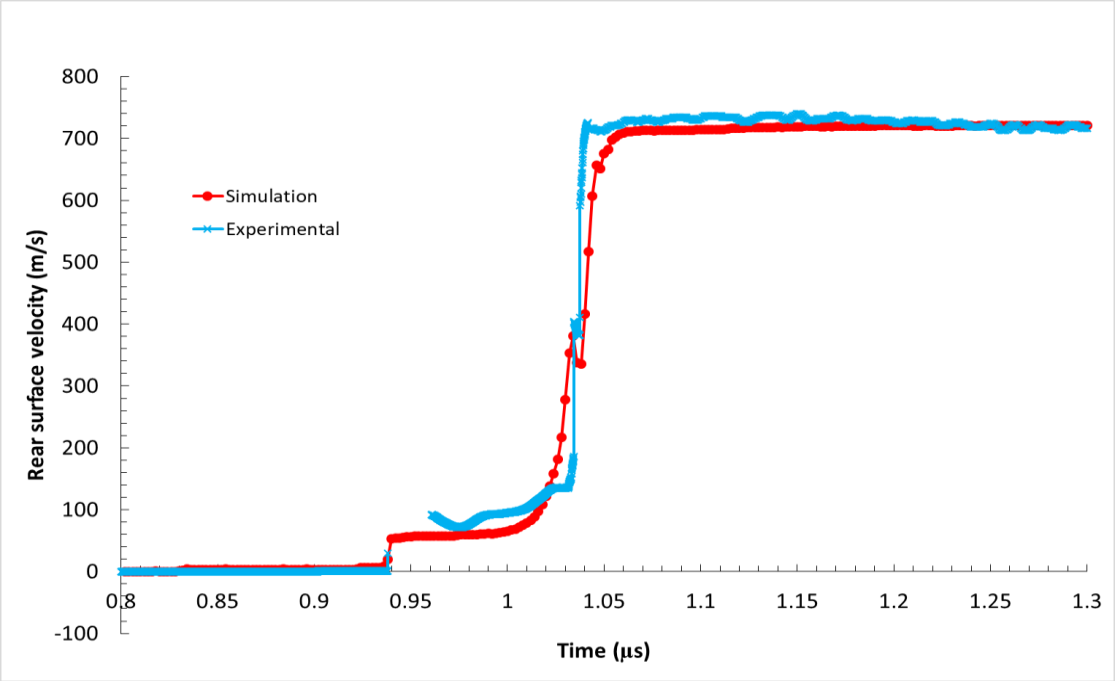

Figure 9-4: Comparison of simulation and experimental rear surface velocity data for a 4mm thick single crystal tantalum target plate being impacted by a 3mm thick tantalum flyer plate at 726 m/s. Impact is made along the [100] direction of the target.

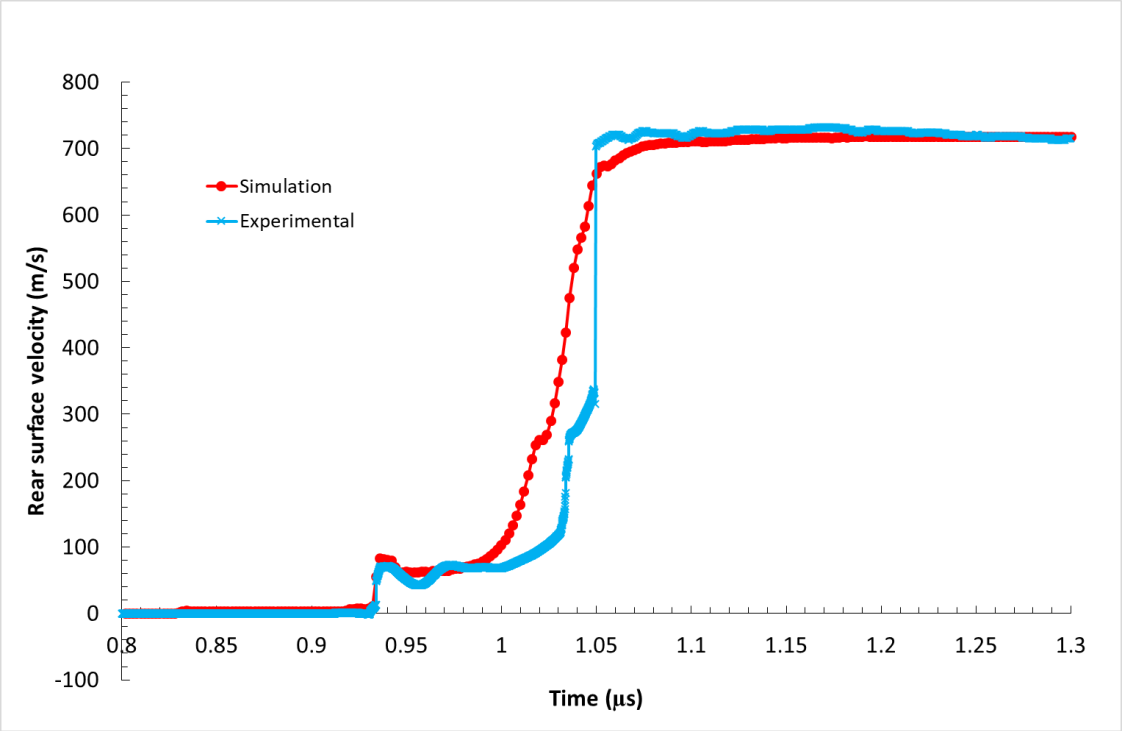

Figure 9-5: Comparison of simulation and experimental rear surface velocity data for a 4mm thick single crystal tantalum target plate being impacted by a 3mm thick tantalum flyer plate at 726 m/s. Impact is made along the [110] direction of the target.

Despite the discussed discrepancies between the simulation and experimental data, the main features of the experimental curves are reproduced in the simulation. The amplitude of the precursor acceleration is accurately reproduced, with the initial overshoot observed in the case of the [110] and [111] impact directions. Additionally, the experimentally observed kink in the shock acceleration is reproduced in the simulations, with the unique character of each correctly predicted. Further, the magnitude of rear surface velocity at which these features are observed shows a good level of agreement between the simulation and experimental data. Finally, for all three test cases the maximum rear surface velocity is correctly predicted.

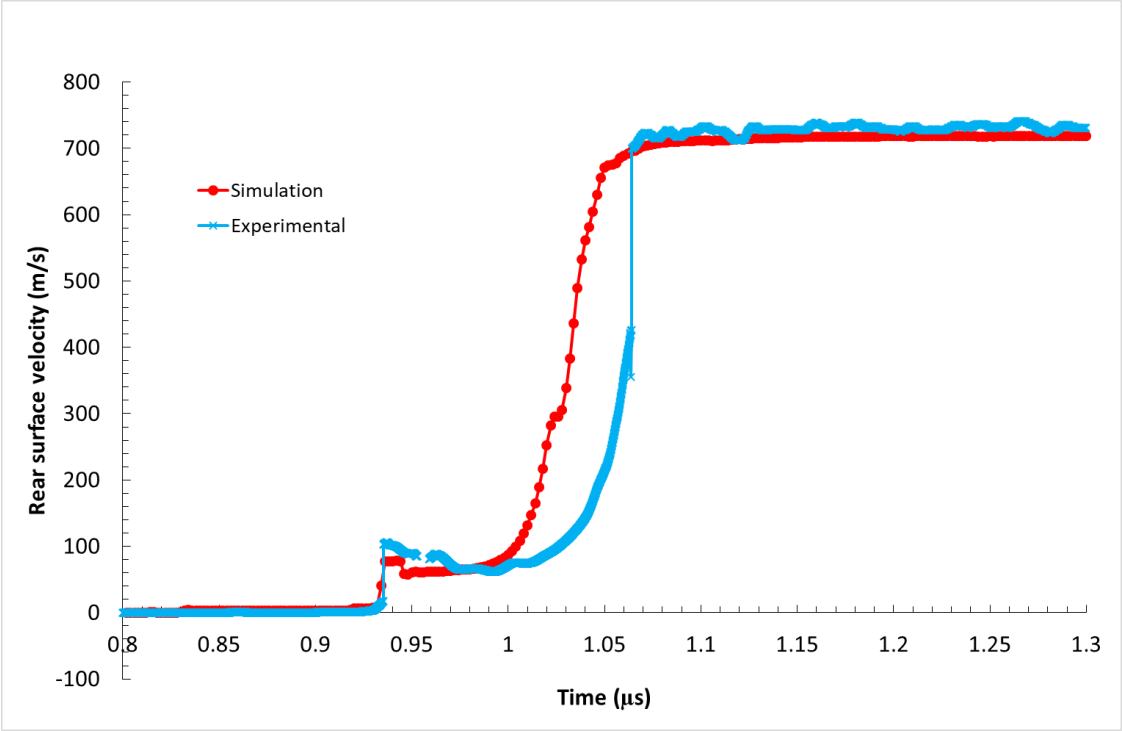

Figure 9-6: Comparison of simulation and experimental rear surface velocity data for a 4mm thick single crystal tantalum target plate being impacted by a 3mm thick tantalum flyer plate at 726 m/s. Impact is made along the [111] direction of the target.

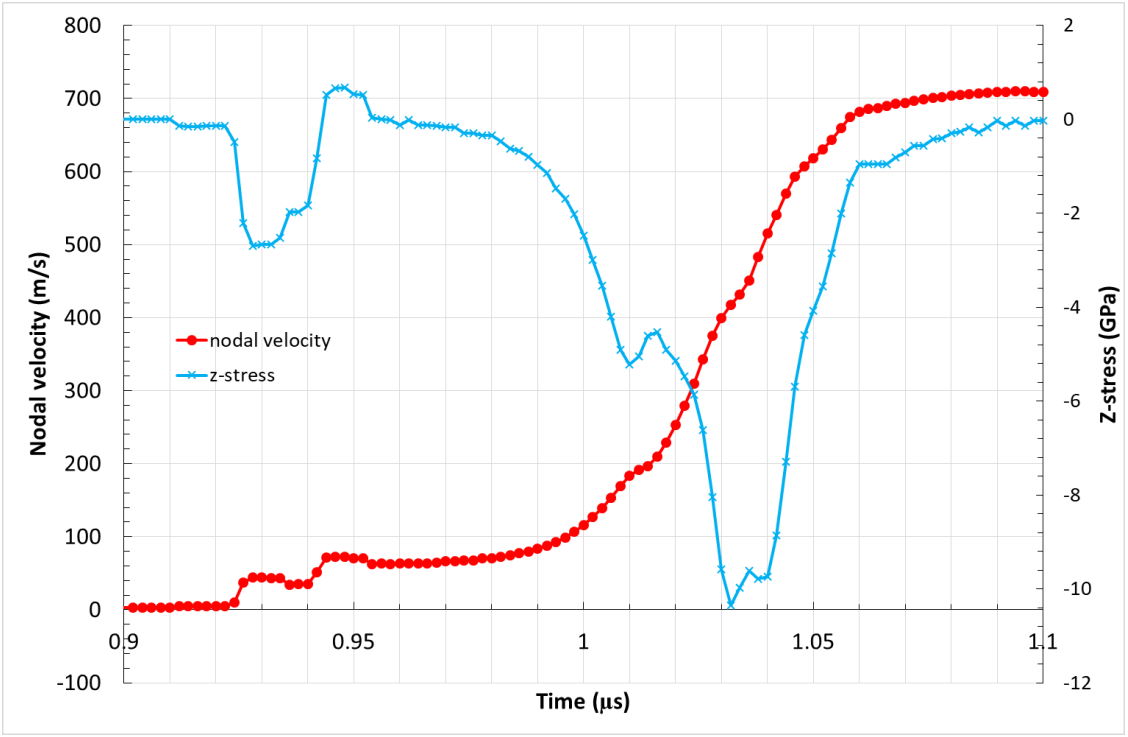

Figure 9-7: Nodal velocity plotted against the z-stress component in an element near to the rear surface of a 4mm thick single crystal tantalum which has been impacted by a 3mm thick flyer plate at a velocity of 726m/s, with impact along the [110] axis of the target.

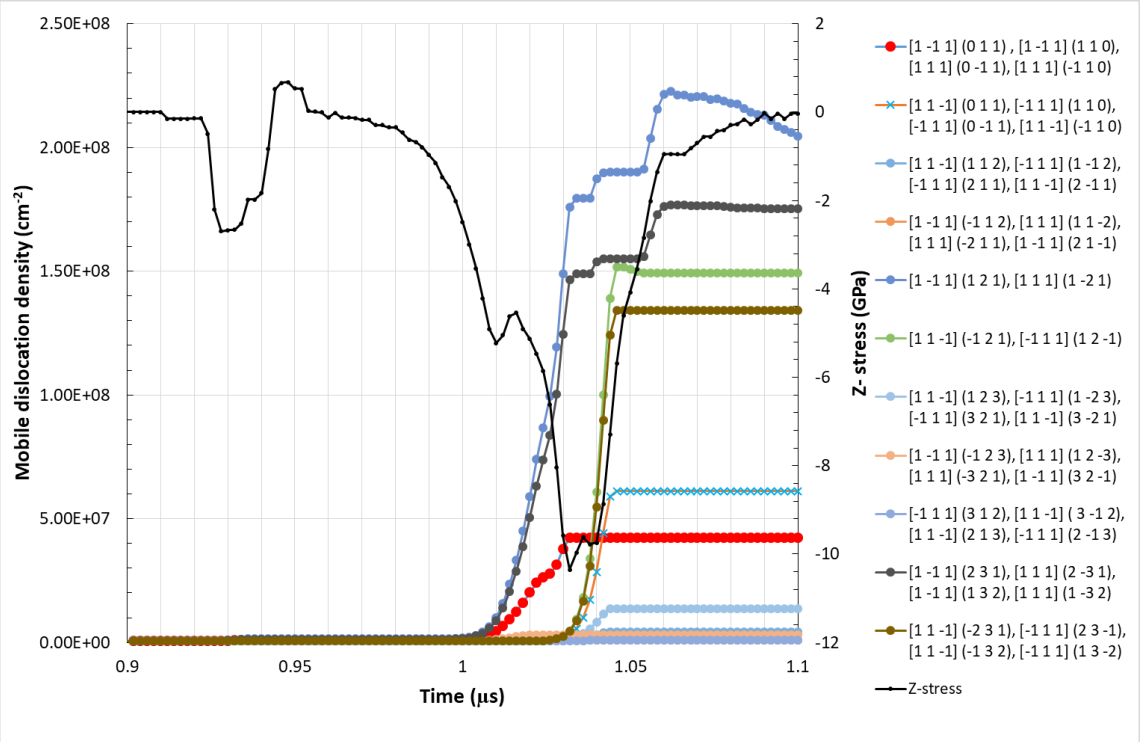

Figure 9-8: Mobile dislocation density of each slip system plotted alongside the z-stress component in an element near to the rear surface of a 4mm thick single crystal tantalum which has been impacted by a 3mm thick flyer plate at a velocity of 726m/s, with impact along the [110] axis of the target.

9.4 Additional bcc considerations

From Figure 9-4, Figure 9-5 and Figure 9-6, it is seen that using a single set of material parameters for all three impact directions through the crystal does not accurately reproduce the experimental data available. The two main features that differ between the results for different impact directions are the amplitude of the precursor acceleration and the width of the precursor pulse.

The reduced width of the precursor pulses for the [110] and [111] impact directions indicate that either the shock velocity or the velocity of the precursor pulse is incorrectly predicted. The shock velocity is controlled by the equation of state and the velocity of the precursor pulse by the elastic properties of the material. It is likely that this is a result of the elastic properties being treated as constants, and the material as isotropic. It is apparent from the Figure 9-4, Figure

9-5 and Figure 9-6, that single crystal tantalum is not isotropic and therefore further work is required to ensure the elastic properties used in modelling replicate this.

The material parameter fitting process has shown that the amplitude of the precursor acceleration is directly controlled by the parameters Y_0 and A_I, both of which are influential in the yield strength calculation. It can therefore be concluded that the yield function used in the current model is insufficient for accurately modelling anisotropic single crystal tantalum, due to the function having a single value for all directions and slip systems.

It is widely accepted that the yielding bcc crystals is more complex than the yielding of fcc crystals. This can potentially be attributed to the fact that there is an apparent breakdown of Schmid's law in bcc crystals (Groger, et al., 2008) (Groger, et al., 2008) (Groger & Vitek, 2008) (Ito & Vitek, 2001) (Patra, et al., 2014) (Qin & Bassani, 1992) (Weinberger, et al., 2012). Schmid's law states that only the shear stress resolved in the direction of dislocation motion influences the movement of the dislocation. However, in bcc crystals it is found that dislocation slip is primarily carried ½[111] screw dislocations, which due to their nature are constrained by direction only and not by crystallographic planes. As a result of this, a screw dislocation with a direction of [111] can exist on three slip planes, with equal priority. The resolved force on the each of these three slip planes affect the nature of the dislocation core, which in turn affects the ability of the dislocation to move on the other slip systems. Therefore, the motion of dislocations in a bcc slip system is not only driven by the resolved shear stress on that slip system, but is also affected by forces acting on other directions.

Currently, the model developed in this work utilises Schmid's law as the criterion for plasticity. It is seen in equation (6.13) that dislocations will move and therefore plasticity will develop in a slip system if the resolved shear stress is greater than the inherent lattice resistance. Therefore, adaptation to the yield calculation, and consequently the criterion for plasticity to develop, is required to account for these additional terms. This will provide that the yield function will need to be calculated

per slip system, and will naturally ensure it becomes sensitive to the loading direction.

Following (Groger, et al., 2008) (Weinberger, et al., 2012) it is proposed that for modelling of bcc metals, the calculation of the resolved shear stress should take the form:

$$\mathbf{s}^{\beta} \cdot \boldsymbol{\sigma}\mathbf{n}^{\beta} + a_1 \mathbf{s}^{\beta} \cdot \boldsymbol{\sigma}\mathbf{n}_1^{\beta} + a_2 \left(\mathbf{n}^{\beta} \times \mathbf{s}^{\beta}\right) \cdot \boldsymbol{\sigma}\mathbf{n}^{\beta} + a_3 \left(\mathbf{n}_1^{\beta} \times \mathbf{s}^{\beta}\right) \cdot \boldsymbol{\sigma}\mathbf{n}_1^{\beta} = \frac{F_D^{\beta}}{b} \qquad (9.1)$$

Where $\mathbf{n}_1^{\beta}$ is the unit vector of a plane in the zone of $\mathbf{s}^{\beta}$ that makes an angle of -60°with the vector $\mathbf{n}^{\beta}$ (Weinberger, et al., 2012), and a_1, a_2 and a_3 are material constants.

9.5 Summary

The process taken to apply the new material model to modelling of the bcc single crystal tantalum has been discussed. The results obtained using the best fitting material parameters show that the new model reproduces all of the main features observed in the experimental rear surface velocity plots. Discrepancies between the simulated and experimental data have been discussed, with a potential future improvement to the model identified.

10 Conclusions

A new dislocation dynamics based continuum model for modelling plasticity at shock loading has been described, implemented and tested. The underlying dislocation physics have been detailed which provide a validation of the formulation of the material model.

Implementation of the model has been made in the DYNA3d hydrocode as a new material model, and coupled with a vector equation of state. The vector equation of state describes the generalised pressure required for accurate modelling of orthotropic materials. The single crystals considered in this work do not exhibit orthotropic behaviour due to the inherent symmetry of their cubic crystal structures, however this coupling is included to allow for potential future developments of the model, specifically an extension to modelling polycrystalline metals.

Validation of the model has been achieved for fcc metals by simulation of plate impact tests. Simulation has been made for two different metals, single crystal aluminium and single crystal copper, and for different geometries. Good agreement is observed between simulated rear surface velocity data and the experimental data available.

Investigation of the initial amplitude and subsequent decay of an elastic precursor wave has been made. It is observed that the initial amplitude of this wave is at a similar level to the main shock front, with decay to the HEL level occurring over a time scale of tens of nanoseconds. Further investigation of this behaviour shown that it is the initial mobile dislocation density that controls this.

Analysis of the material parameters has been made, with the method of deriving each of these shown in Table 10-1. Of the 12 material parameters, the values of 5 can be found in open literature, 3 can be estimated from theory and the remaining 4 are fitted. The four parameters that are fitted are the yield parameter, Y_0 , the coefficient of generation of dislocations, k_g , the hardening coefficient A_1 and the immobilisation velocity, V_I . The procedure followed in this work to fit the

parameters used rear surface velocity plate impact data, with each parameter found to control a certain aspect of the trace. The yield parameter and the hardening coefficient were found to control the magnitude of the precursor region, with each tuned to provide optimal results. The coefficient of generation of dislocations was found to control the width and shape of the precursor region and can therefore be fitted accordingly. Finally the immobilisation velocity controls the release and is fitted to this region of the rear surface velocity trace.

Table 10-1: Material parameters required for the new material model and indication of how to determine them

Model parameter	Method of derivation
Youngs modulus, E	Literature
Shear modulus, G	Literature
Poissons ratio, ν	Literature
Minimum dislocation density required for immobilisation, ρ_0	Literature
Coefficient of generation of dislocations, k_g	Fitted
Coefficient of annihilation of dislocations, k_a	Estimated from theory
Hardening coefficient, A_I	Fitted
Immobilisation velocity, V_I	Fitted
Debye temperature, θ	Calculated
Yield parameter, Y_0	Fitted
Dislocation rest mass, m_0	Calculated from theory
Lattice constant, a_0	Literature

Further application of the model has been made to single crystal tantalum, a bcc metal. This has shown that the capability of the model in its current form reproduces all the main features observed experimentally during plate impact experiments, but also shows that further adaptations are required to account for the more complex yield nature of bcc crystals. A new method for calculation of the mechanical force driving dislocation motion specific to bcc metals is proposed for future inclusion in the model.

10.1 Proposed future work

- Implementation and testing of the new mechanical force calculation proposed in chapter 9 for the application of the model to bcc materials.
- Coupling of the model with a suitable damage model

10.2 Novel aspects of this work

Novel aspects of this work include:

- Implementation of a full 3D model in the framework of the hydrocode, which was previously available in literature in a 1D form only.
- Successful coupling of the new model with an equation of state in the hydrocode
- Validation of the 3D model for FCC single crystal metals
- Successful capture of superelastic precursor behaviour in the finite element model.
- The application of the model to bcc materials, in the form of single crystal tantalum
    - Complexities oadditinal slip systems incorporated in the hydrocode
    - Parameters for single crystal tantalum determined
    - Experimentally observed features captured in simulations and explained.

11 References

Anglade, P.-M., Jomard, G., Robert, G. & Zerah, G., 2005. Computation of the Peierls stress in tantalum with an extended-range modified embedded atom method potential. Volume 17, pp. 2003-2018.

Anon., 2012. *Line defects.* [Online] Available at: http://www.mechlook.com/line-defects/ [Accessed 02 07 2013].

Anon., 2013. *Slip (materials science) page.* [Online] Available at: http://en.wikipedia.org/wiki/slip(materials science) [Accessed 4 6 2013].

Asay, J. R., Vogler, T. J., Ao, T. & Ding, J. L., 2011. Dynamic yielding of single crystal Ta at strain rates of ~5 x 10^5 /s. *Journal of Applied Physics ,* 109(073507).

Austin, R. & McDowell, D., 2011. A dislocation-based constitutive model for viscoplastic deformation of fcc metals at very high strain rates.. 27(1).

Banerjee, B. & Bhawlkar, A. S., 2008. An extended mechanical threshold stress plasticity model: Modelling 6061-T6 Aluminium alloy. *Journal of mechanics of materals and structures,* 3(3), pp. 391-424.

Bangalor, I., 2014. *NPTEL.* [Online] Available at: http://www.nptel.ac.in/courses/105108072/4 [Accessed 01 03 2018].

Brannon, R. M. & Drugan, W. J., 1995. Requirements of Thermodynamics in the Analysis of Elastic-Plastic Shock Waves. *Journal of the Mechanics and Physics of Solids,* 43(6), pp. 973-1001.

Chadwick, P., 1999. *Continuum Mechanics: Concise Theory and Problems.* Dover ed. New York: Dover Publications.

Colvin, J., Minich, R. & Kalantar, D., n.d. A model for plasticity kinetics and its role in simulating the dynamic behaviour of Fe at high strtain rates. 25(4).

Courant, R. & Friedrichs, K. O., 1948. *Supersonic Flow and Shock Waves.* Applied Mathermatical Sciences, vol 21 ed. New York: Springer.

Ding, J. L. & Asay, J. R., 2011. Modeling of the dynamic inelasticity of tantalum single crystals under ramp wave loading. *Journal of Applied Physics ,* 109(083505).

Djordjevic, N., 2011. *Modelling the inelastic behaviour of orthotropic material under dynamic loading including high velocity impact (PhD Thesis),* Cranfield: Cranfield University.

Djordjevic, N., 2011. *Modelling the inselastic behaviour of orthotropic material under dynamic loading including high velocity impact (PhD Thesis),* Cranfield: Cranfield University.

Drugan, W. J., 1986. A More Direct and General Analysis of Moving Strong Discontinuity Surfaces in Quasi-Statically Deforming Elastic-Plastic Solids. *Journal of Applied Physics - Transactions of the ASME,* 53(1), pp. 224-226.

Drugan, W. J. & Shen, Y., 1990. Finite Deformation Analysis of Restrictions on Moving Strong Discontinuity Surfaces in Elastic-Plastic Materials: Quasi-Static and Dynamic Deformations. *J. Mech. Phys. Solids,* 38(4), pp. 553-574.

Drugan, W. & Shen, Y., 1987. Restrictions on Dynamically Propagating Surfaces of Strong Discontinuity in Elastic-Plastic Solids. *Journal of the Mechanics and Physics of Solids,* 35(6), pp. 771-787.

Follansbee, P. S. & Kocks, U. F., 1988. A constitutive description of the deformation of copper based on the use of the mechanical threshold stress as an internal state variable. *Acta Matallurgica,* 36(1), pp. 81-93.

Groger, R., Bailey, A. G. & Vitek, V., 2008. Multiscale modelling of plastic deformation of molybdenum and ynugsten: I. Atomistic studies of the core

structure and glide of 1/2<111> screw dislocations at 0K. Volume 56, pp. 5401-5411.

Groger, R., Racherla, V., Bassani, J. L. & Vitek, V., 2008. Multiscale modelling of plastic deformation of molybdenum and tungsten: II. Yield criterion for single crystals based on atomistic studies of glide of 1/2<111> screw dislocations. Volume 56, pp. 5412-5425.

Groger, R. & Vitek, V., 2008. Multiscale modeling of plastic deformation of molybdenum and tungsten. III. Effects of temperature and plastic strain rate. Volume 56, pp. 5426-5439.

Groh, S., Marin, E. & Horstemeyer, M. a. Z. H., 2009. Multiscale modeling of the plasticity in an aluminum single crystal.. 25(8).

Hadamard, J., 1903. *Lecons sur la propagation des Ondes et les equations de l'hydrodynamiques.* Paris: Librairie Scientific, A Hermann.

Hansen, B., Beyerlein, I., Bronkhorst, C. & Cerreta, E. a. D.-K. D., 2013. A dislocation-based multi-rate single crystal plasticity model. Volume 44.

Hirth, J. P. & Lothe, J., 1982. *Theory of dislocations.* New York: John Wiley and Sons.

Holzapfel, G. A., 2000. *Nonlinar solid mechanics a continuum approach for engineering.* Chichester: Wiley.

Hull, D. & Bacon, D. J., 2001. *Introduction to dislocations.* Oxford: Butterworth Heinemann.

Inogamov, N. A., Zhakhovskil, V. V., Khokhlov, V. A. & Shepelve, V. V., 2011. Superelasticity and the propagation of shock waves in crystals. *JETP Letters,* 93(4), pp. 226-232.

Ito, K. & Vitek, V., 2001. Atomistic study of non-Schmid effects in the plastic yielding of bcc metals. 81(5), pp. 1387-1407.

Jason, L., n.d. *Wikipedia.* [Online] Available at: https://commons.wikimedia.org/w/index.php?curid=5328374 [Accessed 28 May 2019].

Johnson, G. & Cook, W., 1983. *A constitutive model and data for metals subjected to large strain, high strain rates and high temperatures.* The Hague, s.n., pp. 541-547.

Kanel, G. I., Razorenov, S. V., Baumung, K. & Singer, J., 2001. Dynamic yield and tensile strength of aluminium single crystals at temperature up to melting point. *Journal of applied physics,* 90(1), pp. 136-143.

Kanel, G. I., Razorenov, S. V., Utkin, A. V. & Baumung, K., 1996. Experimental profiles of shock waves. *Preprint of scientific association IVTAN of RAS.*

Khan, A. & Liu, J., 2016. A deformation mechanism based crystal plasticity model of ultrafine-grained/nanocrystalline FCC polycrystals. Volume 86.

Khan, A., Liu, J., Yoon, J. & Nambori, R., 2015. Numerical implementation of a crystal plasticity model with dislocation transport for high strain rate applications.. Volume 86.

Kiely, L., 2013. *Review of new methods of modelling plasticity,* Cranfield: Cranfield University.

Krasnikov, V. S., Kuksin, A. Y., Mayer, A. E. & Yanilkin, A. V., 2010. Plastic deformation under high rate loading: The multiscale approach. *Physics of the solid state,* 52(7), pp. 1386-1396.

Krasnokov, V., Mayer, A. & Yalovets, A., 2011. Dislocation based high-rate plasticity model and its application to plate-impact and ultra short electron irradiation simulation. *International Juornal of Plasticity,* Volume 27, pp. 1294-1308.

Kuhlmann-Wilsdorf, D., 2004. Advancing towards constitutive equations for the metal industry via the LEDS theory. *Metallurgical and materials transactions B,* Volume 35B.

Lin, J. I., 2004. *DYNA3D: A nonlinear, explicit, three-dimensional finite element code for solid and structural mechanics.* CA USA: Lawrence Livermore National Laboratories.

Luscher, D. et al., 2016. Coupling continuum dislocation transport with crystal plasticity for application to shock loading conditions. Volume 76.

Malygin, G. A., 1999. Dislocation self-organization processes and crystal plasticity. *Physics - Uspekhi,* 42(9), pp. 887-916.

Mandel, J., 1972. *Plasticite classique et viscoplasticite.* Springer, Vienna, s.n.

Mandel, J., 1974. Thermodynamics and plasticity . In: *Foundations of continuum thermodynamics .* s.l.:s.n., pp. 283-304.

Mase, G. E., 1970. *Schaum's outline series: Theory and problems of continuum mechanics.* New York: McGraw-Hill.

Mayer, A. E., Khishchenko, K. V., Levashov, P. R. & Mayer, P. N., 2013. Modeling of plasticity and fracture of metals at shock loading. *Journal of applied physics,* 113(19).

Mayeur, J. et al., 2016. Numerical implementation of a crystal plasticity model with dislocation transport for high strain rate applications.. 24(4).

Meyers, M. A., 1994. *Dynamic behaviour of materials.* New York: John Wiley and Sons.

Myers, H. P., 1997. *Introductry solid state physics.* London: Taylor and Francis.

Panov, V., 2006. *Modelling of behaviour of metals at high strain rates,* Cranfield University: PhD Thesis, Cranfield University.

Park, N., 2010. *Modelling Shocks using molecular dynamics,* s.l.: PhD Thesis Cranfield Univeristy.

Patra, A., Zhu, T. & McDowell, D. L., 2014. Constitutive equations for modelling non-Schmid effects in single crystal bcc-Fe at low and ambient temperatures. Volume 59.

Qi, C., Wang, M. & Qian, Q., 2009. Strain-rate effects on the strength and fragmentation size of rocks. *International journal of impact engineering,* Volume 36, pp. 1355-1364.

Qin, Q. & Bassani, J. L., 1992. Non-Schmid yield behaviour in single crystals. 40(4), pp. 813-833.

Reese, S. & Vladimirov, I. N., 2008. Anisotropic Modelling of Metals in Forming Processes. *IUTAM Symposium on Theoretical, Computational and Modelling Aspects of Inelastic Media,* Volume 11, pp. 175-184.

Steinberg, D. J., 1996. *Equation of state and strength properties of selected materials,* Livermore: Lawrence Livermore National Laboratory.

Steinberg, D. J., Cochran, S. G. & Guinan, M. W., 1980. A constitutive model applicable at high-strain rate. *Journal of Applied Physics,* Volume 51, p. 1498.

Steinberg, D. J. & Lund, C. M., 1989. A constitutive model for strain rates from 10^-4 to 10^6 s^-1. *Journal of Applied Physics,* Volume 65, p. 1528.

Suzuki, T., Takeuchi, S. & Yoshinaga, H., 1991. *Dislocation Dynamics and Plasticity.* New York: Springer-Verlag.

Vignjevic, R., Campbell, J., Bourne, N. K. & Djordjevic, N., 2008. Modelling shock waves in orthotropic elastic materials. *Journal of Applied Physics,* Volume 104.

Vignjevic, R., Djordjevic, N. & Panov, V., 2012. Modelling of dynamic behaviour of orthotropic metals including damage and failure. Volume 38, pp. 47-85.

Vladimirov, I. N., Pietryga, M. P. & Reese, S., 2009. Anisotropic finite elastoplasticity with nonlinear kinematic and isotropic hardening and application to sheet metal forming. *International journal of plasticity ,* 26(5), pp. 659-687.

Wallace, D. C., 1980. Irreversible thermodynamics of flow in solids. *Phys. Rev B,* Volume 22, p. 1477.

Weinberger, C. R., Battaile, C. C., Buchheit, T. E. & Holm, E. A., 2012. Incorporating atomistic data of lattice friction into BCC crystal plasticity models. Volume 37, pp. 16-30.

Whiteman, G., Case, S. & Millett, J. F., 2014. Planar shock compression of single crystal tantalum from 6-23 GPa. *Journal of Physics: Conference series,* Volume 500.

Zerilli, F. J. & Armstrong, R. W., 1987. Dislocation mechanics based constitutive relations for material dynamics calculations. *Journal of Applied Physics,* 61(5), pp. 1816-1825.

Zhakhovsky, V. et al., 2012. Super-elastic response of metals to laser-induced shock waves. *AIP Conf. Proc,* Volume 1464 102.

Appendix A : Mesh sensitivity study

A mesh sensitivity study has been performed for the new material model and is presented in this appendix.

The mesh sensitivity study is performed by simulation of a plate impact test, whereby a 0.4mm aluminium flyer plate impacts a 2.9mm aluminium target plate at 660 m/s. The simulation set up consists of a single, continuous mesh, split into two regions, the target region and the flyer region. The target region is initially at rest, whereas the flyer region has an initial velocity of 660 m/s in the direction of the target. This follows the plate impact tests used for validation of the fcc model.

To assess the sensitivity of the model to the mesh size, 10 different mesh densities are generated, with the number of elements along the 2.9mm target ranging from 500 to 5000 elements. This corresponds to a range of initial element sizes of 0.0058mm – 0.00058mm. Meshes this fine are required to capture the details of the narrow shock front. Table_Apx A-1 provides details of the initial element sizes used in each test.

For each mesh size, the simulation is made and the initial stress wave development is analysed at time intervals of 2, 5, 10 and 20ns. The stress waves are then plotted vs distance the wave has propagated into the target at each time instant and compared to the same results obtained using the other mesh sizes.

Figure_Apx A-1, Figure_Apx_A-2, Figure_Apx A-3 and Figure_ApxA-4 show the comparison of the stress waves obtained at time instances of 2, 5, 10 and 20ns, respectively. It is seen that, in Figure_Apx A-1 the results are largely scattered and noisy. This is due to the ultra fine timescale over which this graph is plotted, however, it can be observed that the results obtained using 4000, 4500 and 5000 elements along the target plate, the stress profile is very similar. The subsequent results displayed in Figure_Apx A-2, Figure_Apx A-3 and Figure_Apx A-4, clearly shows a convergence of the stress profiles for the profiles obtained using 4000, 4500 and 5000 elements along the target. Therefore it is concluded that, for simulation of a 2.9mm plate, 4000 elements is the minimum required for accurate stress prediction. This corresponds to an initial element size of 0.725μm.

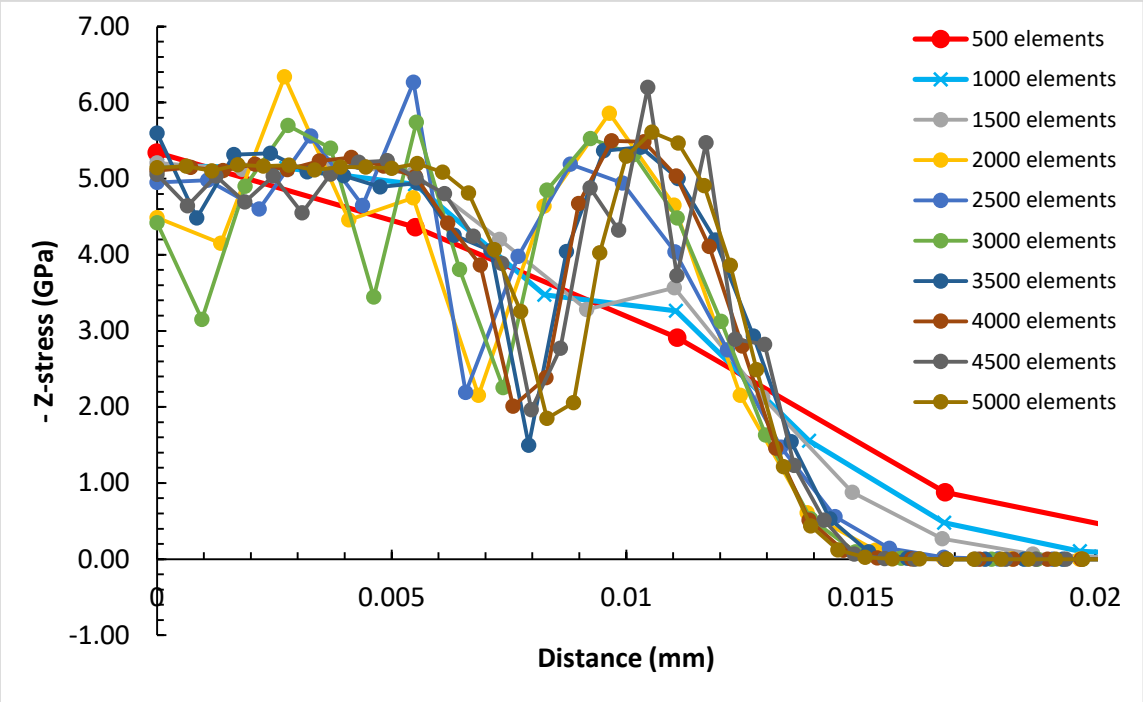

Figure_Apx A-1: Z-stress vs distance wave has propagated into aluminium target plate 2ns after impact for a range of initial element sizes.

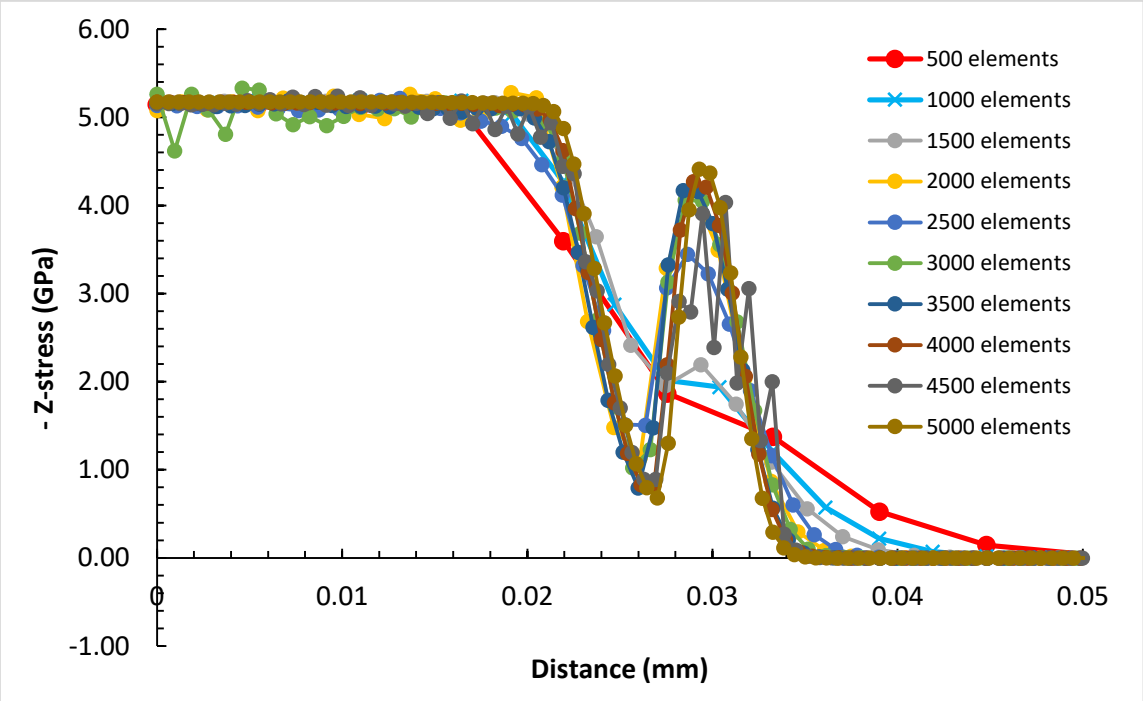

Figure_Apx A-2: Z-stress vs distance wave has propagated into aluminium target plate 5ns after impact for a range of initial element sizes

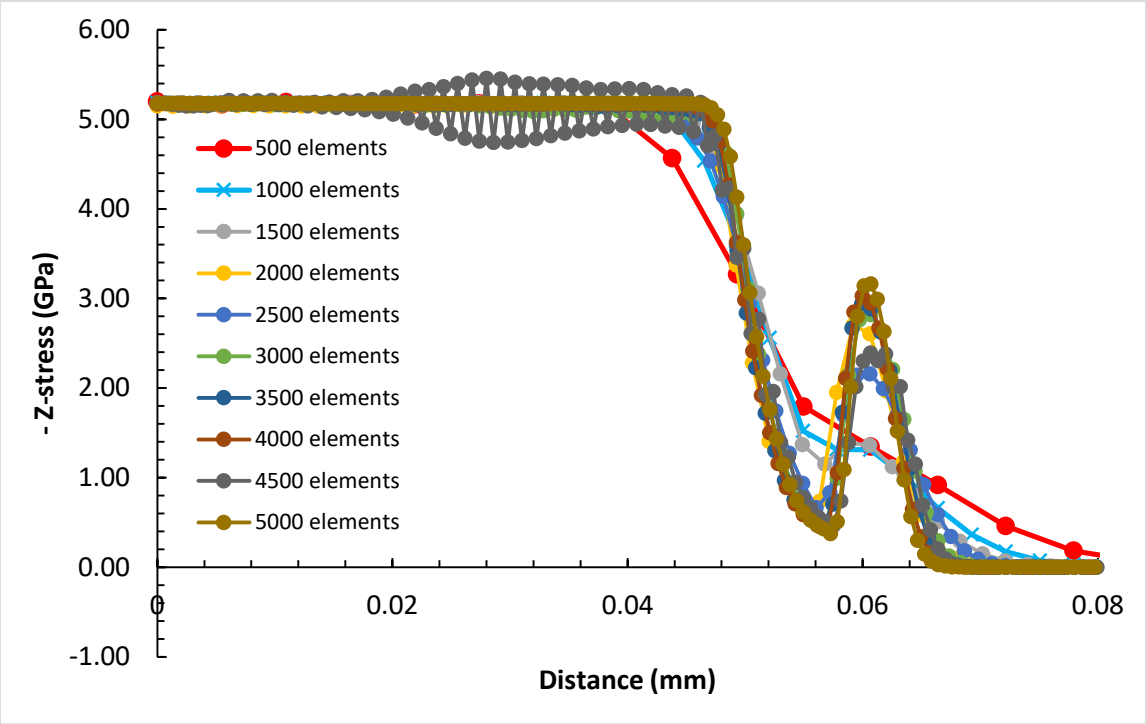

Figure_Apx A-3: Z-stress vs distance wave has propagated into aluminium target plate 10ns after impact for a range of initial element sizes

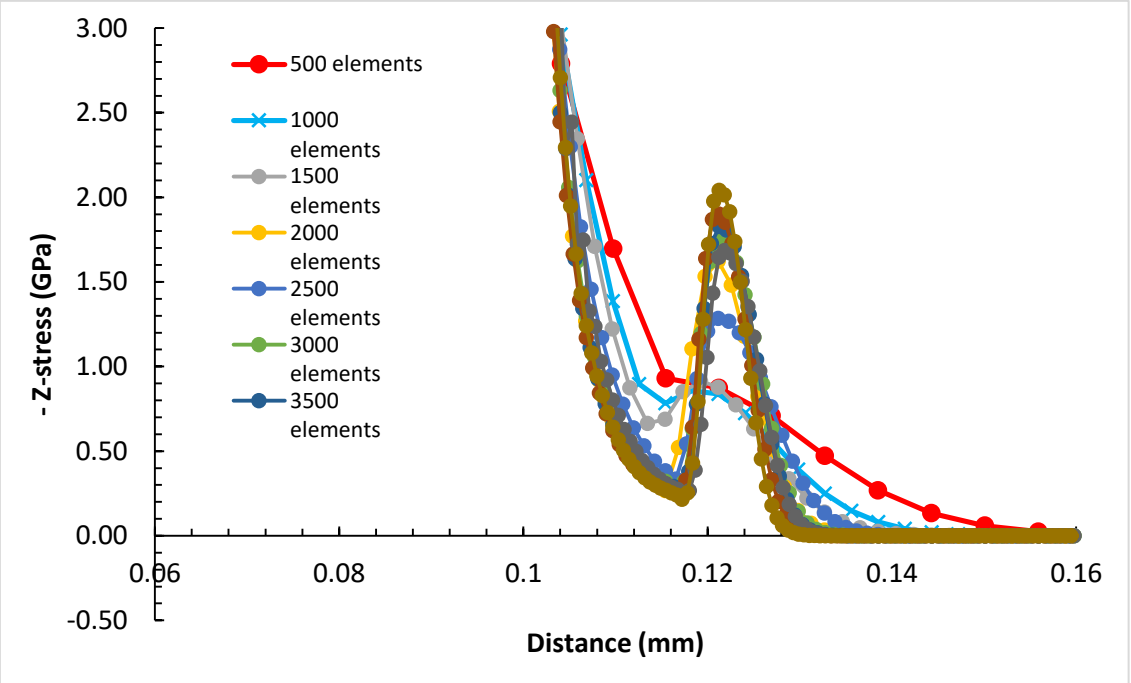

Figure_Apx A-4: Z-stress vs distance wave has propagated into aluminium target plate 20ns after impact for a range of initial element sizes

Table_Apx A-1: Table outlining the number of elements along the z-direction of the 2.9mm target plate and the corresponding initial element size

Number of elements in Z-direction	Initial element size
500	0.00058
1000	0.00029
1500	0.000193
2000	0.000145
2500	0.000116
3000	0.0000967
3500	0.0000829
4000	0.0000725
4500	0.0000644
5000	0.000058

Appendix B Artificial viscosity sensitivity

The sensitivity of the new material model to the artificial viscosity term added by the hydrocode is analysed in this appendix.

To perform the analysis, the two artificial viscosity parameters, the quadratic and the linear term, are varied independently to assess the effect they have upon the results obtained by the model.

Firstly the quadratic constant is assessed. Similar to the analysis presented in Appendix A, plate impact simulation is used here. The plate impact simulation consists of a 2.9mm aluminium target plate, being impacted by a 0.4mm aluminium flyer plate at an impact velocity of 660 m/s.

For each increased shock viscosity value used, the initial stress wave development is assessed at time intervals of 2, 5, 10 and 15ns. The values used for the increased value of the quadratic coefficient are 2, 2.5, 3, 3.5, and 4.

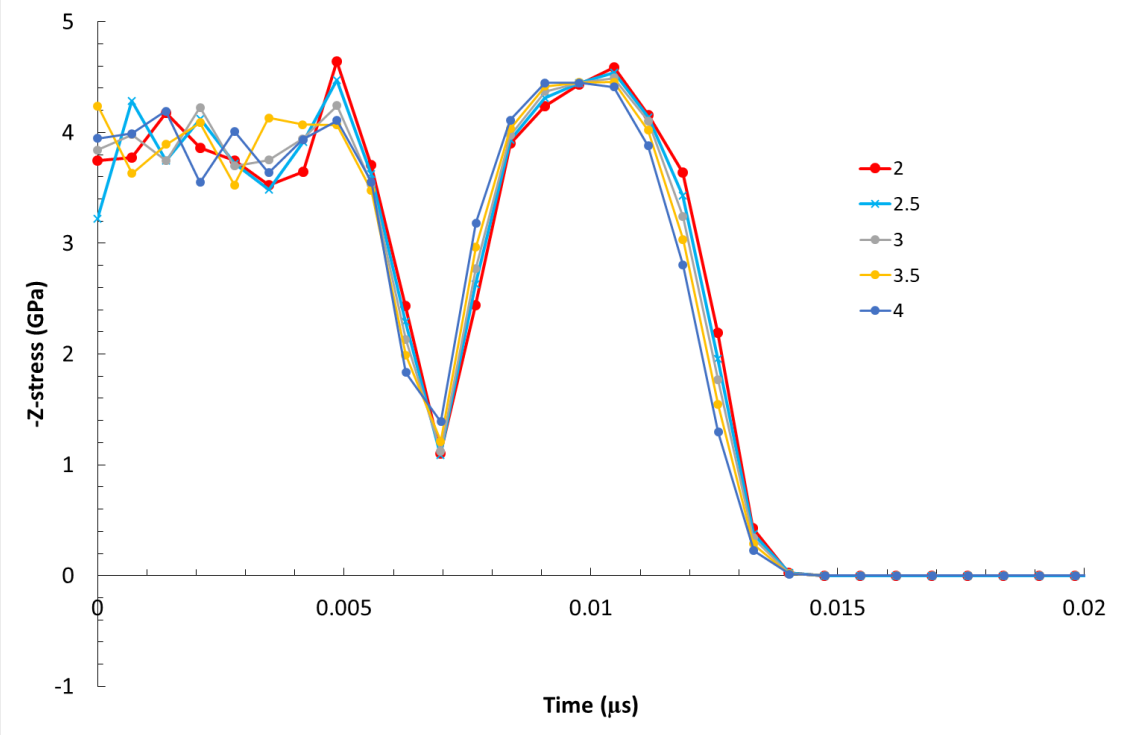

Figure_Apx B-1: Z-stress vs distance wave has propagated into aluminium target plate 2ns after impact for a range of increased values of the quadratic viscosity constant.

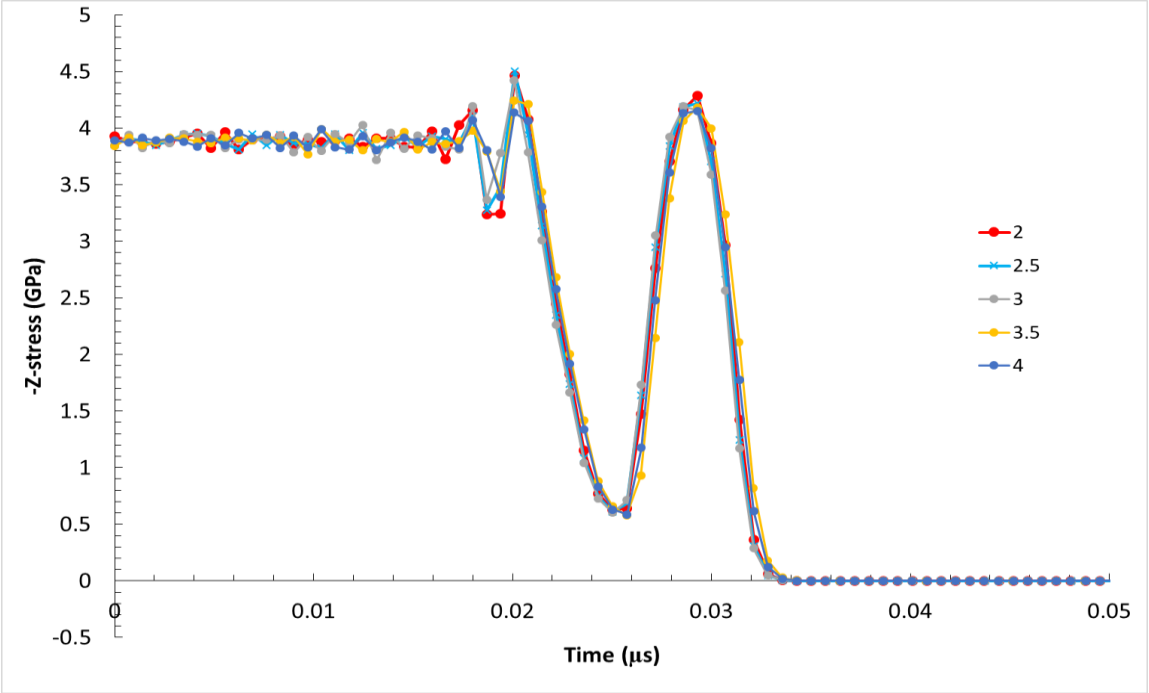

Figure_Apx B-2: Z-stress vs distance wave has propagated into aluminium target plate 10ns after impact for a range of increased values of the quadratic viscosity constant.

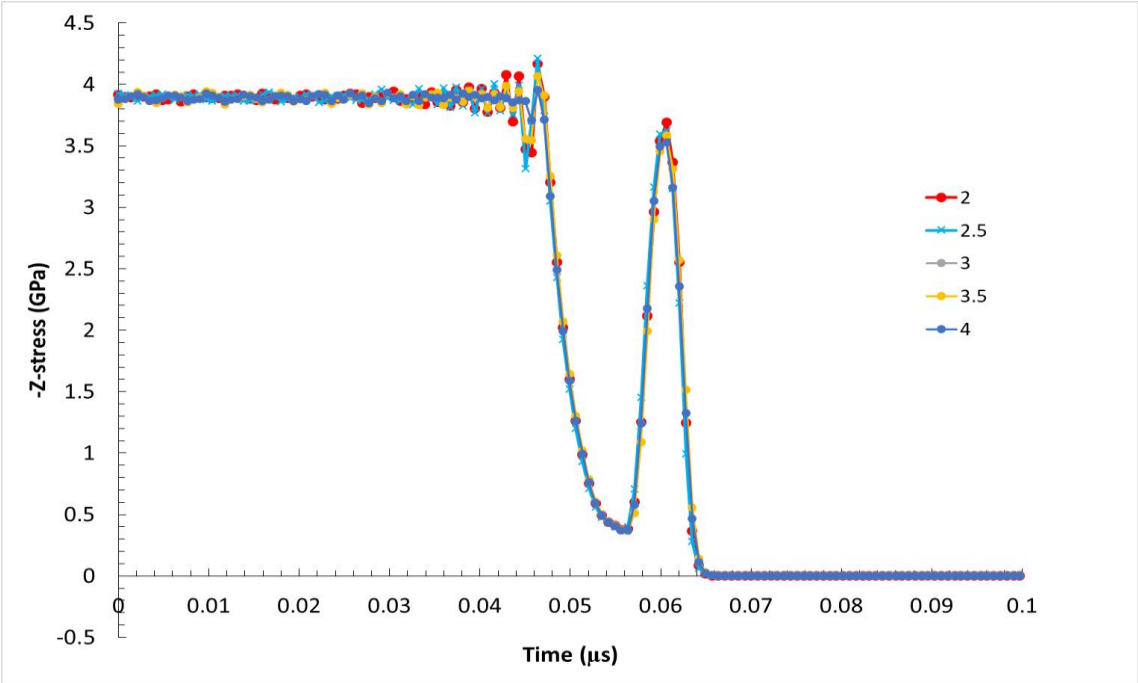

Figure_Apx B-3: Z-stress vs distance wave has propagated into aluminium target plate 10ns after impact for a range of increased values of the quadratic viscosity constant.

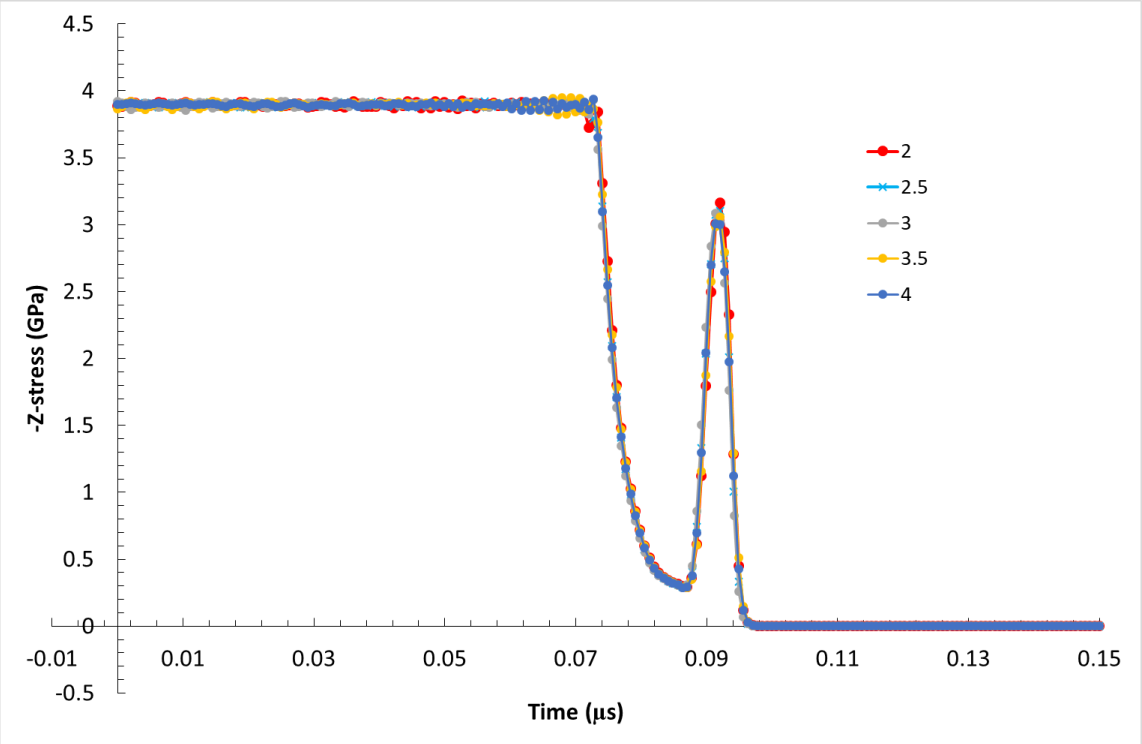

Figure_Apx B-4: Z-stress vs distance wave has propagated into aluminium target plate 15ns after impact for a range of increased values of the quadratic viscosity constant.

It is seen in Figure_Apx B-1 that as the value of the quadratic artificial viscosity constant is increased, the steepness of the initial shock front is decreased. The remaining results for the quadratic constant analysis shown in Figure_Apx B-2, Figure_Apx B-3, and Figure_Apx B-4 show that there is very minimal change in the stress profile as the value of the viscosity constant is increased. Therefore, it can be concluded that for the purpose of simulations using the new material model, the default value for the quadratic viscosity constant is sufficient.

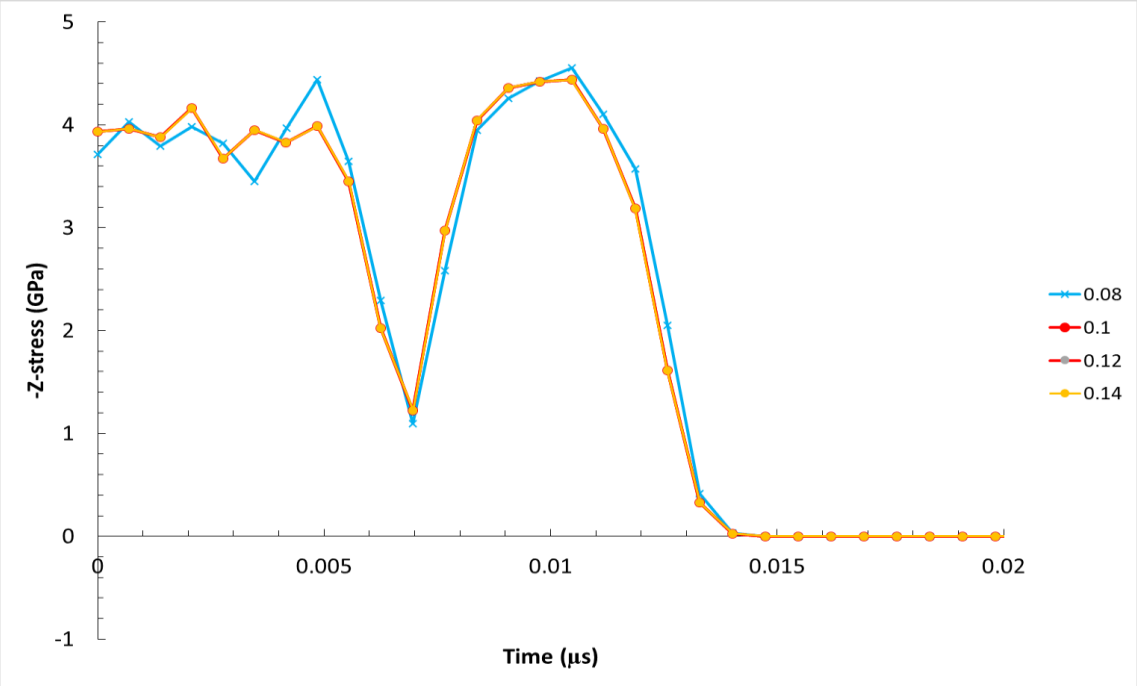

Figure_Apx B-5: Z-stress vs distance wave has propagated into aluminium target plate 2ns after impact for a range of increased values of the linear viscosity constant.

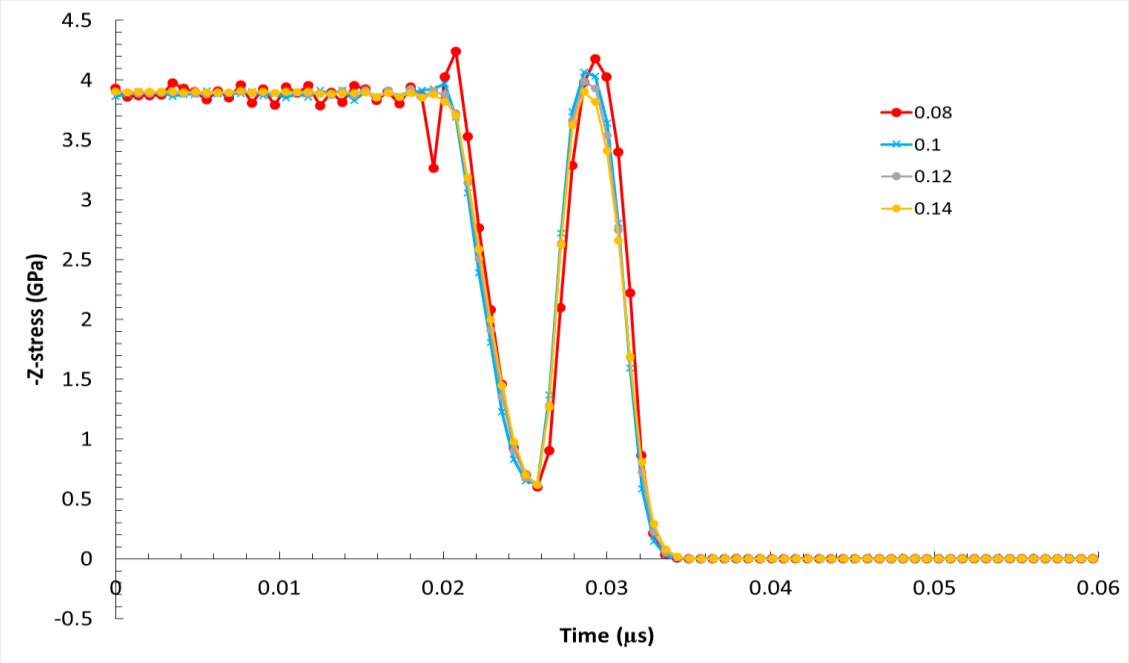

Figure_Apx B-6: Z-stress vs distance wave has propagated into aluminium target plate 5ns after impact for a range of increased values of the linear viscosity constant.

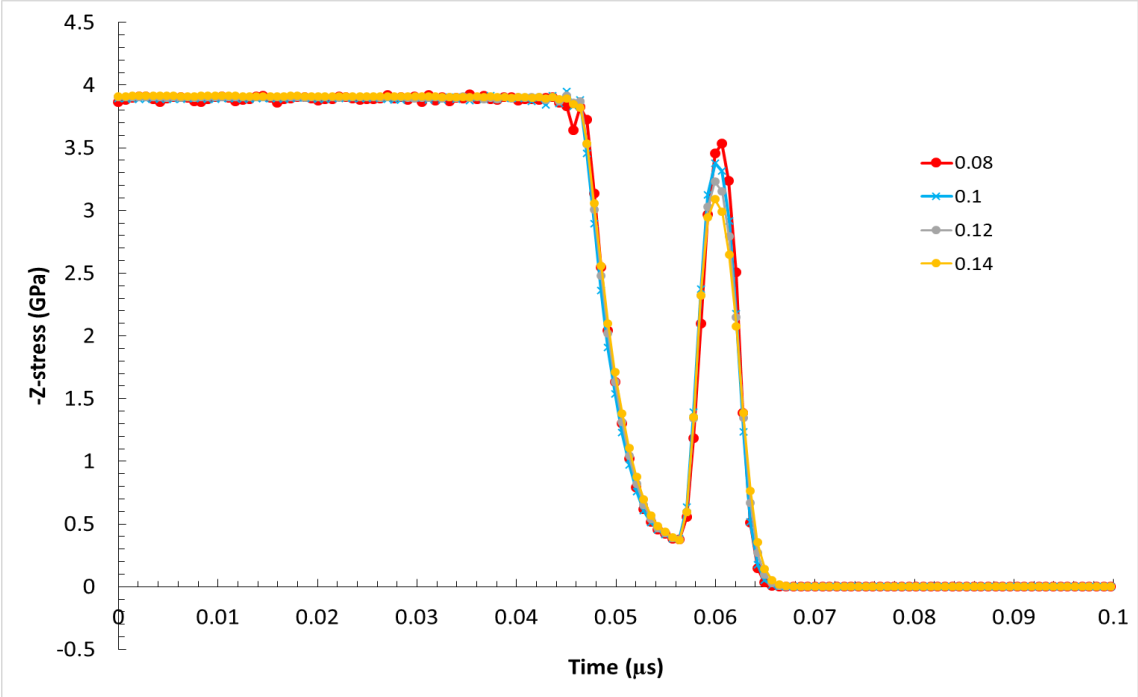

Figure_Apx B-7: Z-stress vs distance wave has propagated into aluminium target plate 10ns after impact for a range of increased values of the linear viscosity constant.

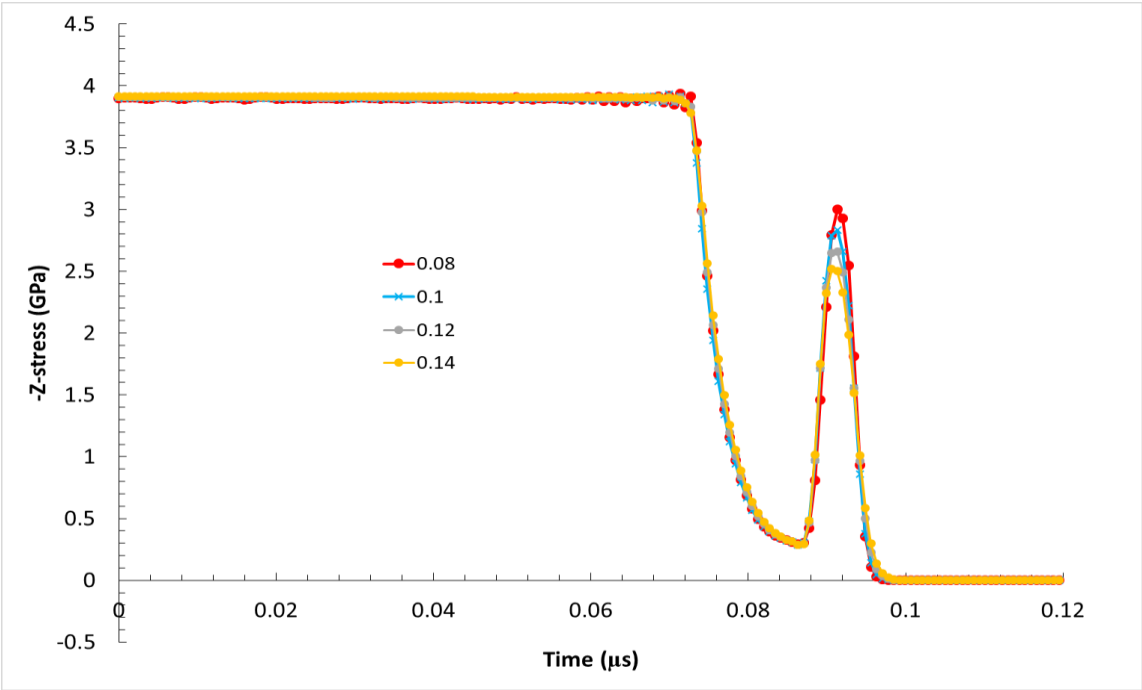

Figure_Apx B-8: Z-stress vs distance wave has propagated into aluminium target plate 15ns after impact for a range of increased values of the linear viscosity constant.

The analysis of the linear artificial viscosity constant, shown in Figure_Apx B-5, Figure_Apx B-6, Figure_Apx B-7 and Figure_Apx B-8 shows that increasing the linear constant has little impact on the shock front. However, it is observed that increasing this term slightly, damps out the noise observed in the steady stress wave, with the value of 0.1 being the smallest to produce a smooth wave. Therefore, for use with the new material model, it is concluded that the value of the linear term should be increased slightly from the default value of 0.06, to the value of 0.1.